Master's thesis

NTNU
Norwegian University of Science and Technology
Faculty of Engineering
Department of Geoscience and Petroleum

Tian Guo

Large-scale CO_2 Injection Analysis: understanding pressure variation in multiple compartments using analytical and computational analysis approaches

Master's thesis in Petroleum Geosciences
Supervisor: Philip S. Ringrose
June 2022

NTNU
Norwegian University of
Science and Technology

Tian Guo

Large-scale CO_2 Injection Analysis: understanding pressure variation in multiple compartments using analytical and computational analysis approaches

Master's thesis in Petroleum Geosciences
Supervisor: Philip S. Ringrose
June 2022

Norwegian University of Science and Technology
Faculty of Engineering
Department of Geoscience and Petroleum

NTNU
Norwegian University of
Science and Technology

Preface

This report is my final work of master's thesis at the Department of Geoscience and Petroleum at the Norwegian University of Science and Technology (NTNU). This project is a team effort, cooperate with Eline Nybråten at the Department of Geoscience and Petroleum, NTNU.

Many thanks to Tobias Dyngeland, Postdoc Ajeet Pathak and Professor Anne C. ELster of High Performance Computing from the Department of Computer Science(NTNU) for their support in programming. Further, I really appreciate Andrea Callioli Santi from Department of Geoscience and Petroleum(NTNU) for her nice helping in geo-information, and the nice tutorial of analysis supporting from Professor Jo Eidsvik of Center for Geophysical Forecasting, NTNU.

I am really glad to have an enjoyable and great cooperation with my teampartner Eline Nybråten, and I am very grateful for my family's support. Finally, my sincere thanks to my supervisor, Philip S. Ringrose, Professor of the Department of Geoscience and Petroleum, for his patient guidance and excellent supporting in making this project a success.

Abstract

Injecting carbon dioxide into deep saline aquifers and then storing it by physically and chemically trapping, is one viable strategy for reducing greenhouse gas emissions and mitigating global warming. To ensure the security of storage, it is vital to comprehend the long-term variations in pressure after the injection of CO_2 and the pressure limits during injection.

The study area of this project is the Smeaheia area, located in the eastern margin of the Horda Platform, around 20∼35 km offshore Western Norway. The Viking Group is the main storage group, where the Sognefjord Formation, the Fensfjord Formation and the Krossfjord Formation act as the major storage units and are the focus of this project.

The problem is investigated using a basin fluid delta-pressure approach and the "box method", with a focus on parameter estimation. To combine with the real cases, the subsurface compartments are also divided into different scenarios based on the faults map to apply the "box method". The "box method" is a way of defining the pressure limit and the compressibility limit on basis of the initial estimation of parameters. Then the pressure variation in each compartment is obtained using an analytical method and the injection result for each compartment is calculated as well. After randomly sampling the variables, a more accurate range for each parameter is generated, on basis of this, the pressure situation and the mass of injected CO_2 is estimated in different time periods. Machine learning approaches can also be applied to the results in future study.

Furthermore, to figure out the deterministic factors, tornado plots are generated for the initial parameters and the PCA method is then applied to further analyse the results. The analysis indicates that both the geometric parameters and injectivity values can have a significant impact on the injection.

Contents

Preface . . . . . **iii**
Abstract . . . . . **v**
Contents . . . . . **vii**
Figures . . . . . **xi**
Tables . . . . . **xv**
Code Listings . . . . . **xvii**
1 Introduction **1**
1.1 Project Description 1
1.2 Background 1
1.3 Study Area Smeaheia 2
1.4 Research Goals 3
2 Theoretical Background **5**
2.1 Greenhouse Gases and Climate Change 5
2.1.1 CO_2 8
2.1.2 CO_2 emission 11
2.2 CCS Technology 13
2.2.1 Why CCS 13
2.2.2 CO_2 capture 14
2.2.3 CO_2 transport 15
2.2.4 CO_2 storage 16
2.2.5 CCS project phase 19
2.2.6 Trapping mechanisms 21
2.3 Smeaheia CO_2 storage site 26
2.3.1 Geological Setting of the Smeaheia 26
2.3.2 Reservoir Formations 26
2.3.3 Caprock 29
2.4 Case Studies Used 30
2.4.1 Smeaheia 30
2.4.2 Snøhvit 30
2.5 Pressure Theory 31
2.5.1 Pore Pressure 31
2.5.2 Fracture Pressure 32
2.5.3 Overburden Stress 32
2.6 Basin Fluid Delta-pressure Approach 34

2.7 Simple Analysis of Rock Compressibility Limits . . . 38
3 Method and Data . . . 39
3.1 Box Method . . . 39
3.2 Compartment Division and Scenarios . . . 41
3.3 Random sampling . . . 42
3.3.1 Uniform Distribution . . . 42
3.3.2 Gaussian Distribution . . . 42
3.4 Sensitivity analysis . . . 43
3.5 PCA . . . 44
3.6 Data . . . 46
3.6.1 CO_2 Density . . . 46
3.6.2 Porosity . . . 47
3.6.3 Injectivity . . . 47
3.7 The workflow . . . 48
4 Results . . . 49
4.1 Scaling Parameter A . . . 49
4.1.1 Geometric factor . . . 49
4.1.2 Compressibility . . . 50
4.2 Injection Constraint . . . 53
4.2.1 Maximum Volume limit . . . 53
4.2.2 Maximum Pressure Limit . . . 53
4.3 Pressure variation . . . 55
4.4 Injection Volume Estimation of Different Scenarios . . . 58
4.5 Sensitivity analysis . . . 60
4.6 Mass of Injection CO_2 . . . 67
4.7 Numerical analysis result . . . 71
5 Discussion and Conclusion . . . 77
5.1 Effect of compressibility . . . 77
5.2 Effect of injectivity . . . 77
5.3 Injection results of different scenarios . . . 77
5.4 Tornado plot . . . 78
5.5 PCA . . . 78
5.6 Uncertainty Analysis . . . 79
5.6.1 Parameter . . . 79
5.6.2 Data . . . 79
5.7 Scope of the work . . . 80
5.8 Conclusion . . . 81
Bibliography . . . 83
A Additional Material . . . 87
A.1 Map of Smeaheia area . . . 87
A.2 Box Division . . . 89
A.3 Injection CO_2 volume estimate . . . 91
A.4 Code . . . 93
A.4.1 Pressure Function . . . 93

A.4.2 Random sampling A 97
A.4.3 Injection Volume calculation 100
A.4.4 PCA 104

Figures

1.1 Caption used in list of tables 3

2.1 Evidence for human influence on climate (NASA-climate, n.d.) . . . 6
2.2 Summary of radiative fluxes in the Earth's atmosphere (Ringrose, 2017) 7
2.3 Summary of the principal components of the radiative forcing of climate change between 1750 and 2011.(IPCC, 2016) 7
2.4 CO_2 phase diagram (Whitson and Brulé, 2000) 8
2.5 Density of CO_2(Ringrose, 2020) 9
2.6 Density of CO_2 as a function of pressure and temperature (Whitson and Brulé, 2000) 10
2.7 Viscosity of CO_2 as a function of pressure and temperature (Whitson and Brulé, 2000) 10
2.8 Schematics of carbon cycle (Ringrose et al., 2017) 11
2.9 Historical record of global CO_2 emissions(Stephenson et al., 2019) 11
2.10 Total energy supply in the NZE(net-zero emissions scenario)(IEA, 2021a) 13
2.11 Overview of CCS technologies (Ringrose, 2020) 14
2.12 CO_2 capture process(Gibbins and Chalmers, 2008) 15
2.13 Overview of geological storage options for CO_2(Ringrose, 2020) . . 17
2.14 Sketch of open,closed, semi-closed systems around an injection well interval(Zhou et al., 2008) 18
2.15 Four phases of CCS projects(Cooper, 2009) 19
2.16 Techno-economic resource–reserve pyramid for discussing CO_2 storage estimates(Bachu et al., 2007) 20
2.17 CO_2 storage trapping mechanisms(Ringrose, 2020) 22
2.18 Sketch of capillary trapping of a CO_2 phase in super-critical (dense) phase in a completely water-wet porous medium. Due to smaller pore throats of caprock with small grains compared to larger pore throats in the aquifer, the gas column will rise quite slightly(Ringrose, 2020) 23
2.19 CO_2 storage flow processes(Ringrose, 2020) 24
2.20 Sketch of the CO_2 sequestration process in a simple geometry(Pau et al., 2010) 24

2.21 CO_2 absorption in clay minerals(Cooper, 2009) 25
2.22 The depth structure map of the study area 27
2.23 The chronostratigraphic framework for the Viking Graben and Horda Platform 28
2.24 Hydrostatic pressure, pore pressure, overburden stress, and effective stress in a borehole 31
2.25 Pore pressure gradient, fracture gradient, overburden stress gradient (lithostatic gradient), mud weight, and casing shoes with depth. 33
2.26 Pressure depth functions(Ringrose and Meckel, 2019) 35
2.27 Idealised project lifetime pressure varies with time 37

3.1 Scenario D compartment map 41
3.2 Hierarchy of scenario B,C and D 41
3.3 A selection of Normal Distribution Probability Density Functions. Both the mean μ, and variance σ^2 are varied('Normal Distribution PDF', 2022) 42
3.4 Density of CO_2 versus depth in three formations 46
3.5 Workflow of the project 48

4.1 A varies with area size 50
4.2 A varies with pore volume 50
4.3 Scaling parameter A versus size for different compressibility 51
4.4 Scaling parameter A versus pore volume for different compressibility 51
4.5 Different compressibility ranges set for A versus pore volume plots. 52
4.6 A distribution with random sampling compressibility 52
4.7 Maximum pressure limit versus depth in three formations 54
4.8 Pressure curve in B2 compartment of Sognefjord Fm. 56
4.9 Pressure curve in B5 compartment of Sognefjord Fm. 56
4.10 Pressure curve in C9 compartment of Sognefjord Fm. 57
4.11 Pressure curve in D5 compartment of Sognefjord Fm. 57
4.12 Some examples for injection volume(m3) in Sognefjord formation . 58
4.13 Some examples for injection volume(m3) in Fensfjord formation . . 58
4.14 Some examples for injection volume(m3) in Krossfjord formation . 58
4.15 Injection volume versus pressure in year 25 60
4.16 Injection volume versus pressure in year 50 61
4.17 Examples for the results of random sampling parameters in year 25 64
4.18 Tornado plot for B3 compartment in Sognefjord Formation 65
4.19 Tornado plot for B3 compartment in Fensfjord Formation 65
4.20 Tornado plot for B3 compartment in Krossfjord Formation 65
4.21 Tornado plot for C7 compartment in Krossfjord Formation 66
4.22 Tornado plot for D11 compartment in Krossfjord Formation 66
4.23 Injection result in 50 year $C_b = 5.0E-09\text{Pa}^{-1}$,$I_c = 60\text{m}^3/\text{day/bar}$ 67
4.24 Injection result in 50 year $C_b = 3.0E-09\text{Pa}^{-1}$, $I_c = 2000\text{m}^3/\text{day/bar}$ . . . 68
4.25 Mass of injection CO_2 in year 25 versus pressure 69
4.26 Mass of injection CO_2 in year 50 versus pressure 69

4.27 Schematic diagram of PCA 71
4.28 PCA analysis result of the first test 74
4.29 PCA analysis result of the second test 75
4.30 PCA analysis result of different variables test 76

A.1 Structure map of Smeaheia, modified from Wu et al., 2021 87
A.2 Fault map of Smeaheia. 88
A.3 Scenario B compartment map 89
A.4 Scenario C compartment map 90
A.5 Total CO_2 injection volume in each compartment 92

Tables

3.1 Porosity of different formations 47
3.2 Injection rate and injectivity used in final result 47

4.1 Setting of parameter value used in tornado plot 62

Code Listings

listings/pressure.py 93
listings/calc_cb.py 97
listings/injVandPress.py 100
listings/PCA.py 104

Chapter 1

Introduction

1.1 Project Description

The case study is in the Smeaheia area comprising multiple rock compartments defined for different fault scenarios, which are defined from published seismic mapping. Various analytical approaches combined with a computational approach are applied to explore the deterministic factors which control the CO_2 injection and figure out the optimal injection scenarios, and further predict the long-term pressure decay over time.

The project is a team effort and the focus of this thesis is to analyse the effect of different geological parameter settings on injection results through program coding. The geological parameters act as input for computation, and the pressure variation and the injection results are the output. The aim is to optimize the CO_2 injection.

The main purposes of this thesis are to explore the deterministic parameters controlling the injection, to figure out the best compartment scenario which can offer the largest storage capacity, to analyse the pressure variation in all compartments, and then optimize the injection. Further, this project sets a foundation for the future application of machine learning approach.

1.2 Background

The average global temperature of the earth is closely related to the GHGs (greenhouse gas) concentration in the atmosphere of the earth. After the industrial revolution in the last century, the GHGs concentration has been rising steadily due to human activity, leading to the global temperature rising. As the Intergovernmental Panel on Climate Change(IPCC) reported, it is unequivocal that the increase of CO_2, methane(CH_4) and nitrous oxide(N_2O) in the atmosphere over the industrial era is the result of human activities and that human influence is the principal driver of many changes observed across the atmosphere ocean, cryosphere and biosphere"(IPCC, 2021). At meanwhile, the carbon cycle is one of the

most significant chemical systems which enable life on earth to be sustained, human civilizations are also built on carbon. Global energy-related CO_2 emissions remain at 31.5 Gt, which leads to the highest annual average CO_2 concentration ever recorded in 2020, 412.5 parts per million, about 50% higher than at the start phase of the industrial revolution(IEA, n.d.).

To reduce global CO_2 emissions, several low carbon energy solutions have been implemented so far, such as using renewable energy sources, nuclear power, fuel switching, improving efficiency in the use of energy and others. Although renewable energy is considered as the most essential approach to reduce carbon emissions, the practical situation indicates the limitation of this solution: the capacity to improve wind, solar and hydropower is insufficient to meet the global energy demand, the cost of renewable energy is considerable and most renewable energy sources have some intermittency and cannot meet the demand when consumer needed. Capture and geological CO_2 storage can provide a efficient way to reduce emitting CO_2 into atmosphere, by capturing CO_2 from major stationary sources, transporting it by pipeline or ship in dense form. Injecting CO_2 into suitable geological formations at selected sites can store the CO_2 underground for a long period of time which can be considered that more than 99% of the injected CO_2 will be stored for 1000 years(Metz et al., 2005). Combining the technology of existing enhanced oil recovery(EOR), economic benefit increasement also improve the feasibility of the CCS projects. Comprehensively, carbon capture and storage with fossil-fuel is currently concluded that the only solution to the climate challenge in order to avoid or limit CO_2 emissions.

To meet the goal of global emissions reduction strategy and achieve net-zero emission by 2050, CCS (carbon capture and storage) is now globally used, which takes a huge proportion of carbon emission reduction. CCS is anticipated to support approximately 13% of total cumulative emissions reductions through 2050, requiring around 120,000 million tonnes (Mt) of cumulative CO_2 reduction by 2050. Annual storage rates in 2050 are expected to be 6∼7,000 Mtpa (LPDD, 2022). There exists 51 large scale CCS facilities globally, 4 of them under construction, 19 in operation and 28 in various stages of development, the capture capacity estimation from all 51 facilities is approximately 96 million tonnes of CO_2 every year(LPDD, 2022). In Norway, there are several CCS facilities which provide abundant information and experience, such as the Sleipner and Snøhvit are both known as successful CCS projects.

1.3 Study Area Smeaheia

The study area in this project is the Smeaheia on the Horda Platform in the Norwegian North Sea. The Smeaheia is situated at the east margin of the Troll Field and around 50 km west from Mongstad (M. Mulrooney, 2021). The Vette Fault System(VFS) in the west and the Øygarden Fault System (ØFS) in the east are the boundaries of this area. There are two structural closures in the Smeaheia area, “Alpha 32/4-1” in the west and “Beta 32/2-1” in the east. (Seismic reservoir

characterization of potential CO_2 storage reservoir sandstones in Smeaheia area, Northern North Sea) The main storage reservoir formations of this area are the Sognefjord, Fensfjord, and Krossfjord Formations from the Viking Group, with the depth of around 1200 m to 1700 m(Fawad et al., 2021).

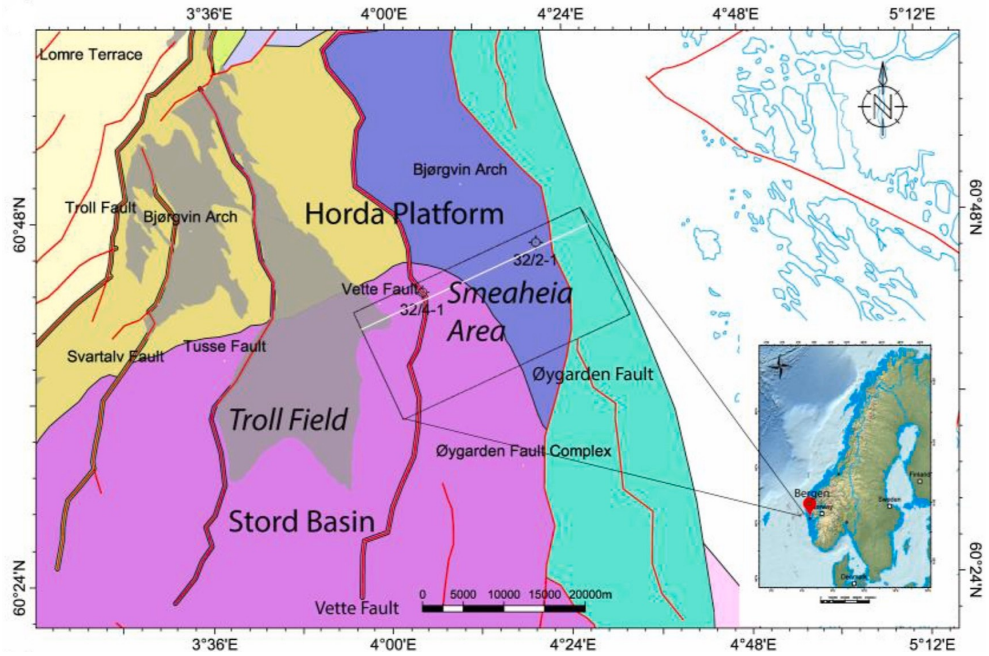

Figure 1.1: Location of the CO_2 storage site Smeaheia, offshore Norway(Fawad et al., 2021)

1.4 Research Goals

In this project, the “basin fluid delta-pressure analysis approach” and “box method” are used as the theoretical foundation. The "basin-fluid pressure analysis approach" is proposed by P. S. Ringrose and T.A. Meckel(Ringrose and Meckel, 2019), which is based on the generic approach of pressure and stress trends in the offshore sedimentary basins, summarized from different offshore basins with well-knowledge over decades. The "box method" is also used to compare and acquire a thorough perspective of the parameters. The compressibility calculation is used as the basis of this method, which simplifies the rock compartments into different boxes, the box sizes are attended as geometric variables, the rock property parameters include porosity and compressibility, and the solution is primarily controlled by pressure changes before and after CO_2 injection. The basin fluid delta-pressure approach is used as the primary method, which is based on the integration of the injectivity equation over the project life time, isolating the parameters within the approach and comparing them to the box method on the basis of similar parameters, then the initial estimate of the inner relationship of parameters is obtained.

This study focuses on the Sognefjord Formation, Fensfjord Formation and Krossfjord Formation from the Viking Group, actual practice geological data from the Smeaheia area is applied into box method and generate three scenarios based on the fault structures. To calculate the pressure variation in each compartment and analyse the injection result, several parameters are required, which all generated from the initial estimation. The analyse shows two constraints of the injection, the most general limit is given by pressure, another is from compressibility. Random sample approach is also applied to obtain ranges of each variable so as to optimize the injection. In the beginning phase, it is found that the pressure limits can be reached in most of the compartments before compressibility limit, only in some extremely small compartments the compressibility limits are reached. The injection result in different scenarios also indicates the complicated subsurface structures can affect the total injection volume, the results are not determined by the boundary situations directly. For a more accurate parameter estimation, the sensitivity analysis specific as the tornado plot is applied to the result to figure out the importance of different parameters, according to that, the further analysis reveals the importance of injectivity, when increases the value closed to the practical project data, the final result shows that the injectivity limits are essential as well. Based on the graphs of pressure and mass of injected CO_2, PCA method is utilized to have a deeper understanding of this final result.

This study serves as a basis for the future work that will incorporate more advanced machine learning approaches into the research in order to figure out the key controlling parameters, and figure out the best scenario and optimize the injection process. During this stage, the primary parameters of the two solutions are examined, parameters involved in the calculation have a more specific range, pressure limit and compressibility limit are the main findings. The pressure variation as well as the maximum injection CO_2 volume and mass in each compartment is calculated and plotted. Simple sensitivity analysis (tornado plot) and numerical analysis (Principal Component Analysis) have completed to figure out the parameter influences, this can be applied to the future study.

Chapter 2

Theoretical Background

2.1 Greenhouse Gases and Climate Change

The greenhouse gases(GHGs) are named because of the heat absorption and emit radiation effects, which leads to the greenhouse effect. The main greenhouse gases in the atmosphere are water vapour, carbon dioxide, methane, nitrous oxide and ozone. After the industrialization revolution, along with the clear-felling forests, farming and several human activities, which have caused increasing quantities of GHGs in the atmosphere, the concentration of GHGs has been increasing steadily as the result of the human activity, especially the fossil fuel burning and the land-use changes. Due to this, the Earth's average global temperature has risen by 0.08 ℃ per decade since 1880(Rebecca Lindsey, 2021), the average surface temperature of our planet has risen around 1.01 ℃ since the late 19th century. Most of the warming occurred in the last 40 years, the seven most recent years being the warmest, the years 2016 and 2020 are considered the warmest year on the record(NASA-climate, n.d.). The graph shows the evidence of human influence on climate (Fig 2.1).

The main controls on the Earth's climate can be divided into 3 groups: External factors, Earth-system factors and atmospheric factors. The external factors include the Milankovitch cycles and the solar heating cycles. The Milankovitch cycles can be clearly seen in the climate record, which includes:

1) The shape of Earth's orbit (eccentricity), the total global annual variation in isolation caused by the eccentricity cycle is very small. As the variations in the Earth's eccentricity are quite small, they are relatively minor factors influencing seasonal climate change.

2) The angle of Earth's axis titled with respect to Earth's orbital plane (obliquity) , in the past million years, the obliquity varied between 22.1 and 24.5 degrees with respect to Earth's orbital plane. The greater the inclination of the Earth's axis, the more extreme our seasons, the effects are not uniform globally as well, areas in higher latitudes always receive a larger change in total solar radiation than the areas near the equator.

3) The direction Earth's axis of rotation is pointed (precession). Precession

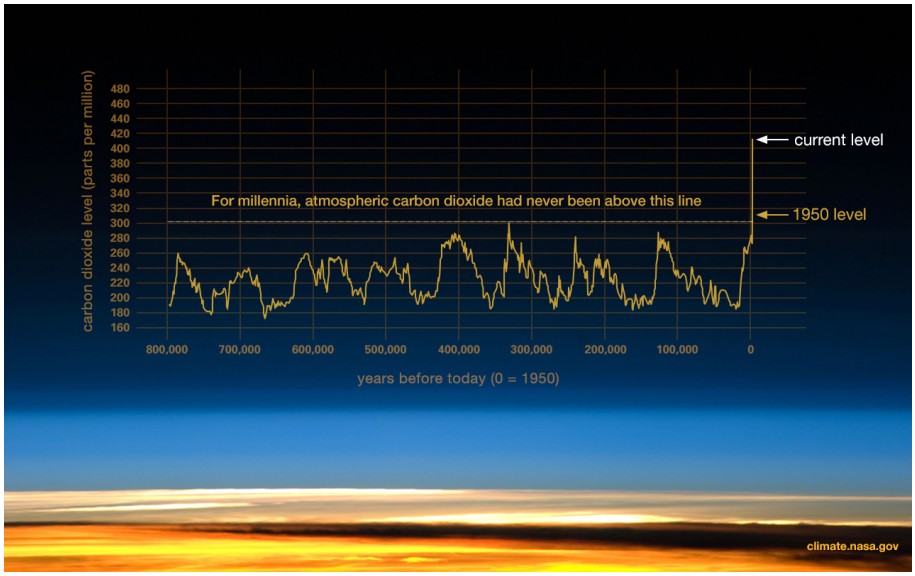

Figure 2.1: Evidence for human influence on climate (NASA-climate, n.d.)
This graph, based on the comparison of atmospheric samples contained in ancient ice cores and more recent direct measurements, provides evidence that atmospheric CO_2 has increased dramatically since the Industrial Revolution compared to paleoclimatologic (past climate) measurements over the past 800,000 years (NASA-climate, n.d.).

can affect seasonal timing relative to the Earth's closest/farthest points around the sun, both the axial and apsidal precession lead to the precession cycle spanning around 23,000 years on average in total (Buis, 2020).

The Earth-system factors include mainly ocean circulation and volcanic eruption. The atmospheric factors mainly refer to the greenhouse gas effects. The GHGs effects involved a few physical processes: the interactions with atmospheric molecules and particles motivate the incident sunlight of scattering and reflection back into space, this process accounting for about 26% of incident solar energy; absorption of energy by atmospheric gases, vapour and particles, this process accounts about 19% of incident solar energy; the sunlight reflects back into space from the planet's surface, this takes around 4% of incident solar energy. After the energy reaches the surface, the energy can then be further consumed by heating the ground face (this leads the Earth to act as a radiator of energy in the longwave portion of the spectrum, melting ice and snow, evaporation of water and the photosynthesis of plant (Ringrose, 2021), as the Fig 2.3 shown.

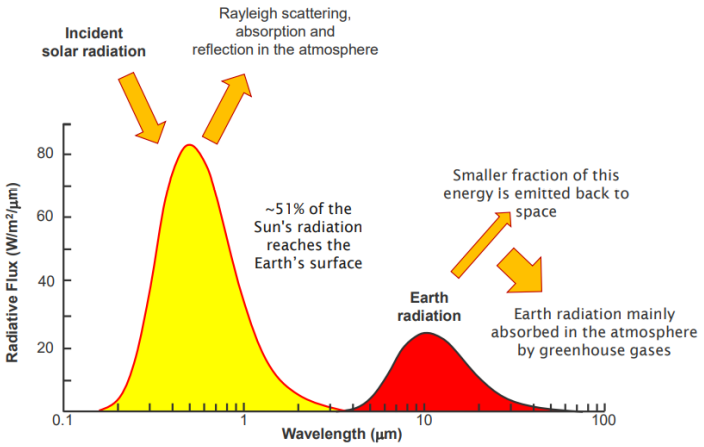

Figure 2.2: Summary of radiative fluxes in the Earth's atmosphere (Ringrose, 2017)

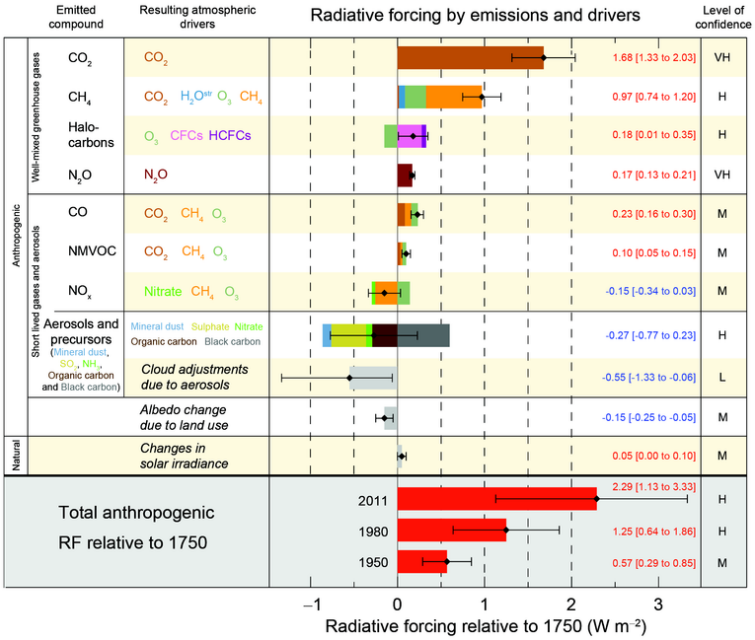

Figure 2.3: Summary of the principal components of the radiative forcing of climate change between 1750 and 2011.(IPCC, 2016)

The figure plots Radiative Forcing (RF) estimates in 2011 relative to 1750 and aggregated uncertainties for the main drivers of climate change. (IPCC, 2016).

2.1.1 CO_2

CO_2 is a nontoxic, colorless and stable compound, at standard conditions, CO_2 is in a gaseous state. At 1 atm and 15 ℃, the density of CO_2 is 1.5 times denser than air, the molecular weight is 44.01 g/mol. In the petroleum industry, CO_2 exists as gas or as a liquid-like supercritical fluid. The physical properties of carbon dioxide change with different pressure and temperature, leading to a potential change in the phase. This change will affect the behaviour of carbon dioxide in different environments.

Fig 2.4 shows the CO_2 phase varies with temperature and pressure. The critical isochor defines the supercritical condition, where the phase density is equal to the critical density of 0.47 g/cm^3. The critical point and the triple point are the key points in this diagram: the critical point is at 30.98 ℃ and 73.8 bara, which defines the condition of no boundaries between different phases. The triple point is located at 5.2 bara and -56.6 ℃(Philip Ringrose, 2021). To the left of the triple point and at very low temperature conditions, carbon dioxide will be in a solid state, acting as snow or dry ice. Under standard conditions and temperatures above -80 ℃ and relatively low pressure, CO_2 will be in the gas phase. Liquid CO_2 will appear above the triple point (Whitson and Brulé, 2000). The physical properties of a supercritical CO_2 are crucial for gas and liquid phases in both, so it is difficult to figure out the phase of CO_2 whether it is in gas or liquid form.

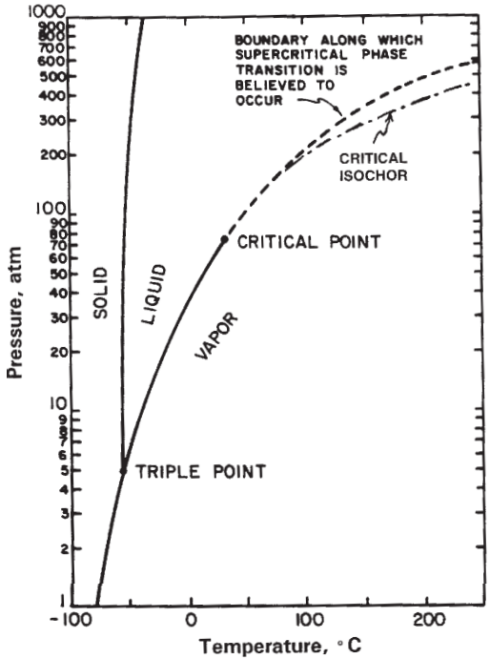

Figure 2.4: CO_2 phase diagram (Whitson and Brulé, 2000)

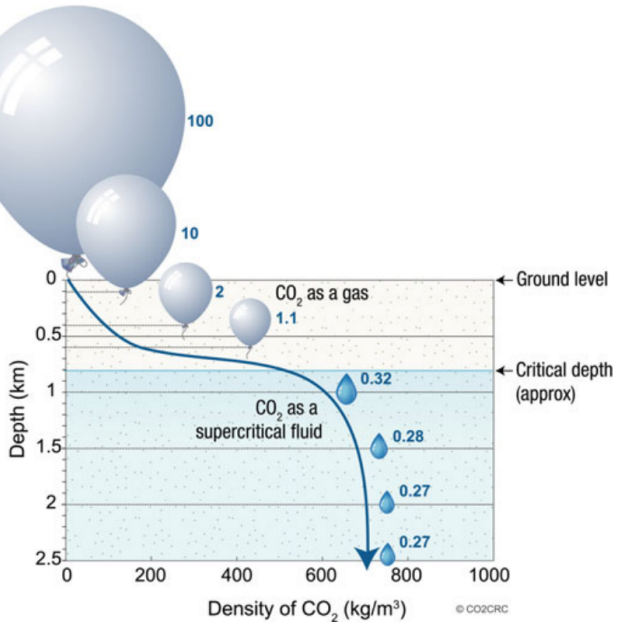

Figure 2.5: Density of CO_2 (Ringrose, 2020)
Simplified CO_2 density versus depth diagram (©CO2CRC, image courtesy of CO2CRC.Ltd

Density

Fig 2.6 shows density of CO_2 as function of pressure and temperature. It indicates that the increase of pressure can lead to an increase in density, and the rising in temperature can result in a decrease in density. The density changes a lot to a bigger degree at lower pressures compared to the higher pressure cases, the density is more sensitive at the lower pressure changes.

Fig 2.5 shows how the density of CO_2 varies with depth. This indicates the storage of CO_2 should be set in relatively deep depth to make sure the CO_2 is in a dense form, either in a supercritical phase or a liquid phase. The CO_2 storage site needs to be deeper than 800 m, although the transition to the liquid phase depends on temperature and local geothermal gradients in fact (Ringrose, 2020).

Viscosity

Fig 2.7 shows the viscosity of CO_2 as a function of pressure, which varies with temperature as well.

According to the graph, the viscosity increases with pressure increasing, when temperature rising, the CO_2 gets less viscous and the flows of CO_2 gets much faster. The sensitivity of CO_2 viscosity is related to the pressure and low temperature conditions.

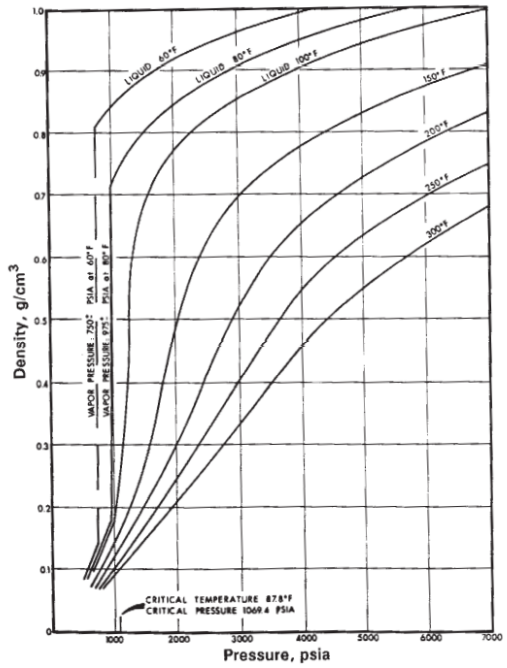

Figure 2.6: Density of CO_2 as a function of pressure and temperature (Whitson and Brulé, 2000)

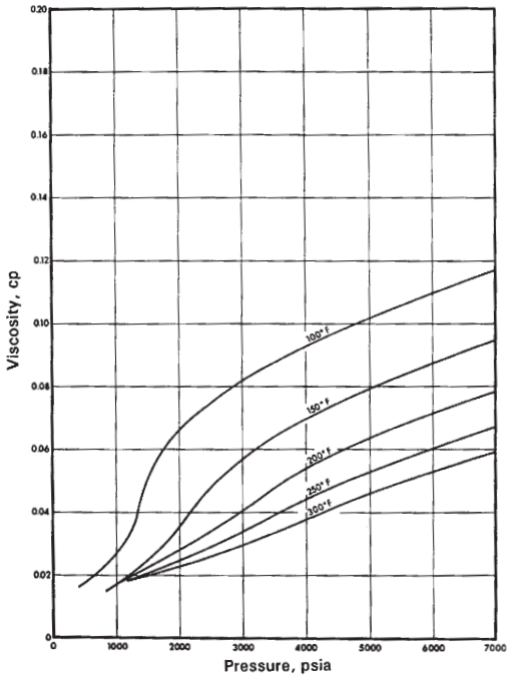

Figure 2.7: Viscosity of CO_2 as a function of pressure and temperature (Whitson and Brulé, 2000)

2.1.2 CO_2 emission

In nature, CO_2 can be stored in different kinds of carbon reservoirs for very long period. In rocks, oceans, plants and in the atmosphere the CO_2 always exists, so the carbon cycle is essential to the earth. The carbon cycle can be simplified shown in Fig 2.8. The hydrosphere, biosphere, atmosphere and lithosphere exchange carbon through numerous ways. After industrial revolution, the human activity increases the emission of carbon, leads to the huge change in the carbon ecosystem, the CO_2 exchanges in different parts lose balance.

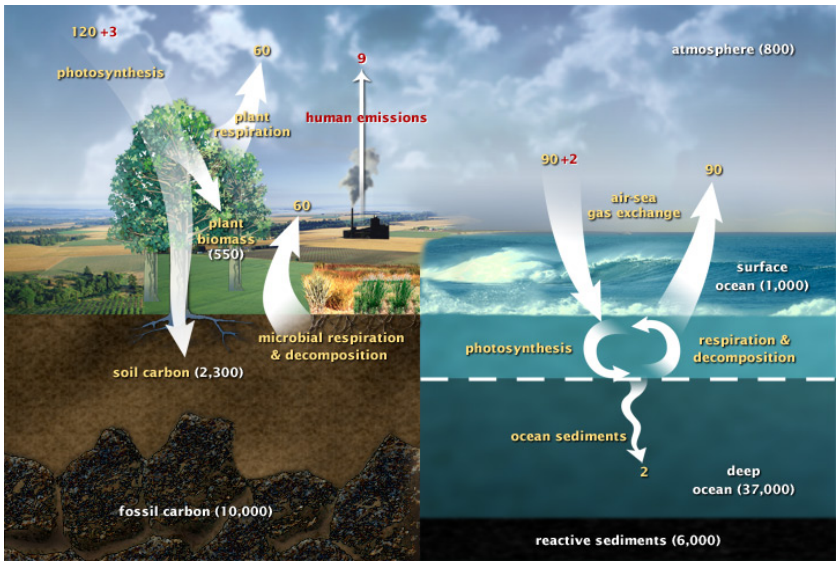

Figure 2.8: Schematics of carbon cycle (Ringrose et al., 2017)

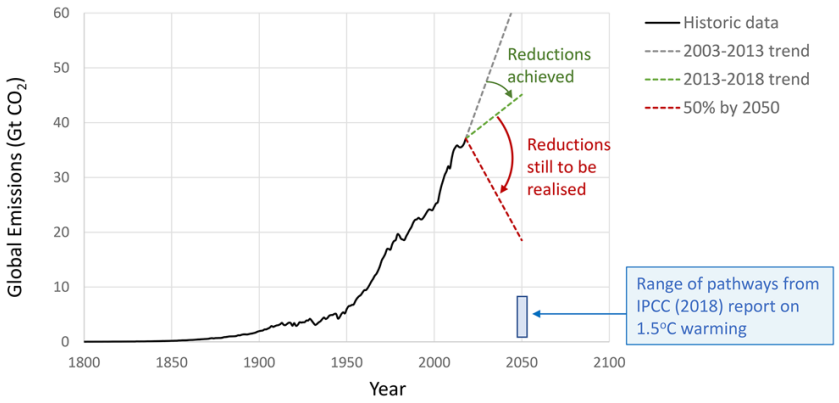

Figure 2.9: Historical record of global CO_2 emissions(Stephenson et al., 2019)
Data sources: carbon emissions data up to 2013 from https://cdiac.ess-dive.lbl.gov/ with 2014–2018 years estimates from www.wri.org)(Stephenson et al., 2019).

Fig 2.9 shows the historical record of global CO_2 emissions in the world compare to various projections. The concentration of atmospheric CO_2 has risen dra-

matically compared to the 1800, as the figure shown, the amount of CO_2 emission has increased rapidly after 1950, the main possible cause is the burning of fossil fuels, so as to reduce the carbon emissions, this will also be the main effort direction. But our world still highly depends on the fossil fuel energy, this provides the main primary energy and likely to remain for a long time in the future. Thus the solution of carbon emission reduction which also allows the fossil burning is necessary. Carbon capture and storage technology can meet this requirement and provide a solution to reduce huge amount of CO_2.

2.2 CCS Technology

2.2.1 Why CCS

According to the report from IEA (IEA, 2021a), the total energy supply will fall to 550 exajoules(EJ) in 2030, 7% lower than in 2020. With the significant growth of the global population and economy, total energy supply declines because of the energy intensity decreasing, as Fig 2.10 shown.

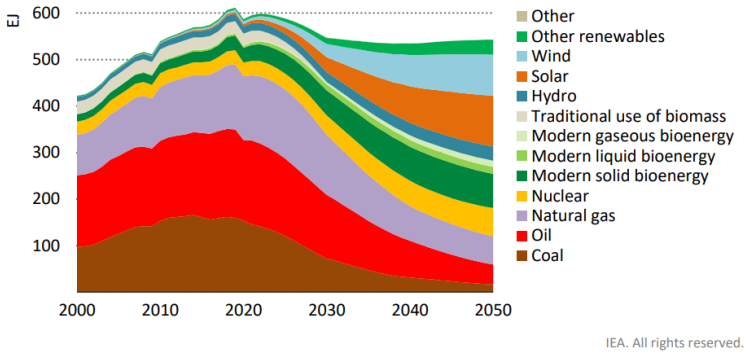

Figure 2.10: Total energy supply in the NZE(net-zero emissions scenario)(IEA, 2021a)

In 2020, oil accounts for 30% of the total energy supply, coal for 26%, natural gas for 23%. In the net-zero emissions scenario, total fossil fuel consumption in 2050 would be about 120 EJ, compared to 460 EJ in 2020. Although the net carbon dioxide emissions from the energy section in 2020 would plan to be zero, fossil fuel use is still not down to zero for many practical reasons(IEA, 2021a):

1. For non-energy purposes, in the net-zero emissions scenario, more than 30% of the total fossil fuel use in 2050 is for non-combustion applications. For example, as a raw material for chemicals, and for the production of lubricants, paraffin waxes and asphalt, within a significant effort in limiting the use of fossil fuels.
2. For sectors where technology options are limited, in the net-zero emissions scenario, the remaining 20% of fossil fuel use in 2050 occurs in sectors where complete emission elimination is difficult. At that time fossil fuel will primarily be oil, continuing to fuel a number of sectors, especially the aviation industry.
3. Combine with CCUS technology, about half of the fossil fuel use in 2050 will occur in plants equipped with CCUS(in 2050, about 3.5 Gt of CO_2 emissions captured from fossil fuels).(IEA, 2021a)

CCS plays a significant role in reducing carbon emissions for several reasons, although renewable energy sources are considered as key solution to achieving the net-zero goal, the intermittent nature of it(such as wind and solar energy) is also a key challenge, so significant growth will likely require energy storage or use

of mixed energy systems(includes hydrogen and methane combustion). The supportive arguments as CCS are vital to achieving the reduction GHGs goal include: CCS provides a mechanism for both decarbonizing existing energy supplies and reducing emissions from industrial production(steel and cement for instance); CCS also enables faster and cheaper energy transition than using renewable resources; when deployed with bio-energy combustion, CCS can be used for projects with negative net carbon emissions (Ringrose, 2020).

Carbon dioxide is stored in the subsurface primarily for reducing greenhouse gas emissions into the atmosphere. Solar energy is absorbed in the atmosphere by greenhouse gases and the sunlight is reflected back down to the earth's surface. This heat on the ground will affect plant photosynthesis, cause evaporation of water, and result in an increase in melted snow and ice.

It is widely agreed that CCS, when combined with other methods (for example, biomass generation), is one of the most reliable technologies for lowering CO_2 levels in the atmosphere because of its ability to store large volumes of CO_2 while allowing economic development. Because it can potentially recover CO_2 emissions from fossil fuels, power plants, and industrial processes, it strategically prevents these industries from being decommissioned, slowed, or suffering redundancy (IEA, 2021b). The overview of CCS processing is shown in Fig 2.11.

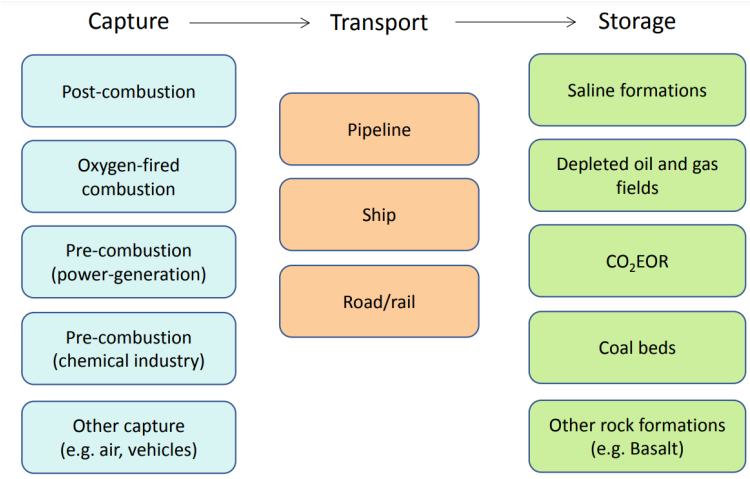

Figure 2.11: Overview of CCS technologies (Ringrose, 2020)

2.2.2 CO_2 capture

Carbon capture refers to capturing the carbon dioxide from point sources of gas emissions. Carbon dioxide can be captured from the chemical industry or from power generation. At the beginning of the CCS project, the main purpose of carbon capture is to separate the carbon dioxide from gas streams and concentrate the carbon for transportation and storage. There are several technologies used to capture the carbon, the main methods can be divided by pre-combustion, post-

combustion capture and oxygen-fired combustion capture (Ringrose, 2020)(Fig 2.12).

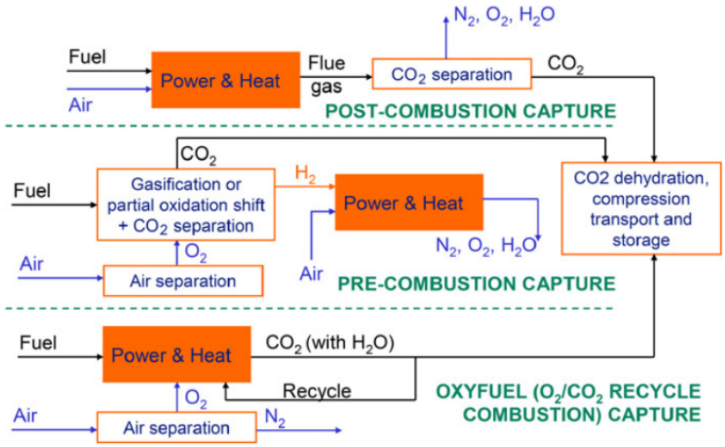

Figure 2.12: CO_2 capture process(Gibbins and Chalmers, 2008)

- Post-combustion capture Post-combustion capture technologies mainly focus on the removal of CO_2 from combustion gas streams, flue gas for instance. CO_2 is captured at low pressure and a flue gas with a low carbon dioxide concentration(3∼20%). The process involves two steps in general, energy conversion and CO_2 separation(Gibbins and Chalmers, 2008).
- Pre-combustion capture Pre-combustion capture technology operates on removing CO_2 from gas blends with a significant fraction of CO_2 in it. This technique includes CO_2 removal from industrial chemical processes and removal from natural hydrocarbon gas resources(Ringrose, 2020).
- Oxygen-fired combustion capture Oxygen-fired combustion capture technique is always applied to the process of combining the air separation and the denitrogenation. The nitrogen can then be removed from the air and the concentrated stream of CO_2 is produced to combust further(Gibbins and Chalmers, 2008).

2.2.3 CO_2 transport

CO_2 transport technology mainly includes the operation of captured CO_2 gas/liquid streams and the transportation of them to the storage site by pipeline, ship or tanker. Several reasons make the transportation of CO_2 become much more challenging technique than other transportation techniques: firstly, the thermodynamics properties of CO_2 make the transportation much more complicated, the CO_2-rich gas/liquid stream must be handled across phase transitions, which means the transport of gas, liquid and dense-phase can all occur in the CCS systems; secondly, the mixture of CO_2 and any aqueous phase can become corrosive and rise the risk of corrosion and leakage; thirdly, the captured streams are hardly

pure CO_2, various components make the CO_2 management complicated; finally, the techniques of CO_2 transport and flow assurance are not mature enough to handle all complex projects (Ringrose, 2020).

2.2.4 CO_2 storage

As the last stage for CCS technology, the safety of storage is significantly important, so it is crucial to select a safe site which can also optimize the capacity and storage period as well. There are several options to store captured CO_2, regarding the possible storage capacity, which can be summarized into 5 groups(Ringrose, 2020):

- Saline aquifer formations: in deep water-bearing reservoirs, the potential capacity can be extremely large.
- Depleted oil and gas reservoirs: after the oil and gas being extracted, the reservoirs can offer the storage sites which are always infrastructure, the depleted fluid pressure of that may also benefits for pressure management. Depleted oil and gas reservoirs usually provide great potential in the longer term
- CO2EOR: CO_2 is utilized in enhanced oil recovery(EOR), this method also has economic effect on developing the CCS technology by help facilitate the economics and growth of large-scale CO_2 capture and storage
- Coal bed: coal bed can be used in un-mineable coal seams storage or in enhanced coal-bed methane projects.
- Other rock formations: such as volcanic rocks, underground caverns, basalt formations,oil or gas bearing shale formations(Ringrose, 2020).

Geological Storage in Saline Aquifer

As platform 3 shown in Fig 2.13, this type of formation has great potential to store a huge amount of CO_2. The storage in a deep saline aquifer is mainly influenced by the properties of the aquifer, caprock as well as storage options. These factors are required to take into consideration before injection.

The storage is highly dependent on the aquifer's size and boundaries, which can control capacity as well, Fig 2.14 shows different storage systems. The open system is laterally open and vertically closed by caprock. The CO_2 is stored by water displacement, the water will mainly migrate laterally, and the storage capacity in this situation is around 0.5% The brine migration can lead to the pressure buildup to be slower in the open systems compared to closed systems, the pressure can propagate further in the layer (Bachu, 2015).

The storage capacity of the saline aquifer is affected by driving forces as well as CO_2 properties. The buoyancy and hydrodynamic forces control the CO_2 flow rate and the mobility between CO_2 and brine which leads to an increase in CO_2 and its spreading to the top of the aquifer, then storage efficiency is changed. Irreducible water and CO_2 saturation can change storage efficiency, capillary pressure

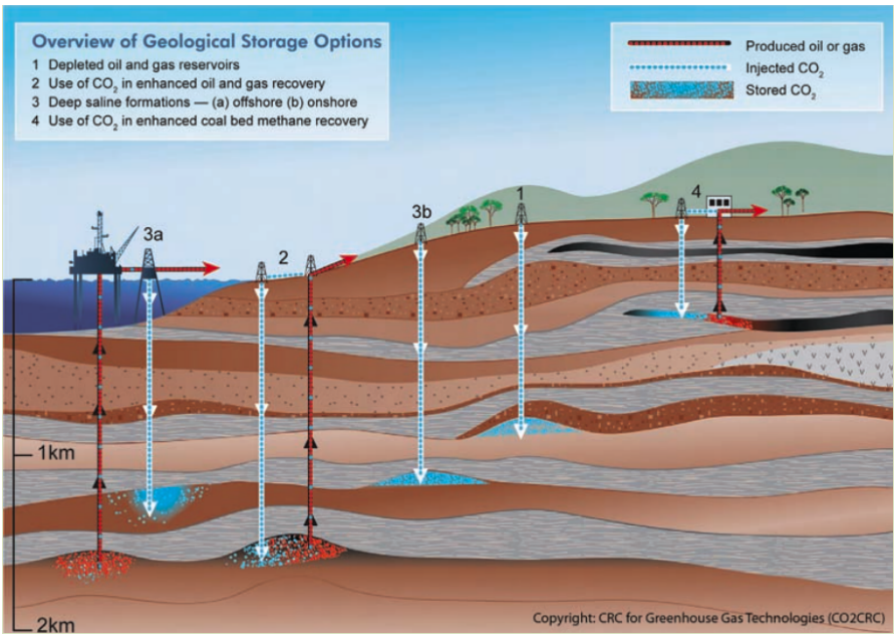

Figure 2.13: Overview of geological storage options for CO_2 (Ringrose, 2020)

in caprocks. The water proportion reduces and the storage capacity increases because of the increasing amount of pore space in the layers. Besides, the downhole pressure, formation temperature, salinity can affect the storage efficiency as well. The density and viscosity of CO_2 brine rise when pressure rises, temperature decreases, influencing the efficiency further(Bachu, 2015).

On the other hand, the permeability and capillary entry pressure can affect the storage efficiency,the low capillary pressure leads to CO_2 movement getting harder, thus improving the storage efficiency. From the perspective of well operations, numerous factors can change the efficiency, such as the injection period, rate and well numbers(Bachu, 2015).

Geological Storage in depleted oil and gas reservoir

Depleted oil and gas reservoirs are considered the most significant sites for storage. The reservoirs are always generated in porous basins such as sandstone and carbonate rock and overlying impermeable caprock such as shale and salt. The reservoir basin requires to have a proper porosity and permeability to have a good capacity in the pores, the caprock is important as well to keep the CO_2 injected in the subsurface for a long period. As platform 1 shown in Fig 2.13, the CO_2 is injected into a depleted oil and gas reservoir. Depleted reservoirs have lots of advantages for storage and can provide very readily available storage solutions, there are several reasons. Firstly, a large amount of data has been collected about these reservoirs that can be applied directly to understanding CO_2 storage dynamics; secondly, the depleted reservoirs can generally offer suitable pressure regimes for

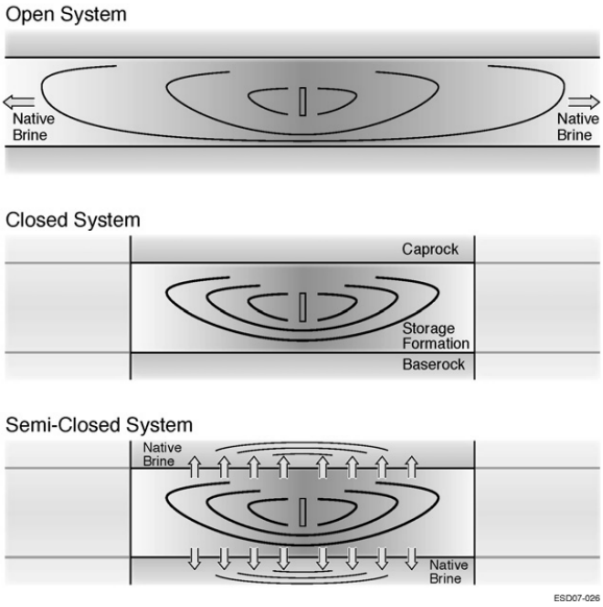

Figure 2.14: Sketch of open,closed, semi-closed systems around an injection well interval(Zhou et al., 2008)

the injection and storage; finally, the existing wells in these reservoirs allow access to the reservoir, which can improve the efficiency significantly(Cooper, 2009).

While there are still several factors that make the injection more difficult, such as when the project is designed to reuse the equipment, the operation costs may increase due to necessary improvements because of different practical situations, such as the higher pressure rating, corrosion-resistant material and updated pumping equipment. In addition, the injectivity pressure and temperature are also problematic to keep the CO_2 in a dense phase when injecting to the depleted reservoirs. Furthermore, the downhole pressure is also required to achieve to make the injection safer, which is also related to the property of CO_2. When CO_2 is injected in a dense phase, the hydrostatic pressure will increase and lead to the downhole pressure increases further. The difference between pore pressure and the injected CO_2 pressure can be problematic, especially the failure of reservoir and the reservoir cooling. When the flow rate is high, the reservoir can be cool soon, then the reservoir is brittle and easy fracture, the cooler reservoir will lead to a less dense CO_2, further reducing the storage of CO_2. When the injection pressure changes to an up-proper and high value, the reservoir and the caprock may also fracture. Moreover, containment is essential as well. During the production of hydrocarbon, the pore pressure decrease, then the pressure margin is available for re-pressurization, this may change the seal capacity, rock properties, thermal and chemical destabilization, so the CO_2 is more difficult to be stored. In addition, low pore pressure can lead to effective stresses increasing, then the rock of reservoirs is compacted, leading to a lower porosity and permeability(Loizzo et al., 2010).

2.2.5 CCS project phase

A CCS project is likely to consist of four distinct phases, as shown in Fig 2.15. The first phase is site selection and development, which may last 3 ∼ 10 years, the site is set based on geological evaluation, commercial factors as well as regulatory expectations. The subsurface storage space and surface facilities space all need permission, afterwards, the infrastructure is constructed and the operational capacity is verified. The second phase is Operation and it continues over decades, it refers to the entire period of injection and some additional monitoring. The third phase is closure, generally this phase can last over years, starts when the injected CO_2 is close to being well-managed, then the observations on wells or other facilities can be selected. At this stage, most wells are plugged and the infrastructure is removed. The final phase is post-closure, the well-established reservoir is expected to maintain for a very long time, and the operator is no longer involved (Cooper, 2009).

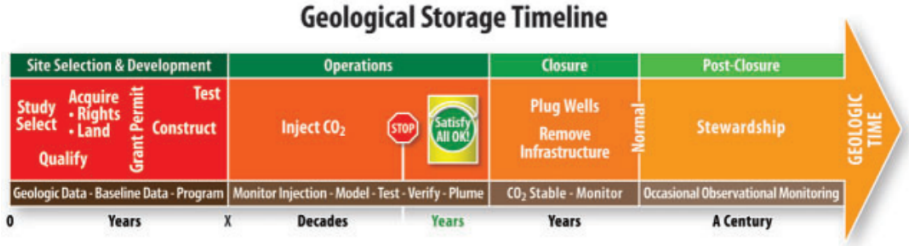

Figure 2.15: Four phases of CCS projects(Cooper, 2009)

The key issues about carbon storage include formation capacity, containment and injectivity:

- **Containment**
  A CO_2 storage site should be strictly sealed to prevent CO_2 leakage, it is useless and no meaning to store CO_2 if it migrates out of the formation and into shallow groundwater or the surface. Containment depends on several factors: rock distribution, pressure regimes, trapping mechanisms and seal geometry(Cooper, 2009). The storage sites are generally under 800m, whereas the units are always low-permeability or impermeable. The sealing rock always has a low permeability with 1 nD to 1 mD, so CO_2 is difficult to mitigate. The good caprock can be evaporites, shales, anhydrites, salt. When fractures and faults occur in the seal, the storage will be affected significantly. The faults can lead to CO_2 mitigation, and cause the leakage problem further. So pressure management is required to prevent the generation of faults and fractures, since when pressure rises up to be higher than the fracture pressure, the subsurface situation will change(Cooper, 2009).
  The formation containment is also influenced by the trapping mechanisms and fluid flow. During gas migration, residual gas saturation may occur when there is a buildup of immobile gas in the porous medium. CO_2 moves

because of the density differences between formation fluids, the CO_2 amount is reduced by this mechanism due to accumulation in pores(Ringrose, 2020).

- **Capacity**
  The capacity of the storage unit is determined by formation thickness, porosity, CO_2 density, the area size of storage structure and storage efficiency. The thickness is determined by the porosity, the higher porosity offers a large storage capacity of CO_2 in the formation. The CO_2 density increases with depth in general, then the CO_2 density tends to liquid at the storage depth. A great volume can be reached when CO_2 is in super-critical phase(Cooper, 2009). The storage efficiency is affected by buoyancy, heterogeneity and sweeps efficiency in the storage unit, the pore volume in practical cases is assumed to be saturated with CO_2 in a range of 0∼5%(Ringrose et al., 2017). The pressure limitation, size of storage and other factors can also limit the storage capacity, this thesis will discuss this in Chapter4. The estimation of capacity can be summarized into four classes, as Fig 2.16 shown:

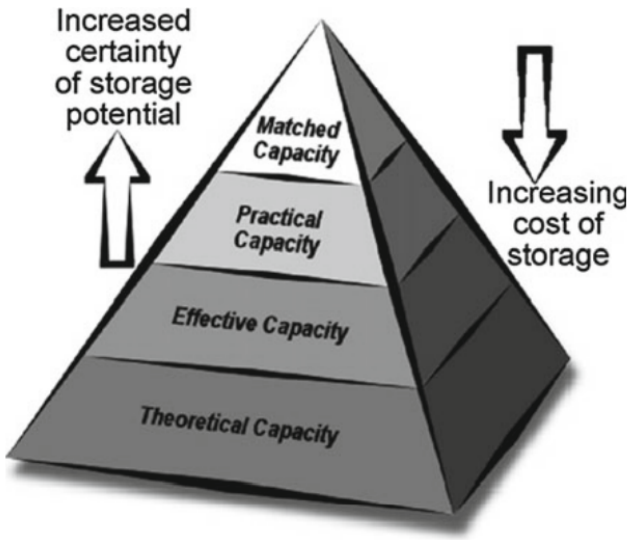

Figure 2.16: Techno-economic resource–reserve pyramid for discussing CO_2 storage estimates(Bachu et al., 2007)

The theoretical capacity is identified by the physical limit of the storage site, the effective capacity refers to an estimate using cut-off criteria, practical capacity includes consideration of economic, technical and regulatory factors, the matched capacity means the site-specific storage for specific projects(Bachu et al., 2007).
The theoretical approach to estimate the capacity is simplified to the calculation of trap,porosity and saturation:

$$V_{CO_2} = V_{trap}\phi\,(1 - S_{wirr}) \tag{2.1}$$

V_{trap} is the trap volume, ϕ is porosity and V_{wirr} is the irreducible water sat-

uration, while in sandstone system the net to gross ration is also applied to calculate. Residual-phase storage can also occur in the structural closures, whereas CO_2 migrates from deeper storage unit through the porous medium. The storage can be estimated by :

$$V_{CO_2} = V_{swept}\, \phi\, S_{CO_2R} \tag{2.2}$$

V_{swept} refers to the volume contacted by migrating CO_2, S_{wirr} refers to the saturation of residual CO_2. When considering the effects of fluid dynamics, the CO_2 can fill the available pore space in the formation, then storage efficiency factor ε is introduced to the calculation(Ringrose, 2020), this factor describes the ratio of the actual volume of CO_2 stored in aquifer volume to the estimated pore volume, indicates the cumulative effects of heterogeneity, fluid segregation as well as the sweep efficiency(van der Meer, 1995). Thus the total injection mass of CO_2 in the saline aquifer is shown as:

$$M_{CO_2} = V_\phi\, \rho_{CO_2}\, \varepsilon \tag{2.3}$$

Further, the general function of CO_2 mass is defined as:

$$M_{CO_2} = V_b\, \phi\, N/G\, \rho_{CO_2}\, \varepsilon\, (1 - S_{wirr}) \tag{2.4}$$

- **Injectivity**
  Injectivity is defined as the storage characteristics show the amount of CO_2 injected from the wellbore, which is related to the permeability of the formation, the high permeable formation means the fluid flow rate is high because the pores are well connected. Thus CO_2 storage sites need to construct in a highly permeable zone near the wellbore, then the CO_2 can access the pores more efficiently. While sometimes high-permeable formations mean the pathways connected to pores can lead to the migration of injected CO_2, the storage site then loses the storage safety and efficiency, the formation is not an ideal option for storage anymore. In addition ,the geochemical reaction of injected CO_2 and surrounding rocks in the subsurface can also influence the formation permeability (Cooper, 2009), then injectivity becomes more complicated to estimate.

2.2.6 Trapping mechanisms

Trapping mechanisms can be classified to physical and chemical factors. The physical trapping mechanisms include basin-scale processes, fluid dynamic processes and geometry of structural and stratigraphic traps. The geochemical trapping mechanisms mainly include CO_2 dissolution in the brine phase, CO_2 precipitation as mineral phases and CO_2 sorption/absorption. As Fig 2.17 shown, various trapping mechanisms require to work together to increase storage security which changes with time. Physical mechanisms trapping has the most significant effect in the first years after injection, the importance of solubility and mineral trapping

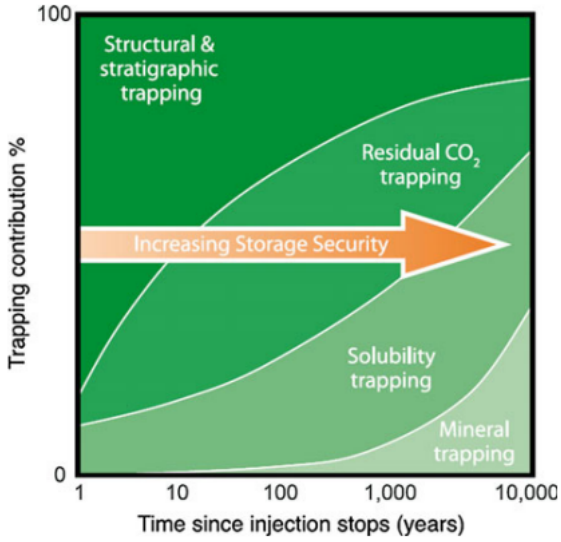

Figure 2.17: CO_2 storage trapping mechanisms(Ringrose, 2020)

is increasing gradually to fix long-term CO_2 storage in the subsurface(Ringrose et al., 2017).

- **Physical trapping mechanisms: Structural and stratigraphic**
  Initial trapping mechanisms controlled by the rock architecture of the storage complex appear below caprocks with low permeability and high capillary pressure. In the early period, these mechanisms is the most dominant for securing storage, similar to hydrocarbons or saline brine accumulation in reservoirs. The closed structures in sedimentary basins can store CO_2 in the subsurface. Because of the combination of permeable and impermeable structures and rocks, these traps always can prevent CO_2 migration, so the storage is safe and efficient. The stratigraphic traps are formed by rock properties change,including lateral facies changes, pinch-outs and unconformities. The variation of facies includes the areas, where permeable and impermeable layers are alternated, preventing the formation fluid migration. In the presence of pinch-outs and unconformities, porous and permeable materials are directly contacted by low-permeable layers(Cooper, 2009).
  The structural traps contain different faults and anticlines, faults can serve as preferential pathways for fluids, or enclose the structure, preventing the migration of the fluids. The anticlines include folds surrounded by impermeable rocks, which makes the storage available in the structures(Cooper, 2009).
- **Physical trapping mechanisms: Fluid flow processes**
  Driven by hydrodynamic, the fluid flow processes occur in saline formations without a closed trap, the fluids can move slowly over long distances. During the injection, the saline water is likely to be displaced by CO_2 on the top,

since the density of CO_2 and brine is different, the gravity force leads to the movement. Afterwards, CO_2 may keep migrating as a separate phase on top of the formation until it can be trapped in stratigraphical or structural traps in the layer or reach residual CO_2 saturation in regions where the brine already takes place of injected CO_2, then CO_2 dissolve in the formation water gradually. The low permeability and low porosity can lead to the pores be narrow in the caprock, small pore throats can generate a capillary seal and prevent the movement of CO_2, then CO_2 is trapped by the caprock. As the figure 2.18 shows, the small pores in the caprock make the migration of CO_2 from the reservoir to the seal difficult. Further, the caprock consists of formation water which can create the inter-facial tension between the CO_2 and brine, together with the capillary force, the CO_2 is trapped in the reservoir(Cooper, 2009).

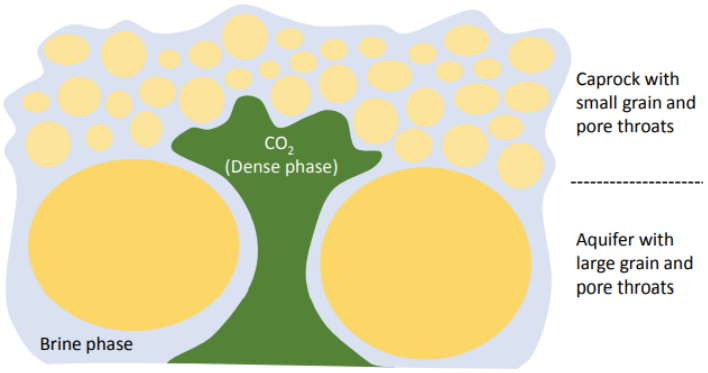

Figure 2.18: Sketch of capillary trapping of a CO_2 phase in super-critical (dense) phase in a completely water-wet porous medium. Due to smaller pore throats of caprock with small grains compared to larger pore throats in the aquifer, the gas column will rise quite slightly(Ringrose, 2020)

- **Physical trapping mechanisms: Residual trapping**
  Residual trapping is driven by fluid flow as well, during the CO_2 migration, the proportion of CO_2 and brine will change. When the water saturation increases, the CO_2 saturation decreases, then gas trapping happens in the layers. The trail of residual gas rises due to buoyancy is shown in figure2.19. Several factors influence the trapping degree, including the size of the pore throat, interfacial tension and wettability. In general, the assumption is CO_2 behaves as a nonwetting phase in sandstone reservoirs, while in some cases practical wetting behaviour may occur, especially for carbonate and clay surfaces. In addition, the angle is also controlled by the pressure, temperature as well as the fluid components(Ringrose, 2020).
- **Geochemical trapping mechanisms: CO_2 Dissolution**
  The differences between the CO_2 density and brine density lead to the CO_2 migration, plume then appears because of CO_2 accumulation, which can

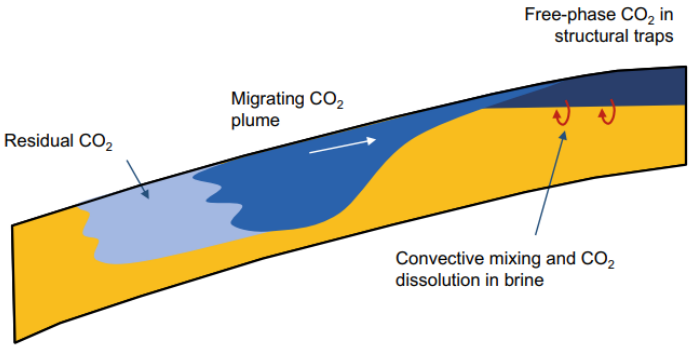

Figure 2.19: CO_2 storage flow processes(Ringrose, 2020)

laterally extension in impermeable caprock, some CO_2 will be dissolved in formation brine during the migration, as Fig 2.20 illustrated. In the plume, the brine and CO_2 both exist, causing the dissolution to be in equilibrium, thus in the aquifer, when the proportion of water exceeds CO_2 the dissolution is slow. The CO_2 dissolution in the brine phase is the most essential geochemical reaction, the influences of it can vary a lot in the aquifer.

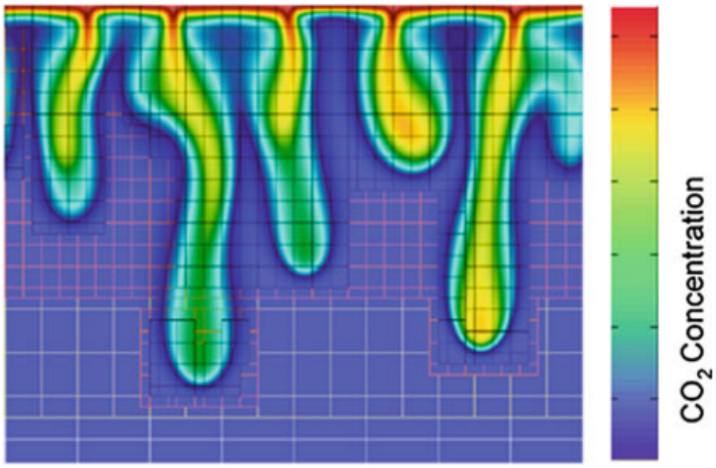

Figure 2.20: Sketch of the CO_2 sequestration process in a simple geometry(Pau et al., 2010)

- **Geochemical trapping mechanism: mineral trapping**
  The CO_2 dissolution in formation water can produce weak carbonic acid which causes chemical reactions with the surrounding minerals and generate solid carbonate minerals, such as sodium, magnesium, iron carbonate, potassium basic silicate as well as silicate minerals. This process is affected by the acid concentration, and it can increase the storage efficiency(Cooper,

2009).

- **Geochemical trapping mechanism: CO_2 sorption/absorption**
  CO_2 can be absorbed on the interface, this process generally occurs when injecting into a coal-bed formation. This absorption can lead to the coal swell and highly affects the storage efficiency further. Fig 2.21 illustrates the absorption process in clay minerals.

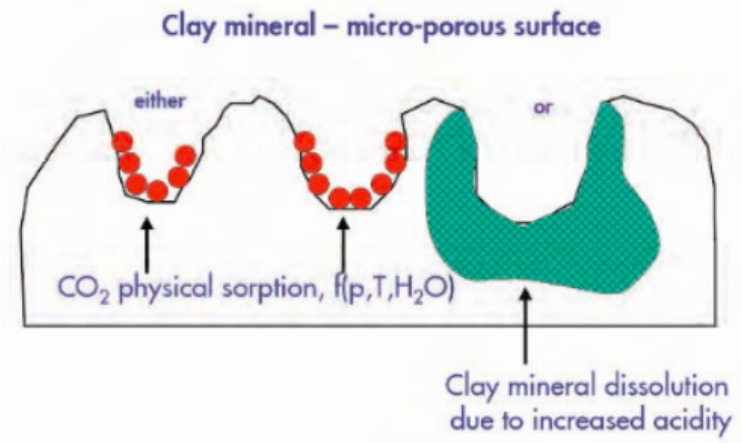

Figure 2.21: CO_2 absorption in clay minerals(Cooper, 2009)

2.3 Smeaheia CO_2 storage site

2.3.1 Geological Setting of the Smeaheia

This section is modified from my semester project, Large-scale CO_2 injection: Pressure decay in multiple compartments and optimization of long-term basin pressure(Guo, 2021)

Offshore areas are seen as the best choices for providing a large storage capacity. The Northern North Sea is one of the most essential hydrocarbon production areas in the world. The Horda Platform is located north of 60°N to the south of 62°N and is a north-south trending structural high along the eastern margin of the Northern North Sea. It is bounded by two N-S trending fault zones: the Øygarden Fault Group to the east and the Mokkurkalve Fault Group to the west. After the discovery of Troll Field in 1979, numerous exploration activities was made in the Horda Platform area. It contains two major extensional events, the Permo-Triassic rifting and the Late Jurassic-Early Cretaceous rifting(M. J. Mulrooney et al., 2020).

The study area mainly covers the Smeaheia area and the eastern margin of the Troll East area. The Smeaheia prospect is located in the eastern margin of the Horda Platform, around 20∼35 km offshore Western Norway. Smeaheia is a fault block at the eastern margin of the platform, there are two main fault systems in the prospect, Vette Fault System and Øygarden Fault System. These main faults dip towards the west, bounding major half–graben basins(Wu et al., 2021).

The essential potential storage units in the Horda Platform are the Middle-Upper Jurassic Sognefjord , Fensfjord and Krossfjord formations and deeper Lower Jurassic Johansen Formation. For the Smeaheia prospect, Viking Group is the main storage group , the coastal shallow-marine sandstone from the Sognefjord Formation, the Fensfjord Formation and Krossfjord Formation is interfingered with the shaly Heather Formation in the Horda Platform, the total thickness of three formations are approximately 400∼500 meters(NPD, n.d.), as shown in Fig 2.23. Each formation has been interpreted in terms of a “forestepping to backstepping” rift marginal wedge. This pattern has been interpreted as the response to eustatic sea-level changes or basin-wide changes in sediment supply, but also as a response to three separate rift eventsNPD, n.d.In the Smeaheia area, two storage prospects have been identified, Alpha and Beta (Fig 2.22), which are formed by footwall and hanging wall three-way structural closures respectively. The Upper Jurassic marine claystones of the Draupne Formation are acting as the seal to the prospects(Skurtveit et al., 2012).

2.3.2 Reservoir Formations

The Sognefjord delta aquifer consists of the Krossfjord formation, Fensfjord formation and Sognefjord formation, partly separated by thin shale from Heather formation.

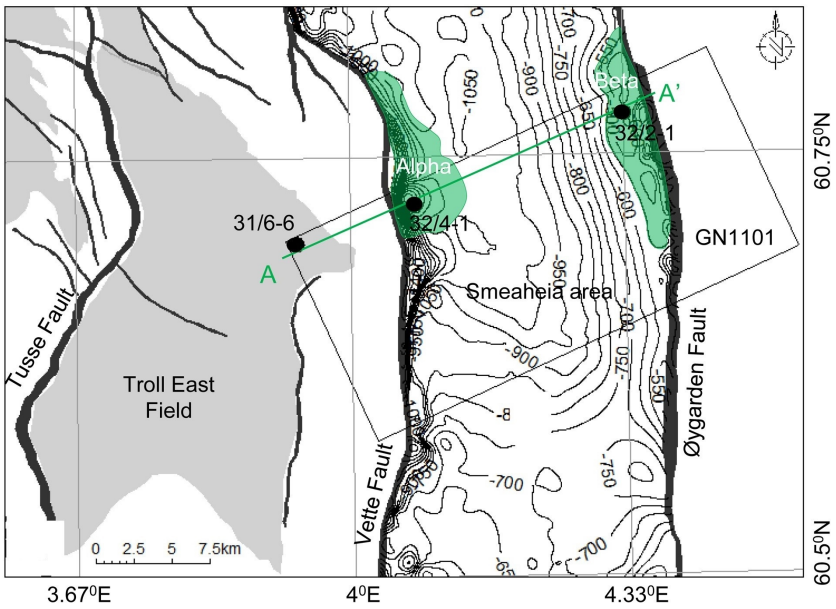

Figure 2.22: The depth structure map of the study area
The depth structure map of the top reservoir unit (Sognefjord Formation) is interpreted using the well tops showing the major faults and Troll East Gas Field in the study area(Rahman et al., 2021)

- **Sognefjord Formation**
  The Sognefjord Formation consists of sandstones and sands,well sorted and friable to unconsolidated, medium to coarse grain size and colored from grey to brown. Locally the formation is weakly micaceous with minor argillaceous and carbonaceous beds, bioclastic material as well as cemented occur locally. Sediment is mainly from Oxfordian to Kimmeridgian/Volgian ages, the formation was deposited in a coastal shallow marine environment. The fine-grained sediments within the formation have porosity between 15% and 25% and the coarse-grained, clean sandstones have porosities up to 38%. The boundaries of the Sognefjord Formation are lower because of the interdigitation of sandstones with silestones from the upper Heather Formation. The well logging of gamma ray shows several cycles displaying "funnel-shaped" coincident with coarsening upward sequences in the upper half of the formation. The top of the formation is the distinct lithological break into claystones or shales(NPD, n.d.).
- **Fensfjord Formation**
  The Fensfjord formation consists of sandstones, well sorted and moderately friable to consolidated, colored from grey to brown. In calcite cemented sandstone beds, generation of bioclasts may occur and occasionally carbonaceous and micaceous layers. Shale intercalations also occur throughout locally. The deposits are formed in a coastal, shallow marine environment in the Callovial age and the sediments include small coarsening upward

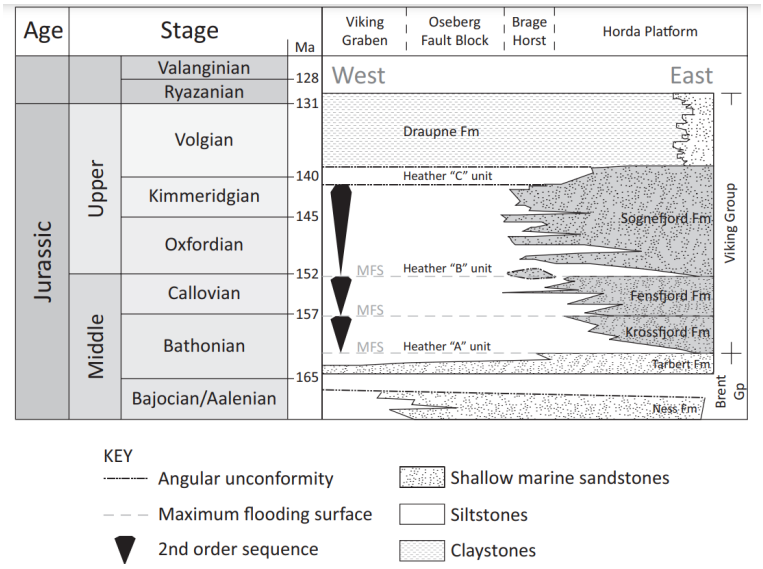

Figure 2.23: The chronostratigraphic framework for the Viking Graben and Horda Platform

SW-NE oriented cross-section of chronostratigraphic framework for the Viking Graben and Horda Platform.(Holgate et al., 2013)

units which contain fine micaceous sands at the bottom and become coarse sands to the top of formation(NPD, n.d.), and the porosity is between 15% and 35%. The formation is underlying the Krossfjord Formation, the top of the Fensfjord Formation is characterized by a transition of the lithology distinguished by gamma-ray log(NPD, n.d.).

- **Krossfjord Formation**
  The Krossfjord Formation consists of sandstones, well sorted and loose to friable, medium to coarse-grained, colored in light grey-brown in total, the sandstone is transparent to translucent,subangular to subrounded, spherical to subspherical, slightly calcareous to calcareous, micaceous and pyrite in places. Cement occurs occasionally, the lower portion of the formation is slightly argillaceous and carbonaceous with minor shale intercalations and overlying Heather Formation siltstones and sandstones(NPD, 1985). The formation was deposited in a coastal shallow marine environment and deposits in the Bathonian age. The upper and lower boundaries are the Heather Formation and Fensfjord Formation occasionally when the Heather formation is absent. In the Troll Field, the formation is characterized by progradation of a sand-rich delta during relatively low rates of normal faulting and fault-block rotationNPD, n.d. The Krossfjord Formation is comparatively thin with high average porosity and a relatively higher permeability than Sognefjord Formation and Fensfjord Formation(NPD, 1985).

2.3.3 Caprock

The Draupne Formation acts as the sealing part of the storage site. The formation mainly consists of non-calcareous, carbonaceous and locally fissile claystones, colored in dark grey-brown to black. From the logging reports, the formation can be marked by high radioactivity because of the organic matter inside, the velocity and density log results are anomalously low, the resistivity log value is high. In basinal areas, the formation overlies the Heather Formation in general, while it onlaps the pre-Upper Jurassic rocks on the marginal high regions. On the northern part of the Horda Platform, the base is marked by the Sognefjord Formation, the upper boundary is unconformity or discontinuous, overlain by the sediments from Cretaceous, it can be marked by well logging data with a higher velocity and low gamma-ray response value. The formation was deposited in ranges from Oxfordian to Ryazanian ages in a marine environment with restricted bottom circulation and often with anaerobic conditions. The sandstones may generate from turbiditic origin(NPD, n.d.).

2.4 Case Studies Used

This section is modified from my semester project, Large-scale CO_2 injection: Pressure decay in multiple compartments and optimization of long-term basin pressure(Guo, 2021)

2.4.1 Smeaheia

The feasibility assessment designated the Smeaheia location as a suitable storage site because of its good reservoir features, low implementation and technical risk, significant storage capacity with the potential to enhance storage volume, and infrastructure of two exploratory wells. CO_2 could be stored in the Alpha structure, which is part of a massive fault block east of Troll, as shown in Fig 2.22. This structure may store around 100 million tonnes of CO_2 at original reservoir pressure before migration to the neighboring Beta structure, which Statoil also assessed. Statoil looked into injecting in both the Sognefjord and the deeper Fensfjord formations. Reservoir models demonstrate that rates much beyond the 200 tonnes/hour employed as a basis in the development solutions are attainable in targeted formations, implying that only one injection well is required. The Draupne Group has a very good primary seal that is overlain by a series of shallower, tighter shale strata. With two exploratory wells and both 2D and 3D seismic, the database is solid(GASSNOVA, 2016).

2.4.2 Snøhvit

The data from Snøhvit project is also applied in this report as a reference to the model built-up.The Snøhvit Field is located in the Barents Sea, around 150 km north of the coast of Norway, at 71^o north.

The Snøhvit project came on stream in August 2007, the gas production started in August 2007. The installations are all sub-sea in the water depth of approximately 290-350 m. The CO_2 injection started in April 2008. After the gas was produced, the unprocessed gas stream was transported in pipeline 150 km to the onshore Melkøya LNG plant. The injection pressure immediately rose to the pre-stop injection pressure level during injection start-up. There was a reduction in reservoir pressure while the drop was not as rapid as the reservoir model indicated. Further continuous and stable injection at high rates (80 tonnes/hr) increased the pressure further. The reservoir model was updated and the new predictions led to action as the pressures approach the estimated rock fracture pressures. After some analysis and actions, the Tubåen Formation storage site was sealed at a shallower level and alternate solutions are used(Hansen et al., 2013).

2.5 Pressure Theory

2.5.1 Pore Pressure

Pore pressure is identified as the fluid pressure in pore spaces of the porous formation. As Fig 2.24 shown, the pore pressure is hydrostatic at relatively shallow depth (less than 2000 m), indicates that a continuous, interconnected column of pore fluid extends from the surface the interests the depth. In the deeper depth, the overpressure occurs, the pore pressure rising with the depth rapidly, indicates that the deeper formations are hydraulically isolated from the shallow part. Below the depth about 3800 m, the pore pressure can approach to a value around the overburden stress, implying the hard overpressure condition (Zhang, 2019).

In the practical petroleum drilling industry, the pore pressure gradient is generally used to determine the mud density because of the convenience. As Fig 2.25 shown, the pore pressure gradient is defined by the pore pressure divided by the TVD (true vertical depth), then the mud density can be selected properly on the basis of pore pressure gradient, wellbore stability and fracture gradient. The proper mud pressure is required to prevent the influx and wellbore collapse during drilling. In some open hole cases, the heavier mud pressure than the pore pressure is needed to avoid the fluid influx and the instability of the wellbore. But when fracture gradient is reaching, the formation may break, leads to the mud losses or even the circulation lost(Zhang, 2019).

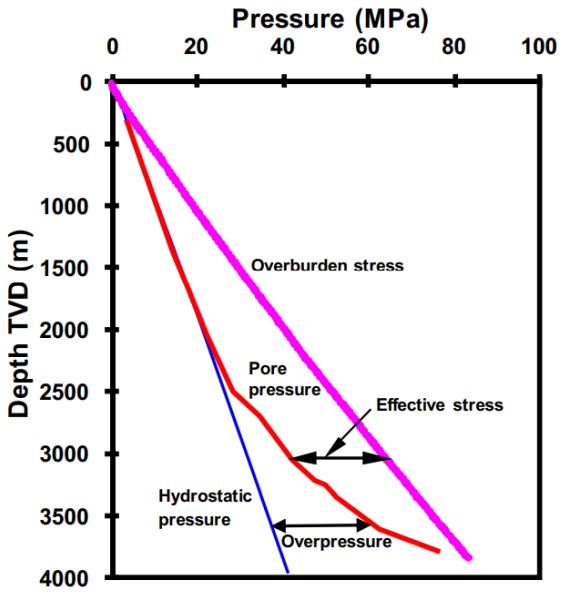

Figure 2.24: Hydrostatic pressure, pore pressure, overburden stress, and effective stress in a borehole

TVD is the true vertical depth. (Zhang, 2019)

2.5.2 Fracture Pressure

Fracture pressure P_{frac} refers to the fluid pressure which fracture the rock formation, usually leads to a dramatically increasing in permeability due to the induced fractures. It is defined as the function of the rock stress state and generally increases with depth (fracture pressure gradient). The rock stress state is defined as three principal stresses, the most common situation for sedimentary basins, the vertical stress σ_V is the largest stress, the horizontal stresses σ_H is close to isotropic or weakly anisotropic. To simplify the model, the case is considered as a vertical, where the maximum principal stress is vertical, the horizontal stress field is isotropic. The two most commonly used methods for fracture pressure definition, minimum stress and the tensile failure methods, give the lower bound and the upper bound of fracture pressure respectively(Bohloli et al., 2017). To calculate lower bound of fracture pressure, the minimum stress approach is defined by Eq 2.5. This approach is under the assumption of isotropic horizontal stress and ignore the tensile strength of rock mass and the thermal stresses.

$$P_{FPmin} = \sigma_{min} = \frac{\upsilon}{1-\upsilon}(\sigma_V - P) + P \tag{2.5}$$

In the equation, σ_{min} refers to the minimum in-situ stress, P represents the pore pressure, υ refers to the Poisson ratio. To calculate the upper bound of fracture pressure, the tensile failure method is applied based on a vertical well-bore, with maximum horizontal stress σ_H, thermal stressσ_T and tensile strength of rock T_0. Then the equation is defined as Eq 2.6:

$$P_{FPmax} = 3\sigma_{min} - \sigma_H - P - \sigma_T + T_0 \tag{2.6}$$

When neglecting tensile strength and thermal stresses, assuming isotropic horizontal stress, the equation can be simplified as equation (2.7):

$$P_{FPmax} = \frac{2\upsilon}{1-\upsilon}(\sigma_V - P) + P \tag{2.7}$$

For any subsurface injection, the maximum allowable injection pressure P_{max} can be calculated from the mechanical strength of the confined or semi-confined cases, so as to estimate the fracture pressure of confining rock units. The P_{frac} is complicated to calculate because of complex stress field, the borehole orientation and the in-situ properties. In this study, based on several assumptions, the upper bound estimation Eq 2.7 of fracture pressure is applied, which is more proper to vertical wells in sedimentary basins (Ringrose and Meckel, 2019).

2.5.3 Overburden Stress

Overburden stress (vertical stress) is caused by the mass of overlying formations. There are several methods to calculate the overburden stress, from bulk density or from empirical equations. If the average density of overlying formation and the depth are known, the overburden stress can be calculated by Eq 2.8, while when

the bulk densities of the rocks change with depth, the integration of densities to the interest depth is used to calculate the stress, defined by Eq 2.9. $\rho_b(z)$is the function of formation bulk density varies with depth, it can be collected from density log. ρ_w is the density of sea water, Z_w is the water depth(only if in offshore drilling, for onshore drilling, Z_w=0)

$$\sigma_V = \rho_a g Z \tag{2.8}$$

$$\sigma_V = \rho_w g Z_w + g \int_{Z_w}^{Z} \rho_b(z) dz \tag{2.9}$$

In some shallow depth cases, the density log is usually not reliable to record the value, some empirical approaches are applied to estimate the shallow formation bulk density in order to obtain the depth-density curve.

For offshore drilling, empirical equations are used as well, the formation overburden stress gradient is always obtained from different well logging data, there are several equations calculated from numerous wells.

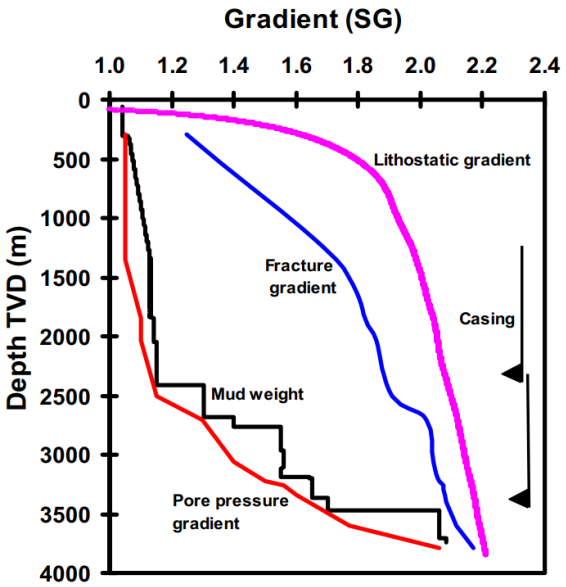

Figure 2.25: Pore pressure gradient, fracture gradient, overburden stress gradient (lithostatic gradient), mud weight, and casing shoes with depth.

In this figure pore pressure and overburden gradients are converted from the pore pressure and overburden stress plotted in Fig 2.24 (Zhang, 2019)

2.6 Basin Fluid Delta-pressure Approach

This section is modified from my semester project, Large-scale CO_2 injection: Pressure decay in multiple compartments and optimization of long-term basin pressure(Guo, 2021)

The "basin fluid delta-pressure analysis approach" is based on the generic approach of pressure and stress trends in the offshore sedimentary basins, summarized from different offshore basins with well-knowledge over decades. The storage capacity can be obtained by the pressure changes in a known area. In order to evaluate the pressure changing in the injection process, several assumption conditions are used to simplify the model. Assuming the non-infinite saline aquifer with barriers, the capacity will be limited by pressure based on the fluid dynamics of open systems(Ringrose and Meckel, 2019). The pressure change is one of the key factors which dominate the capacity. The delta-pressure is identified by the difference between the bottom-hole well pressure and the formation pressure. For the purpose of exploring the maximum storage capacity, a maximum allowable well pressure is set as a limit, an initial formation pressure is defined as well, which is closely related to the depth. Thus, to analyse the pressure, depth is the first factor to consider.

In the shallow interval of geological basins with a depth of $2 \sim 3$ km, the hydrostatic pressure always develops with depth into naturally over-pressured systems, which is essentially controlled by the natural balance between the compaction rate and the fluid pressure dissipation rate. So for the initial pressure, the hydro-pressure can be used to estimate the value in the shallow area, $P_{hydro} = P_i$; for the deeper area of the basins, generally, the initial pressure is larger than the hydro-pressure. In this approach, the shallow interval is mainly used.

While the geomechanical strength of the aquifer(confined or semi-confined) will add a limitation to the maximum injection pressure as P_{max}. When the pressure increases and approaches the lithostatic pressure gradient, the rock fracture pressure P_{frac} as the limiting pressure is reached is complex, which depends on the stress field, the borehole orientation and rock properties(in-situ), as shown in Fig 2.26. The value of it is close to the minimum in-situ stress component σ_3 of the stress tensor. As discussed in Section 2.5.2, the equation of fracture pressure is defined as Eq. 2.7 :

$$P_{frac} = \frac{2\upsilon}{1-\upsilon}(\sigma_V - P) + P$$

υ - Poisson ratio
σ_V - Vertical overburden stress
P- Pore pressure

Injectivity is depending on numerous conditions, such as the well design, the placement strategy of the well, the reservoir formation properties. In order to quantify the gas injection, firstly the injectivity index II is introduced, for the

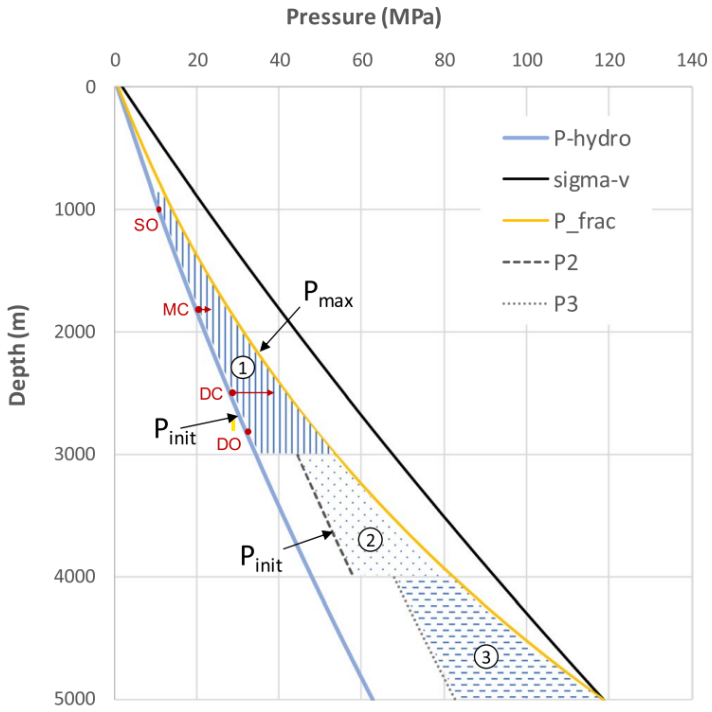

Figure 2.26: Pressure depth functions(Ringrose and Meckel, 2019)
Pressure depth functions for a generalised Norwegian North Sea basin case illustrating the shallow normally pressured region (1), and the progressively deeper and more overpressured regions (with excess initial pressure P2 and P3). P_{hydro} is the hydrostatic gradient, sigma-v is the vertical principal stress, and the maximum reservoir pressure is described by the formation fracture pressure P_{frac}.(Ringrose and Meckel, 2019)

simplest case, the equation to calculate index is described as

$$II = \frac{q}{P_{f\,bhp} - P_{res}} \tag{2.10}$$

q - Flow rate
$P_{f\,bhp}$ - Flowing bottom-hole pressure
P_{res} - Far-field reservoir pressure

This equation is on the basis of that the injection fluid is in-compressible. For the gas injection, the P^2 technique is used, the injection index for gas with the assumption of vertical well(Ringrose et al., 2017) is described as:

$$II_{gas} = \frac{q}{P_{f\,bhp}^2 - P_{res}^2} \tag{2.11}$$

For the CO_2 injection, neglect the skin effect, the equation can be simplified as

$$II_{CO_2} = \frac{q_{CO_2}}{P_{f\,bhp} - P_{res}} \tag{2.12}$$

In practice, the CO_2 injection calculated is more complex, other factors also influence the injectivity as well, such as the near-wellbore effects, the temperature varies with time and depth and the long term far-field reservoir pressure change as well. Adaption the equation for radial flow around a wellbore to create an integral function for the flow rate during the lifespan of the injection wells in the time interval i to f to generalize the long-term performance of an injection well in a saline aquifer(Ringrose and Meckel, 2019):

$$\int_i^f q_t = \frac{2\pi k_a h_a}{\mu \ln\left(\frac{r_e}{r_w}\right)} \left[\int_i^f (P_{well} - P_{res})\right] \tag{2.13}$$

k_a - the permeability of the aquifer formation
h_a - the height of the injection well interval
μ - CO_2 viscosity
r_e - the effective radius of the reservoir unit
r_w - the radius of the well

Use I_c to denote a constant equivalent to the mean injectivity index, replacing the part of the argument multiplied before the integration function. Then considering the flux boundary conditions of the injection well, the flux term is added into this equation, which is represented by F_b:

$$V_{\text{injected}} = I_C \int_i^f (P_{\text{w}} - P_{\text{res}}) + F_b \tag{2.14}$$

The integral of pressure function with time is related to the formation properties and the dimensions of the storage units. Generalized from the real cases, the pressure function always follows a characteristic function of time, then the dimensionless pressure function can be described as equation below:

$$P_D(t_D) = \frac{1}{2} ln(\frac{4t_D}{\gamma}) \tag{2.15}$$

P_D - Dimensionless pressure
γ - Euler's constant, equals to 1.781

Coefficient $\frac{1}{2}$ in this equation may be assumed on account of the reservoir boundary conditions. The compressibility is also neglected in this equation while it's embedded in the P_D function. Then the real dimension of pressure is obtained:

$$P_{res}(t) = P_i + AP_D(t_D) \tag{2.16}$$

A is the scaling parameter related to the reservoir characteristic, which will be illustrated further in the following chapters. For the injection cases, using the upper boundary of the fracture pressure, setting in vertical wells in a sedimentary basin, the general injection volume is described as the function with pressure bounds:

$$V_{project} = I_c[P_w - P_i + \int_i^f AP_D(t_D)] + F_b \tag{2.17}$$

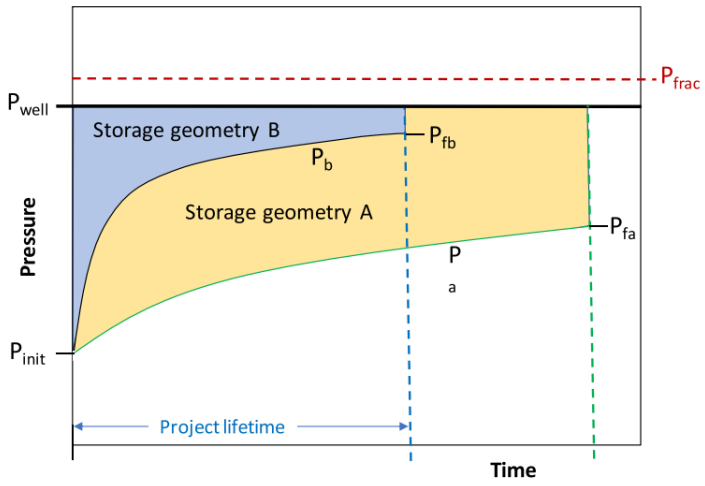

Figure 2.27: Idealised project lifetime pressure varies with time
Idealised project lifetime pressure plots for two contrasting aquifer units assuming the same initial pressure conditions (Ringrose and Meckel, 2019)

Four injection-well model scenarios are also presented by the article(Ringrose and Meckel, 2019) to illustrate the different CO_2 injection projects at different stratigraphic depth and contrast reservoir conditions:

(a) A shallow open-boundary case (SO) with injection at 1000m depth and with no significant pressure constraint;

(b) A moderate-depth, partially-closed pressure boundary case (MC) with injection at 1800m depth;

(c) A deep closed-boundary case (DC) with injection at 2500m depth;

(d) A deep open-boundary case (DO) with injection at 2800m depth and with no significant pressure constrain.(Ringrose and Meckel, 2019)

In basis of the models parameter setting and historical injection data, the deep closed boundary case approaches to the pressure limitation before the designed well lifespan of 25 years, leading to only 5.1 Mt CO_2 stored when project closure in the 16th year. The parameter assumption of this model will be illustrated further in the chapter afterwards as the major basement of the analysis.

2.7 Simple Analysis of Rock Compressibility Limits

This section is modified from my semester project, Large-scale CO_2 injection: Pressure decay in multiple compartments and optimization of long-term basin pressure(Guo, 2021))

The bulk compressibility equation is given by Eq 2.18, with an assumption of a constant temperature(Ringrose, 2020).

$$C_b = -\frac{1}{V_b} * \frac{dV_b}{dP} \tag{2.18}$$

$$V_b = \phi * V, dP = P_f - P_i \tag{2.19}$$

V_b is defined as the pore volume of the rock, dV_b is the pore volume change caused by the compression, the dP inside is defined by the difference of initial pressure and final pressure before and after injection. The C_b is always in the range of 10^{-11} to 10^{-9}Pa^{-1} .

To incorporate this equation into this study, the box method is used: after constructing the box model in the assumed size area, Eq 2.18 is used to calculate the dV_b within the given range of C_b, and the result can then be transformed into the injectivity, establishing a relationship with the basin fluid delta pressure method. This procedure is detailed in the following chapter.

Chapter 3

Method and Data

3.1 Box Method

The injection volume of CO_2 is related to the prospect formation volume and the rock properties, such as the lithology, porosity, permeability, viscosity and compressibility. To obtain a direct view of the underground situation, the box solution is introduced to get a simplified subsurface model. As the different rock compartments can be regarded as different boxes, the sizes of these boxes are determined by setting their scales in x,y,z dimensions. The parameters regarding the rock properties are identified by the practical cases. The fundamental of this solution is the compressibility Eq 2.18, the geometry variables are the size of the area and the thickness(height) of the formation(box), rock property parameters include porosity and bulk compressibility, while the solution is mainly controlled by the pressure change before and after injection.

As a consequence, the project starts from the delta-pressure Eq (2.17) along with the box method, to examine the relationship between the various parameters inside and to optimize the set of parameters that will result in the highest injection efficiency or the biggest storage capacity, finally use this as a foundation for analyzing the long-term variation in pressure.

At the beginning stage, the project's present focus is on the analysis of the relationships between the various parameters. Because pressure change dominates the final output in the delta-pressure approach, pressure is a major aspect in this project, in the box method, the pressure and the bulk volume are the only two variables in the Eq (2.18). The pressure is considered as the main part of the delta-pressure method as well. Then start with it to build up the connection,one can think of dV_b as corresponding to $V_{project}$ in the Eq (2.17) when assuming the compressibility is caused by the CO_2 injection completely. The $V_{project}$ is the CO_2 volume injection per day, so the dV_b is required to convert into the same unit by dividing by the entire injection period.

The parameters inside are always considered as the uncertainties, then the connection is established on parameters setting and several assumptions: the boxes are evenly-spaced, so all the property-related parameters are isotropic; a constant

injection pressure and injectivity; no-flow boundaries for the boxes; the depth of the box is relatively shallow, then the initial pressure can be estimated by the hydro-pressure. The value of other parameters can be determined by the real geological setting, so in this project, the deep-confined case is chosen as a major reference because of the geological environment of the Smeaheia.

As the major parameter illustrated in the reservoir pressure function (Eq. (2.16)), the characteristic scaling parameter A varies with the size of the boxes can be evaluated by this method. It can be calculated by the combination of function (Eq. (2.14)) and the pressure function (Eq. (2.16)), then it's calculated by the Eq. (3.1).The flux parameter F_b is assumed to be zero in this step when configuring the close boundaries for each box.

$$A = \frac{P_w - P_i - \frac{V_{project}}{I_c}}{\int_i^f p_D(t_D)} \tag{3.1}$$

3.2 Compartment Division and Scenarios

The study area we is modified from the structure map generated from Wu et al., 2021, the map is shown in the Fig A.1 in Appendix. On basis of the fault analysis in the Smeaheia area, this project divided the map into different compartments from the simplified fault extension in the study area(Fig A.2 in Appendix). Scenario B,C and D are built on each formation to compare the affect of different boundary conditions. Whereas the scenario B consists of 6 large compartments, C has 12 middle-size compartments and D has 24 small-size compartments, the hierarchy of scenarios is shown in Fig 3.2. Scenario B implies the highly communicated cases of all compartments, compare with the scenario D which is highly compartmented, scenario C is the in-between case. Fig 3.1 shows an example of the compartment division. The scenario B and C map are attached in the appendix.

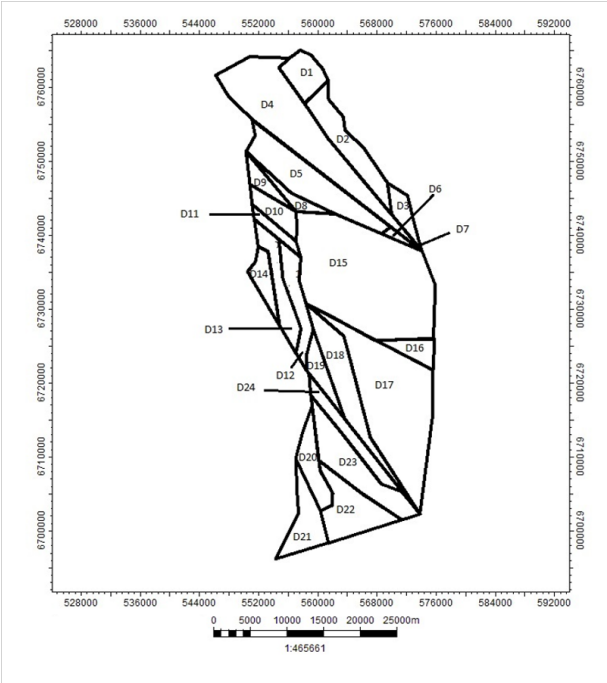

Figure 3.1: Scenario D compartment map

Hierarchy of Compartments																								
B1			B2				B3		B4					B5					B6						
C1		C2	C3	C4			C5	C6	C7	C8				C9		C10			C11		C12				
D1	D2	D3	D4	D5	D6	D7	D8	D9	D10	D11	D12	D13	D14	D15	D16	D17	D18	D19	D20	D21	D22	D23	D24	

Figure 3.2: Hierarchy of scenario B,C and D

3.3 Random sampling

To account for uncertainty in the input parameters, random sampling is applied in programming. Both uniform distribution and Gaussian (normal) distribution are used.

3.3.1 Uniform Distribution

The uniform distribution is simplified determined by boundaries a and b, which correspond to the maximum value and minimum value. The value interval can be either be open (e.g. (a,b)) or closed (e.g. [a,b]), so the distribution is abbreviated U(a,b), the U stands for uniform distribution. The difference between the maximum and minimum values defines the interval length, all intervals of the same length on the distribution should be equally probable. The maximum entropy probability distribution for random variable X under no constraint.

3.3.2 Gaussian Distribution

Gaussian distribution shows a continuous probability distribution for a real-valued random variable. The general form of the probability density function is defined by:

$$f(x) = \frac{1}{\sigma\sqrt{2\pi}} e^{-\frac{1}{2}(\frac{x-\mu}{\sigma})^2}$$

The parameter μ refers to the mean or expectation of the distribution, while the parameter σ refers to the standard deviation. The variance of the distribution is σ^2. A random variable with a Gaussian distribution means to be normally distributed, with a normal deviate(Weisstein, 2022). As Fig 3.3 shown:

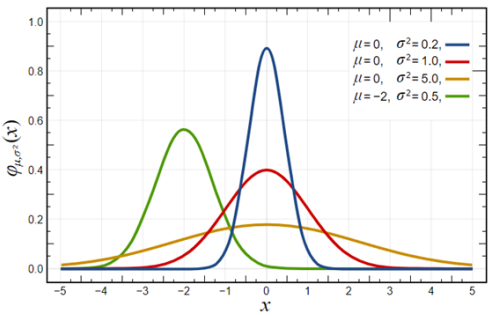

Figure 3.3: A selection of Normal Distribution Probability Density Functions. Both the mean μ, and variance σ^2 are varied('Normal Distribution PDF', 2022)

Gauss distribution are often applied to natural and social science analysis to represent real-valued random variable with unknown distribution. The importance of Gaussian distribution is partly because of the central limit theorem, it also has some unique properties in analytic studies, such as the normal deviate can be generated from any linear combination of fixed collection of normal deviates.

Many approaches and analysis, for instance the propagation of uncertainty and least squares parameter fitting, can be benefited from it since the analysis can be derived analytically in explicit form when the relevant variables are under Gaussian distribution(Weisstein, 2022).

3.4 Sensitivity analysis

There are several numerical and probabilistic tools targeted as determining the model of variables input which contribute to an interest quantity depending on model output mostly. This quantity can be the variance of the output variable.

Sensitivity analysis method are always used to study how the uncertainty in the output of a model can be apportioned to different sources of uncertainty in the model input. The most contributing and deterministic input variables can be figured out to an output behaviour as non-influential inputs involved(Iooss and Lemaître, 2015).

In this thesis, tornado diagrams are used for deterministic sensitivity analysis on the parameters to compare the relative importance of several parameters. The high, low, mean value of each variable is estimated from the previous study and the experiences of practical CCS project. The sensitive variables are centering by one modelled value and other variables are held at this set of baseline values. Then the sensitivity of each parameter can be showed by the diagram directly.

3.5 PCA

The numerous parameters involved in this project is considered as a difficult problem to solve, in order to handle the results and get a deeper understanding of the future work, multivariate analysis is required. Since the dataset used in this project is made of several examinations collected on a set of units, the rows are for units and variables are columns, then Principal Component Analysis (PCA) is firstly used to have an initial analysis of all parameters(Lewis-Beck et al., 2004).

The main goal of PCA is to decomposed data table, extract the most important information from the data tables, then compress the size of the dataset by keeping the important information, simplify the interpretation of the data and finally analyze the structure of the observations and the variables(Abdi and Williams, 2010). In the process, the new set of uncorrelated variables are defined as the principal components, and each unit is assigned a set of scores which corresponds to the projection on the components(Lewis-Beck et al., 2004). The PCA calculates the principal components by linear combinations of the original variables. The importance of each component is referenced by the variance of its projections or by the variance explained proportion. The first principal component is defined as having the largest possible variance. The second component is computed under the constraint of being orthogonal to the first component and to have the largest possible interia. These factor scores can be interpreted geometrically as the projections of the observations on the principal components(Abdi and Williams, 2010). In summary, the PCA approach is interpreted as an orthogonal decomposition of the variance of the dataset(Lewis-Beck et al., 2004).

Standardization of the data is the first step to standardize the range of the continuous initial variables so each variable contributes to the analysis equally. This is critical to perform this step to PCA since the latter is sensitive to the variance of the initial variables. When large differences between the ranges of initial variables exist, the larger range variable will dominate the whole process and lead to biased result. This result can be calculated by standard deviation of each value of each variable(Jaadi, 2021).

Generally, the second step is computed the covariance matrix. This is an important step to understanding the variance of each input and check if there is any potential relationship exist since some variables maybe highly correlated and informative, then the covariance matrix can be used to identify the correlations. If the matters in covariance is positive, then two variables are correlated, if the sign of the matters is negative, then the variables are inversely correlated(Jaadi, 2021).

For the third step the eigenvectors and eigenvalues are computed regarding the matrix to identify the principal components. These are the linear calculation to determine the principal components of the dataset. The principal components are constructed as linear combination of the initial variables which can be computed based on the correlation of the variables and the first component covers most of the information. This process is useful to reduce dimension without los-

ing too much information, this an be considered as new variable. So the principal components are less interpretable and don't have real meaning since they are computed as linear combinations of the initial variables. In other words, the principal components indicate the directions of the data which explain an maximum amount of variance. The principal components can be considered as new axes which provide best angle to evaluate the data, then the differences between the observations are observed further. The largest possible variance in the data set is the first principal component(Jaadi, 2021).

The fourth step is to decide the feature vector, computing the eigenvectors and order by their eigenvalues in descending order, the the principal components is decided by order of significance, then discard the less significance or keep all components, the remaining factors form a new matrix called feature vector, which has columns contain the eigenvectors of the keep components, the dimension gets reduction(Jaadi, 2021).

The final step is to recast the data along the principal components axes, use the feature vector formed using the eigenvectors of the covariance matrix to reorient the data from original aces to the principal components, which can be the production of transpose of the original dataset and the transpose of the feature vector(Jaadi, 2021).

3.6 Data

For the initial estimation and basic analysis of the parameters and modelling, the data is mainly from the database of the article from Ringrose, 2020. To build the scenarios and divide compartments on basis of the fault systems, we used Petrel 2021 to process the data and make the polygon of the study area on basis of the Equinor 2019 simulation grid. The horizons and faults information is from Smeaheia dataset from the CO_2 Datashare, the depths and thickness information was converted by Center for Geophysical Forecasting(CGF), an example of the fault map is shown as FigA.2 in Appendix. Well logging data (NPD, 2000,NPD, 1985) from the target area (especially the Well 32/2-1 and the well 32/4-1 T2) are used to determine geological parameters, such as porosity, net to gross ratio and permeability.

Finally, the data from the Sleipner and the Snøhvit project are also utilized in this project as a reference to set some injection factors and examine the variance of pressure levels in respect to the parameters.

3.6.1 CO_2 Density

The CO_2 density is determined base on the NIST online database, the density can be simply considered to correlate with the pressure and formation temperature, which can be converted to a function of depth in further. The geothermal gradient is set as 35 ^oC/km on basis of the previous study (Ringrose and Meckel, 2019) and then the CO_2 density changes with depth in different formations is shown as Fig 3.4. The result is affected by temperature and depth in both, the Krossfjord formation has a little lower density than the Fensfjord formation, while density in the Sognefjord formation is much higher than others.

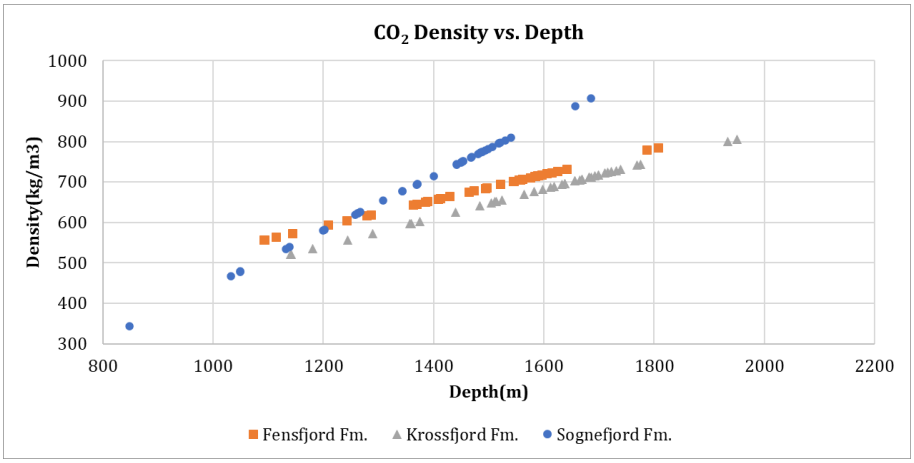

Figure 3.4: Density of CO_2 versus depth in three formations

3.6.2 Porosity

On basis of the previous work, the porosity in the project was set as 0.3 for three formations. While to figure out the effect of different parameters, a more accurate and reasonable range of porosity is needed. According to the previous study and well logging report of the Viking Group, the porosity range for each formation is determined as the table3.1 shown:

	low	mean	high
Sognefjord Formation	27%	30%	34%
Fensfjord Formation	26%	27%	28%
Krossfjord Formation	21%	23%	25%

Table 3.1: Porosity of different formations

3.6.3 Injectivity

The initial injectivity value was set to 40 m^3/day/bar based on the assumption of a deep confined case. When aiming to obtain a more scientific analysis of the entire project, the injectivity value can be determined based on both the Sleipner project and Smeaheia modeling(Brobakken, 2018). Regarding the geological study in Smeaheia area, the injectivity of Sognefjord formation is close to Sleipner project, and the Krossfjord formation's injectivity is much lower caused by the low permeability. Then the I_c value is set at 1000, 500 and 50 ton/day/bar for Sognefjord, Fensfjord and Krossfjord Formation respectively.

	Injection rate (t/d/bar)	CO_2 density (kg/m^3)	I_c (m^3/d/bar)
Sognefjord Fm.	1000	697	1500
Fensfjord Fm.	500	677	725
Krossfjord Fm.	50	675	75

Table 3.2: Injection rate and injectivity used in final result

3.7 The workflow

Based on the previous study done in the project report, a more accurate compartment division on the published map of Smeaheia area is used as the foundation. Some simple relationships between parameters have been obtained from previous work, based on this, the initial estimation of parameters setting is determined. The programs are coded up in Python scripts(cooperate with Eline Nybråten) for the pressure function (Eq 2.16) and volume limit function (Eq 2.18) to calculate the pressure and injected CO_2 based on the initial parameter estimates. Then use this as a basis to change the parameters as different inputs by random sampling to obtain the new results for pressure and CO_2 injected over different time period as output. Compare the results from different input settings by numerical analysis approaches, calling the "sklearn" package to perform Principal Component Analysis(PCA) of the results via Python scripts (Appendix4.4), attempt to figure out the deterministic parameter and optimize the injection.

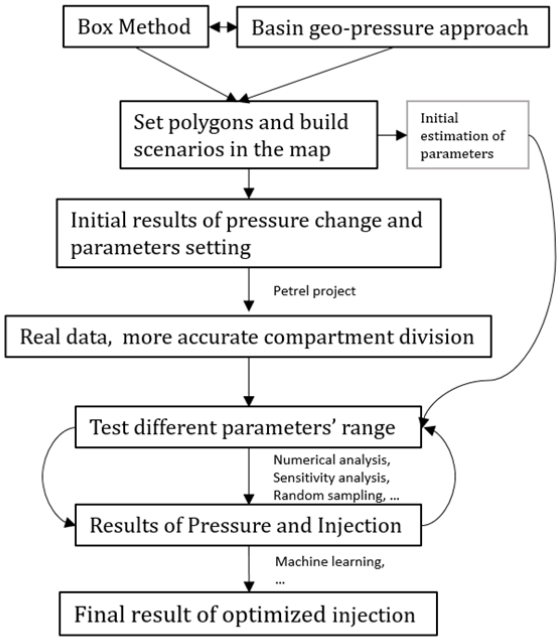

Figure 3.5: Workflow of the project

Chapter 4

Results

At the beginning of the project, all parameters were set to fixed values to have a more direct and simple view of the injection results in all compartments. While to complete the numerical analysis as well as the injection-related calculation, a more accurate and scientific parameter setting was required. So the first step was to study the parameters and observe if there could be any potential relationship between each parameter.

By observation of Eq 2.18, scaling parameter A appears to have a significant influence on the results of injection as it is involved in the integration of pressure variation with time, so the first step was set to explore the scaling parameter A.

4.1 Scaling Parameter A

For the estimation of each parameter, the initial values of each parameter are set based on the dataset from previous work. Regarding the function applied to calculate the injected CO_2 volume, the main parameters in the pressure function include the scaling parameter A and injectivity I_c. Combining Eq 2.17 and Eq 2.18, assuming an injection period of 25 years, then replacing dV_b with the product of $V_{project}$ and time, one obtains the scaling parameter A is related to the geometry and the compressibility of the box. To test how A changes with area size (volume), some initial parameters are required to simulate the value.

4.1.1 Geometric factor

From the previous dataset(Ringrose and Meckel, 2019), the deep-confined case from the basin fluid delta-pressure approach is applied in terms of the geological setting of the Smeaheia area, then as the first step, all the parameters used in the calculation is derived from this setting. I_c is assuming equal to 40 m^3/day/bar, the initial pressure of the formation is equal to 290 bar as P_i and assume when the injection is completed, the pressure is equal to 391 bar as P_f. For the dimensionless pressure calculated, the coefficient is 0.5 caused by the reservoir boundary conditions, γ=1.781 is related to Euler's constant.

The images of estimating the scaling parameter A variation with area size and volume are generated under these assumptions, it illustrates that the A value is decreasing when the area is getting larger, the images of the variation of A with the size of area as well as pore volume are obtained(as Fig4.2 and 4.1 shown).

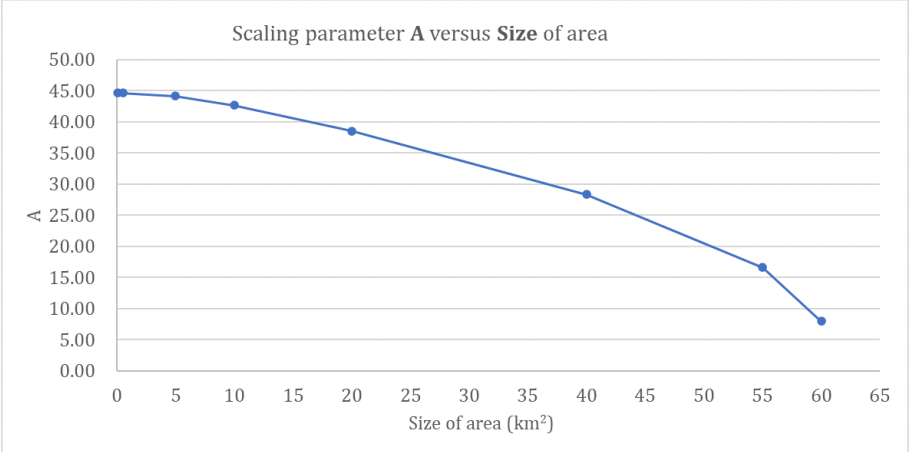

Figure 4.1: A varies with area size

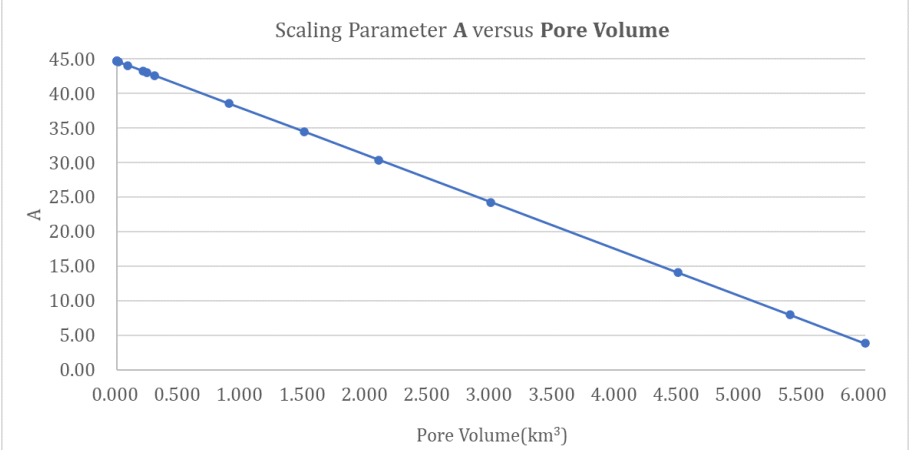

Figure 4.2: A varies with pore volume

4.1.2 Compressibility

To have an initial estimation on the compressibility affect, the simple range of C_b is chosen as $10^{-9} \sim 5 * 10^{-9} \text{Pa}^{-1}$, maintain other parameters' value, then the A changes with area size and pore volume in different compressibility are shown as Fig 4.3 and 4.4.

To obtain a more complete view, a Python script is designed to sample the area size and volume uniformly at random, run over two different C_b ranges ($10^{-11} \sim$

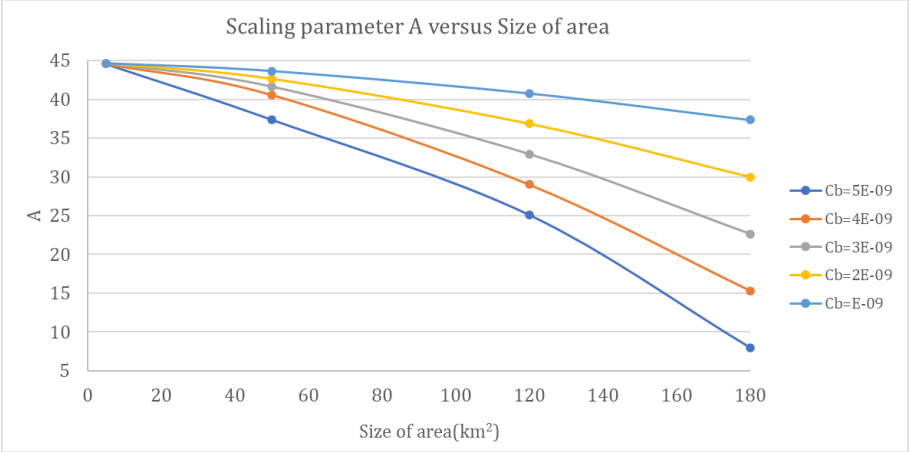

Figure 4.3: Scaling parameter A versus size for different compressibility

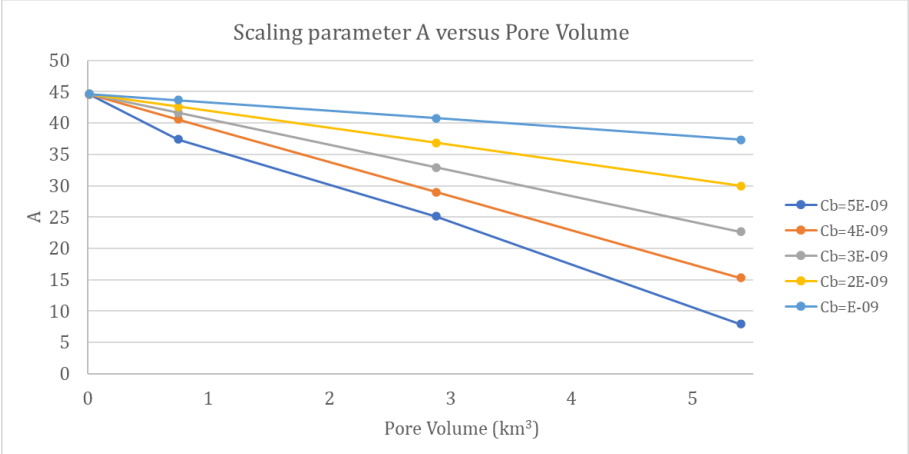

Figure 4.4: Scaling parameter A versus pore volume for different compressibility

$5 * 10^{-9}\text{Pa}^{-1}$ and $3 * 10^{-10} \sim 7 * 10^{-9}\text{Pa}^{-1}$), then generate scatter plots as shown in Fig 4.5.

Fig 4.5 shows the value of A is more concentrated in the case of a smaller size(volume) and decreases gradually with the larger ones. The relatively wider range of compressibility makes the data points concentrated at the much higher slope.

To have a more random distribution of the A points, the compressibility is randomly selected from the range of $10^{-11} \sim 10^{-9}$. The actural size and thickness of each compartment is enterd into the equation, and the C_b is chosen randomly using Python scripts, the results of the variation of A with size and volume is shown in Fig 4.6(the code is in Appendix4.2).

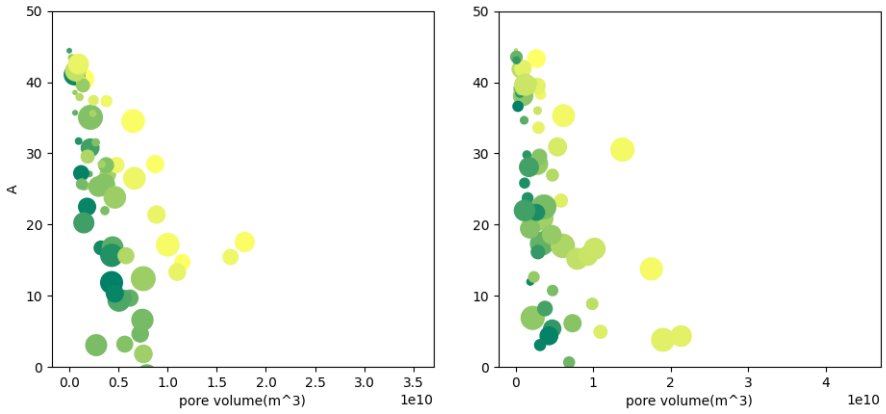

Figure 4.5: Different compressibility ranges set for A versus pore volume plots. The point size corresponds to the area size for each compartment, the color from light yellow to green shows the increasing compressibility. (left): $C_b = 10^{-11} \sim 5 * 10^{-9} \text{Pa}^{-1}$, (right):$C_b = 3 * 10^{-10} \sim 7 * 10^{-9} \text{Pa}^{-1}$.

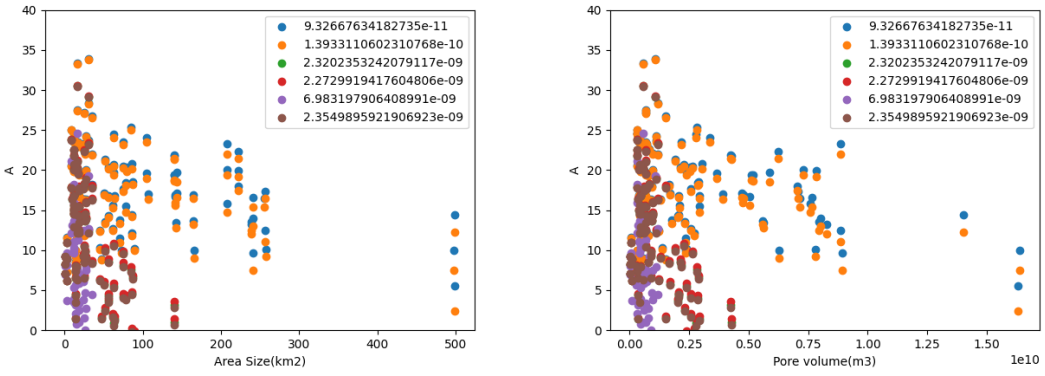

(a) A versus Area size **(b)** A versus Volume

Figure 4.6: A distribution with random sampling compressibility

4.2 Injection Constraint

4.2.1 Maximum Volume limit

The box approach provides the maximum volume of injected CO_2, as the Eq (2.18). The volume constraint for each compartment can be calculated from compressibility, pore volume of the formation and the pressure change. The limit can be calculated from Eq 4.1):

$$dV_b = C_b * V_b * dP \tag{4.1}$$

The compressibility to calculate the maximum volume is selected as $7 * 10^{-9} \sim 10^{-9}\text{Pa}^{-1}$ while the delta pressure can be set as 3 MPa based on other previous projects. It is found that when assuming compressibility is a constant and small injection rate, only in very small compartments from scenario D the maximum volume can be reached, such as the D6 and D7, then the injection volume is equal to the maximum pore volume change. In the large compartments such as B5 in three formations, the volume limits can not be reached when the injection rate is low. This simplified box limit method is only intended as a way of assessing injection volume limits.

4.2.2 Maximum Pressure Limit

After several attempts, compressibility is verified as the second-important factor to determine the capacity, while the pressure limit is the key issue in this project. From Eq 2.16, when the CO_2 continues to inject into the reservoir, the pressure inside the storage unit is increasing, and the fracture pressure of the formation is vital to determine the stop timing of injection. Furthermore, the scaling parameter A also affects the change rate of pressure. The maximum pressure limit is estimated as 90% of the fracture pressure (Eq 2.7), the parameters involved are based on previous study of North Sea(Ringrose and Meckel, 2019), the items in this equation are calculated as follow:

- ρ_{brine} = 1020 kg/m^3 + 60 kg/km * Depth (km)
- ρ_{bulk} = 2000 kg/m^3+150 kg/km * Depth(km)
- Poisson ratio: υ = 0.1 + 0.06 * Depth (km)
- P is assuming equals to P_{hydro}, determined by ρ_{brine} and depth.
- σ_V, as shown in Eq 2.9, determined by ρ_{bulk},ρ_{brine} and the seafloor depth, which is set as 0.35 km.

The calculation results are shown as Fig 4.7:

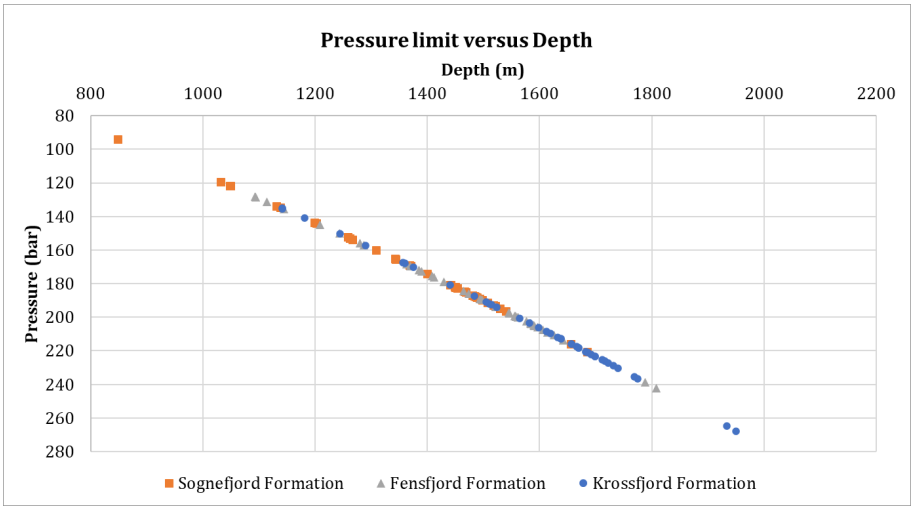

Figure 4.7: Maximum pressure limit versus depth in three formations

4.3 Pressure variation

In this section, the pressure variation with time is the main point to discuss. Based on the function in Eq. 2.16 , the pressure increases at the beginning, and when it reaches the pressure limit, the injection stops, and then pressure starts to decrease, until it returns to the initial pressure(hydrostatic pressure). For most of the compartments, the pressures can reach the peak value due to the pressure constraint after tens of years. While for the huge compartment from scenario B, the pressure increases very slowly, so both the pressure and mechanical constraints cannot affect the injection period in this case.

From the formula for the injection volume (Eq. 2.16), the decay function following injection stop is assumed to be the inverse of the pressure increasing function, so the equation is set as:

$$P_{res}(t) = P_i - AP_D(t_D) \tag{4.2}$$

In this study, the initial pressure is estimated from the hydrostatic pressure, which is determined by the compartment depth, seafloor depth and the brine density. A is estimated from the previous study result, combined compressibility and size area. The pressure limit is estimated on basis of fracture pressure, calculated from the vertical stress and Poisson ratio, generally determined by the depth, seafloor depth, brine density and bulk density as discussed in Section 4.2.2.

As the function of pressure shown, the pressure changes with time and limited by fracture pressure and initial pressure. A python script is designed on basis of Eq 4.2 and 4.1, where each parameter is referenced to the analysis in Section 4.1.2, C_b is set equal to 3.0E-09 Pa^{-1}, take in account of scaling parameter A, the average porosity of each formation is selected from Section 3.6.2, and other parameters are the same as those used in the deep-confined case from paper(Ringrose and Meckel, 2019). Assuming a maximum project life of 50 years, the results show in most of the compartments the pressure decreases rapidly after injection is stopped, while for some very large compartments, the pressure keeps increasing, the pressure cannot stop because of the slowly rising rate. As Fig 4.8 shown, the pressure reaches the limit in 37.5 years and the injection stops, then pressure decreases, while in the extremely big compartment B5 as shown in Fig 4.9, the pressure increases slowly and does not reach the pressure limit during the project period. In a very small compartment, the pressure increases very quickly and reaches the limit in a short period, such as D5 compartment (Fig 4.11) , compared to the result of C9 compartment (Fig 4.10) the rate of variation is much higher. The program used to generate the pressure function is attached in the Appendix4.1.

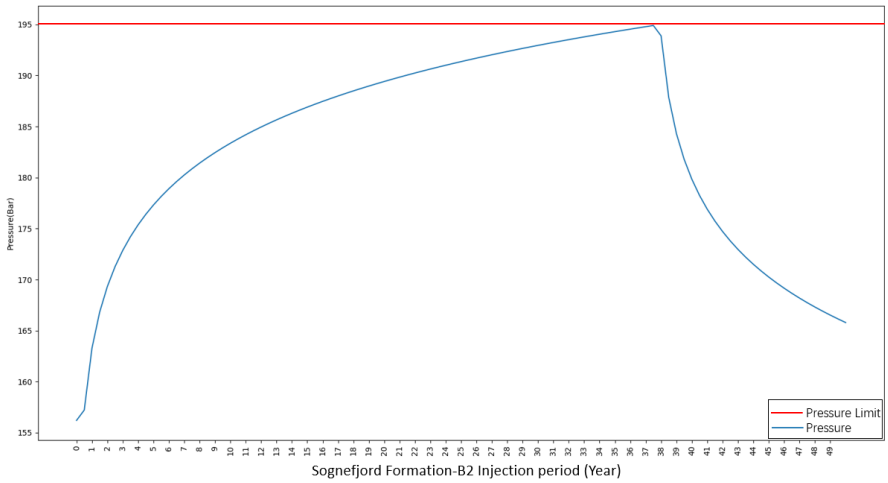

Figure 4.8: Pressure curve in B2 compartment of Sognefjord Fm.

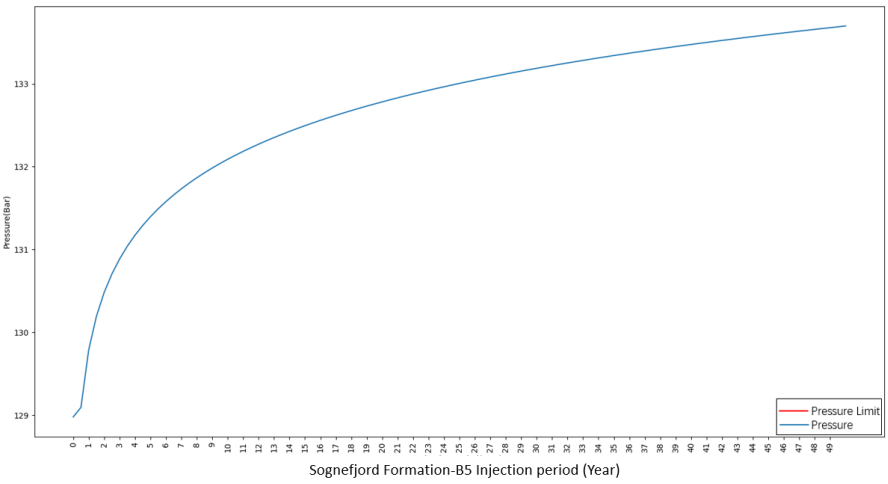

Figure 4.9: Pressure curve in B5 compartment of Sognefjord Fm.

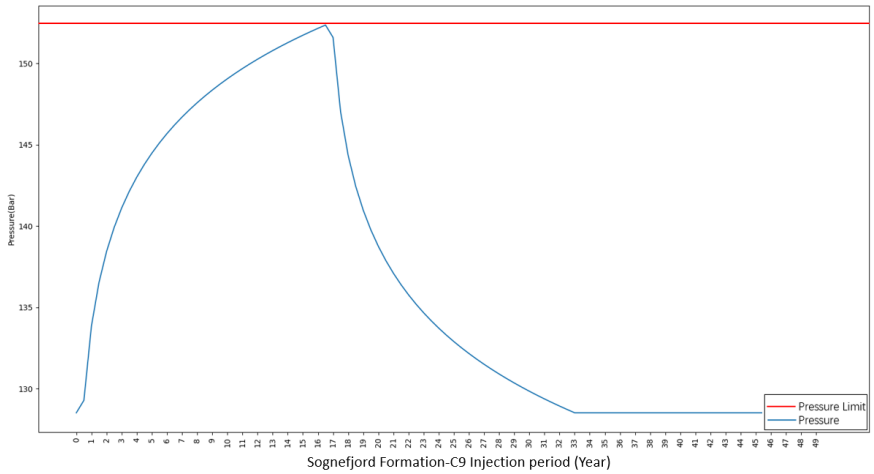

Figure 4.10: Pressure curve in C9 compartment of Sognefjord Fm.

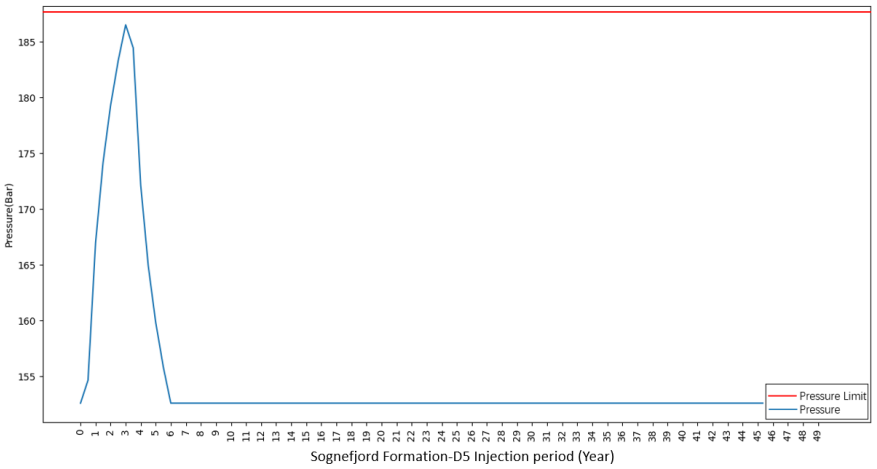

Figure 4.11: Pressure curve in D5 compartment of Sognefjord Fm.

4.4 Injection Volume Estimation of Different Scenarios

From Eq 2.17 the final injection volume can be calculated. Scenario B, C and D have different numbers of compartments and therefore different connectivity, decreasing from B to D scenario. Since B scenario is set to the case where connectivity is best, the assumption was scenario B can store the most. However, the calculations show that the results are uncertain due to the different conditions in each compartments, as Fig 4.12,4.13 and 4.14 shown. The entire dataset is attached in the Appendix A.3.

Sognefjord Fm.	Ic = 1000 t/d/bar							por=0.3	
	B1			B2				B3	
Total injected volume of scenario B(m3)	**1.82E+07**			**1.12E+08**				**1.25E+07**	
	C1		C2	C3	C4			C5	C6
	1.66E+07		5.59E+06	7.11E+07	3.91E+07			5.88E+06	6.24E+06
Total injected volume of scenario C(m3)	**2.22E+07**			**1.10E+08**				**1.21E+07**	
	D1	D2	D3	D4	D5	D6	D7	D8	D9
	1.23E+07	1.25E+07	5.59E+06	7.11E+07	3.74E+07	1.37E+06	1.26E+05	5.88E+06	6.24E+06
Total injected volume of scenario D(m3)	**3.05E+07**			**1.10E+08**				**1.21E+07**	

Figure 4.12: Some examples for injection volume(m3) in Sognefjord formation

Fensfjord Fm.	Ic = 500 t/d/bar							por=0.27	
	B1			B2				B3	
Total injected volume of scenario B(m3)	**1.18E+07**			**1.20E+08**				**1.41E+07**	
	C1		C2	C3	C4			C5	C6
	1.06E+07		4.80E+06	7.59E+07	2.74E+07			6.67E+06	7.01E+06
Total injected volume of scenario C(m3)	**1.54E+07**			**1.03E+08**				**1.37E+07**	
	D1	D2	D3	D4	D5	D6	D7	D8	D9
	1.13E+07	7.68E+06	4.80E+06	7.59E+07	3.35E+07	1.32E+06	1.27E+05	6.67E+06	7.01E+06
Total injected volume of scenario D(m3)	**2.37E+07**			**1.11E+08**				**1.37E+07**	

Figure 4.13: Some examples for injection volume(m3) in Fensfjord formation

Krossfjord Fm.	Ic = 50 t/d/bar							por=0.23	
	B1			B2				B3	
Total injected volume of scenario B(m3)	**1.69E+06**			**6.27E+07**				**3.01E+06**	
	C1		C2	C3	C4			C5	C6
	1.42E+06		6.54E+05	3.01E+03	3.88E+06			3.08E+06	2.97E+06
Total injected volume of scenario C(m3)	**2.07E+06**			**3.89E+06**				**6.05E+06**	
	D1	D2	D3	D4	D5	D6	D7	D8	D9
	1.50E+06	1.01E+06	6.54E+05	2.13E+07	5.29E+06	7.90E+05	99482,9	3.08E+06	2.97E+06
Total injected volume of scenario D(m3)	**3.16E+06**			**27453133,66**				**6.05E+06**	

Figure 4.14: Some examples for injection volume(m3) in Krossfjord formation

For instance, compare different scenarios, from the scenario map (Fig A.3,A.4 and Fig 3.1), B1 compartment is divided into C1 and C2 compartments, where C1 is then divided to D1 and D2 compartments. In Krossfjord Formation (Fig 4.14), B1 can store 1.69E+06 m^3 CO_2 in 50 years, when it is divided into C1 and C2,

the sum of injections in these two compartments is 2.07E+06 m^3, greater than B1. When C1 is divided into D1 and D2, the sum of scenario D is 3.16E+06 m^3, greater than both B and C. For B2 compartment, it is divided into C3 and C4, these two compartments are divided into D4, D5, D6 and D7. In Krossfjord Formation, the sum of injected CO_2 of scenario D is 2.75E+07 m^3, greater than the sum of C3 and C4 for 3.88E+09 m^3, while is less than the result of B2, 6.27E+07 m^3. B3 compartment is divided into small compartments C5 and C6, same as compartments in scenario D. The total injected volume of B3 compartment is 3.01E+06 m^3, less than the sum of C5 and C6 (D8 and D9).

Compare the injection results for the same compartment in three formations, such as the result for compartment B1 in Sognefjord Formation is 1.82E+07 m^3, which is greater than the result in Fensfjord Formation of 1.18E+07 m^3 and the result in Krossfjord Formation of 1.69E+06 m^3. However, for B2 compartment, the result of Sognefjord Formation is 1.12E+08 m^3, which is less than 1.20E+08 m^3 for Fensfjord Formation but greater than 6.27E+07 m^3 for Krossfjord Formation. Thus, injection results for the same compartment in different formations may also vary depending on the situation.

4.5 Sensitivity analysis

As the preliminary work of sensitivity analysis, several random sampling tests were applied to test for different parameters' affect. All parameters are set as fixed values to give a reference, the results are shown in Fig 4.15 and 4.16. Log the result indicates the linear-like relationship of datapoints.In this case The porosity is set as 0.3,0.27 and 0.23 for Sognefjord Fm, Fensfjord Fm. and Krossfjord Fm. respectively. To simplify the problem, for this initial estimation, the injection is set as 40 m3/day/bar, the compressibility is set equal to 3.0E-09 Pa^{-1}.

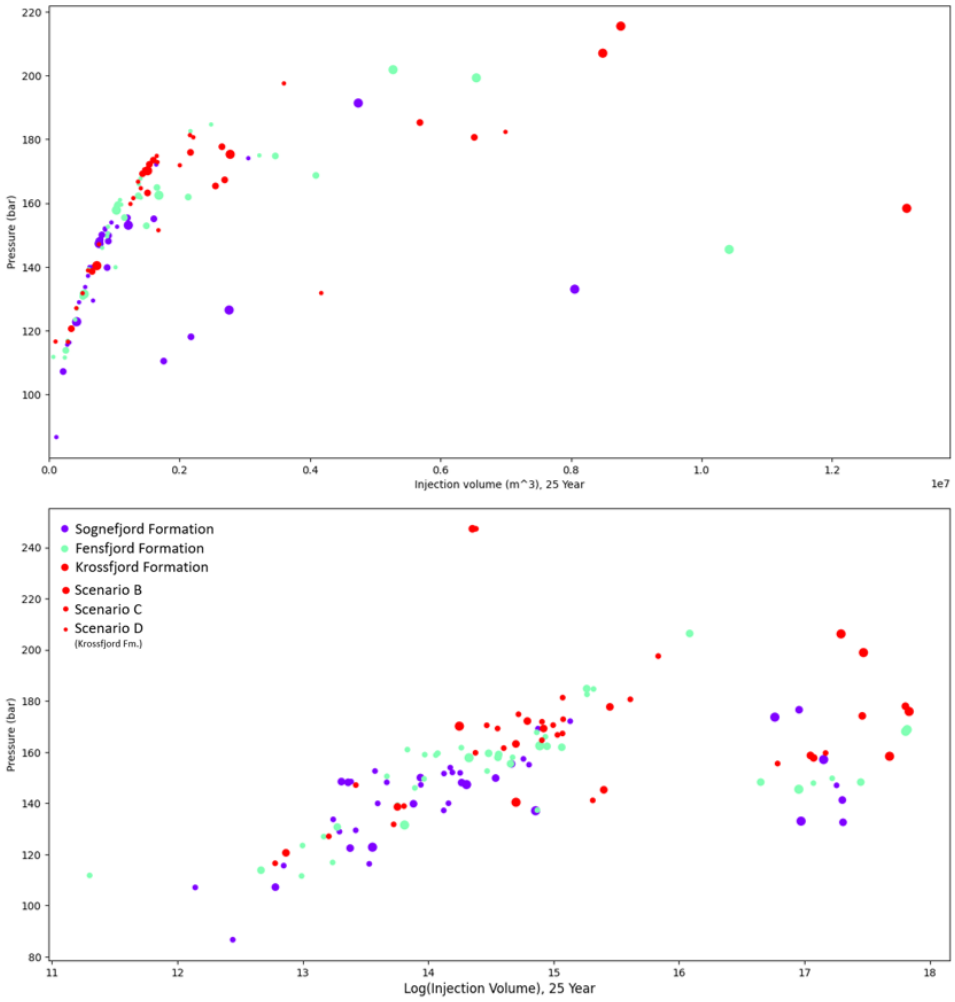

Figure 4.15: Injection volume versus pressure in year 25

To obtain more types of data distribution, the values of parameters were selected randomly from the corresponding value intervals. As the first attempt, combined with the geological data, the Gaussian distribution was applied to randomly sample the porosity. The mean porosity value was set as 0.3 and the standard de-

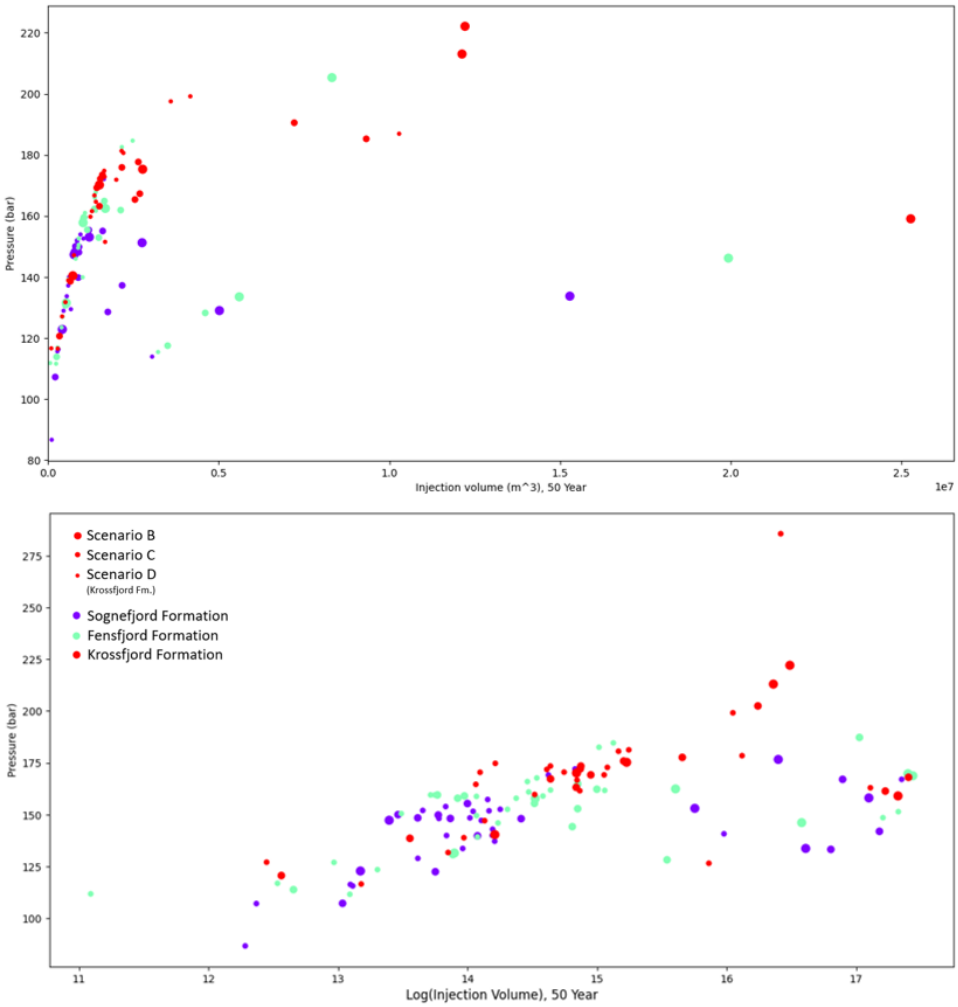

Figure 4.16: Injection volume versus pressure in year 50

viation was set as 0.05 when other parameters were set as fixed values, the results didn't show difference. So uniform distribution was then applied to all parameters in the randomly sampling. To have a rough and direct estimation, the main parameters ranges were set as follow:

- porosity: 27% $\sim$ 34% for Sognefjord Fm., 25% $\sim$ 29% for Fensfjord Fm., 21% $\sim$ 25% for Krossfjord Fm.
- Injectivity: 30 $\sim$ 60m^3/day/bar
- Compressibility: $1.0E-09 \sim 7.0E-09\text{Pa}^{-1}$

The similar data trend in the plots shows three data clusters inside, compared to the constant parameter plot in year 25 (Fig4.15), the findings of the effects of compressibility and injectivity are clearly shown. When taking random samples of the compressibility (Fig 4.17b), the result tends to disperse much more. The ran-

dom change of injectivity disperses a large set of data points that were originally clustered together in the middle(Fig 4.17c).

To analyse the problem of parameter setting, the sensitivity analysis is introduced to have a more scientific perspective of the entire setting. For the initial estimation, the tornado plots are selected since which can provide a summary of how different parameters affect the result. According to the analysis on parameters before and the result from previous work, the main parameters we put into the tornado charts include compressibility, porosity, injectivity, delta pressure(controlled by different practical well conditions), pressures(caused by the uncertainty of depth). On basis of the density analysis in Section 3.6.1, the injected volume can be converted to mass of injected CO_2, since the mass-scale is more convenient to compare with the published data of other real projects. Then the parameters lead to the change of the injection in different compartments per year. The test ranges of different parameters are shown in the table 4.1:

Formation		I_c	C_b	P_i(bar)	P_m(bar)	dP(MPa)	porosity
Sognefjord Formation	mean	1500	5.00E-09	-	-	3	0.3
	low	1250	7.00E-09	-10	85%P_f	5	0.34
	high	1750	1.00E-09	+10	95%P_f	1	0.27
Fensfjord Formation	mean	1000	5.00E-09	-	-	3	0.27
	low	725	7.00E-09	-10	85%P_f	5	0.26
	high	450	1.00E-09	+10	95%P_f	1	0.28
Krossfjord Formation	mean	75	5.00E-09	-	-	3	0.23
	low	50	7.00E-09	-10	85%P_f	5	0.21
	high	100	1.00E-09	+10	95%P_f	1	0.25

Table 4.1: Setting of parameter value used in tornado plot

- I_c: Injectivity (m3/day/bar)
- C_b : Compressibility (Pa^{-1})
- P_f : Fracture pressure (bara)
- P_i : Initial pressure
- P_m : Maximum pressure limit
- dP : Delta Pressure (MPa)

There are some examples show the same area in different formations can be affected by different factors. The results are all obtained from the year 50, the injection in all compartments has already stopped. B3 compartment has a relatively large area size compared to others, so the assumption was both the pressure and compressibility constraints might be difficult to reach in this case. While as the Fig 4.18 and 4.19 shown, the C_b, dP and porosity control the injection result, it indicates that although the capacity is quite big in B3 compartment, it can still be reached due to the high injectivity, which leads to a quick injection and a short injection period. Then the injected volume is limited by the maximum storage capacity. The pressure change, compressibility and the porosity can affect

the injection results and the total mass of injected CO_2 is in the range of around 3∼15 Mt. However, in the Krossfjord formation (Fig 4.20), the injectivity is assuming to a low value, the result shows the maximum pressure, initial pressure, I_c and C_b control the injection, it implies a result of pressure domain, all these parameters change leads to the change in geo-pressure function, thus the pressure limit changes and then affect the final result. The maximum pressure limit and the initial pressure has a significant effect on the result, the injectivity and the compressibility also affect the results, and the total mass of injected CO_2 is between 1∼4 Mt.

The tornado plots for same formation with low injectivity, such as compartments in Krossfjord Formation (Fig 4.20,4.21 and 4.22), the results show that several pressure-related parameters domain the injection process, the pressure bounds are essential in these compartments, so the pressure limits controls the injection process. The mass of injection CO_2 varies from $1 \sim 3.6$ Mt in the B3 compartment, $1 \sim 3.4$ Mt in C7 compartment and $1 \sim 3.1$ Mt in D11 compartment.

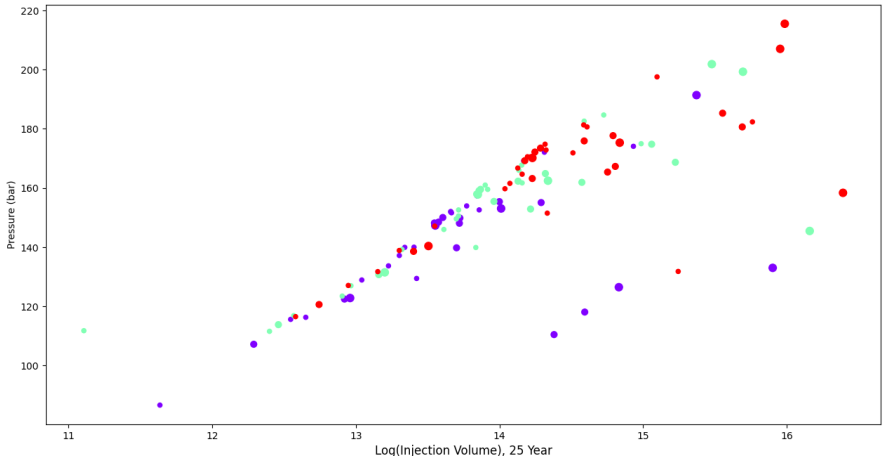

(a) Result of randomly selecting porosity in year 25

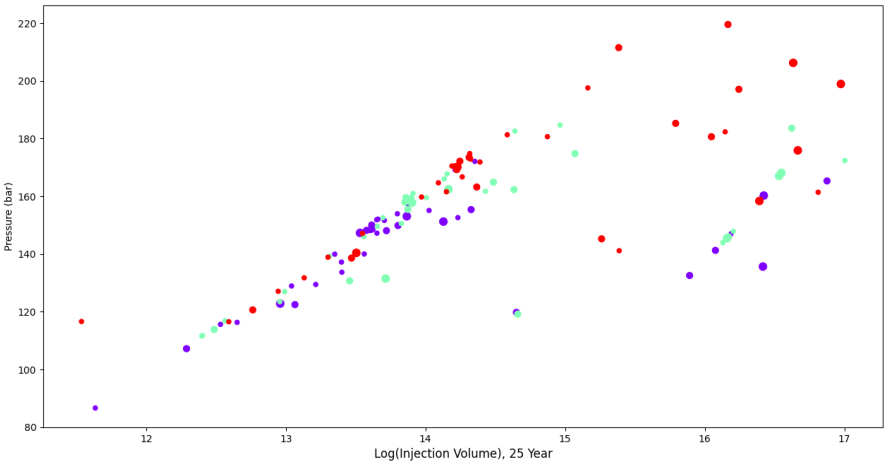

(b) Result of randomly selecting compressibility in year 25

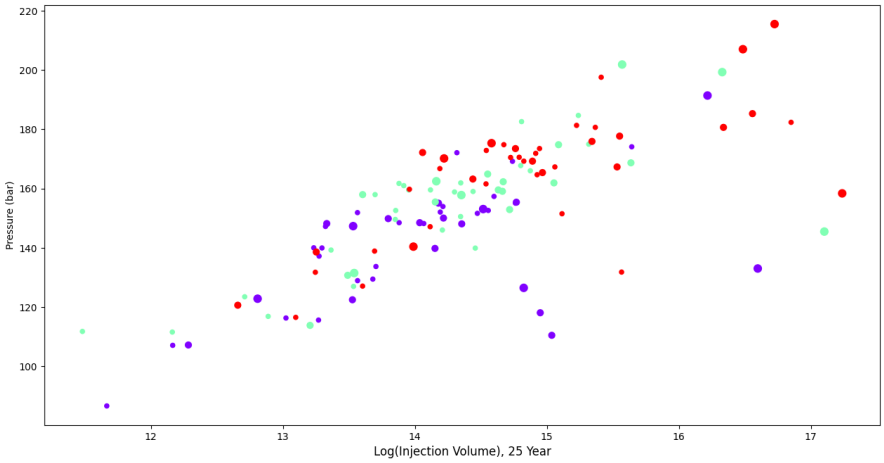

(c) Result of randomly selecting injectivity in year 25

Figure 4.17: Examples for the results of random sampling parameters in year 25

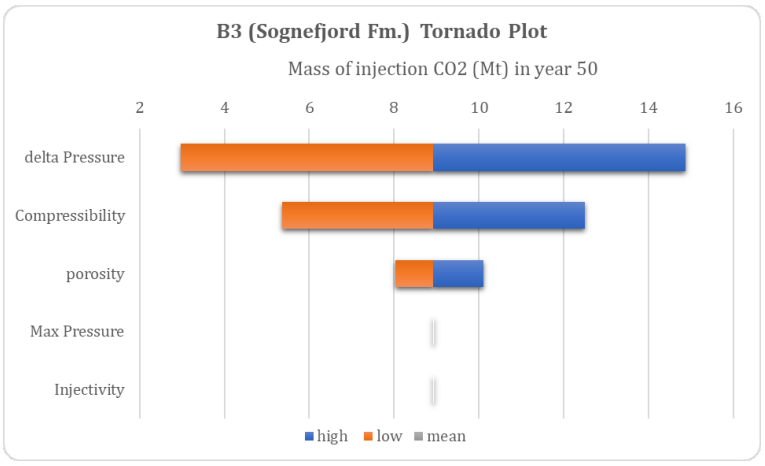

Figure 4.18: Tornado plot for B3 compartment in Sognefjord Formation

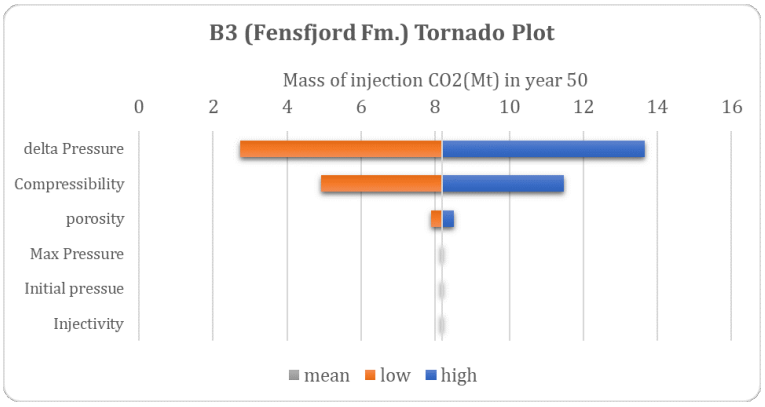

Figure 4.19: Tornado plot for B3 compartment in Fensfjord Formation

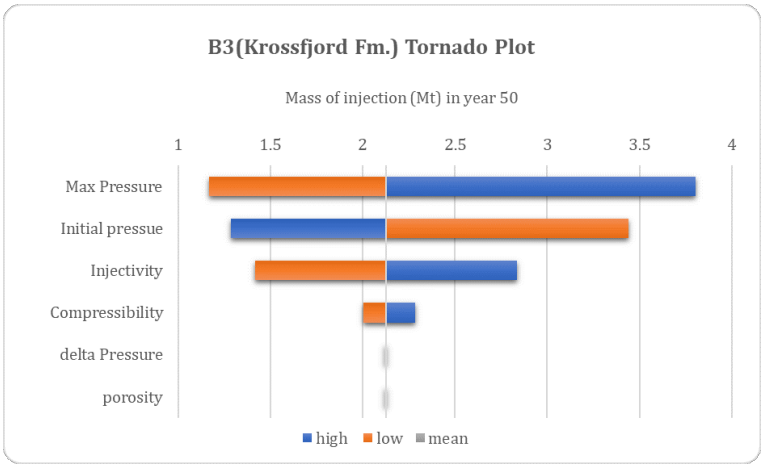

Figure 4.20: Tornado plot for B3 compartment in Krossfjord Formation

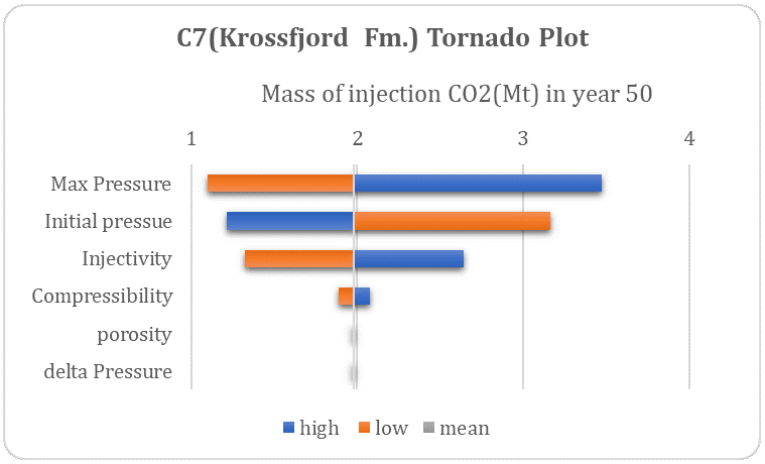

Figure 4.21: Tornado plot for C7 compartment in Krossfjord Formation

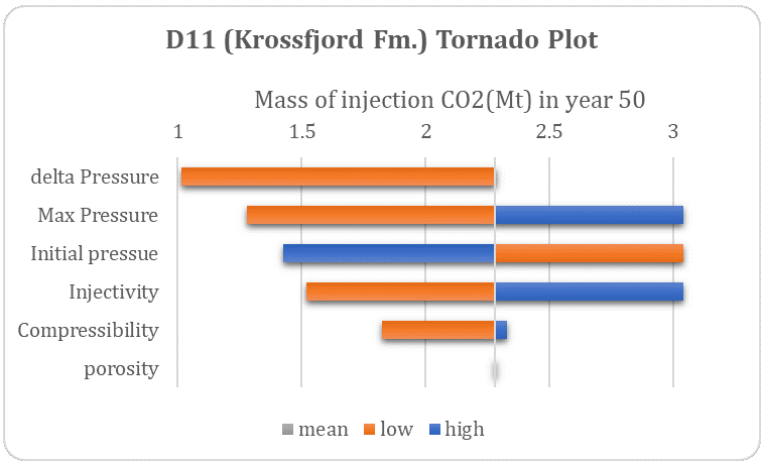

Figure 4.22: Tornado plot for D11 compartment in Krossfjord Formation

4.6 Mass of Injection CO_2

As discussed in Section 4.5, the volume of CO_2 injected is converted to the mass of CO_2 injected in order to assess the injection results more directly and to facilitate comparison with publicly available data from other successful CCS projects. Compared to the data from practical CCS projects, the mass of total injection does not always reach the expected value. This unsatisfactory result is controlled by a complex parameters set. Based on the results obtained from tornado plots as well as the real project data, it was found that the injectivity could always play a significant role and domain the final result, in further, the compressibility also affects the process since it relates to the scaling parameter A which controls how fast the pressure changes. To examine and obtain a reasonable value for this project, the injectivity was set in the range of $60 \sim 2000 \mathrm{m}^3/\mathrm{day/bar}$ and compressibility was set to 5.0E-09 a bit higher than before, then the results shown as Fig 4.23 and 4.24.

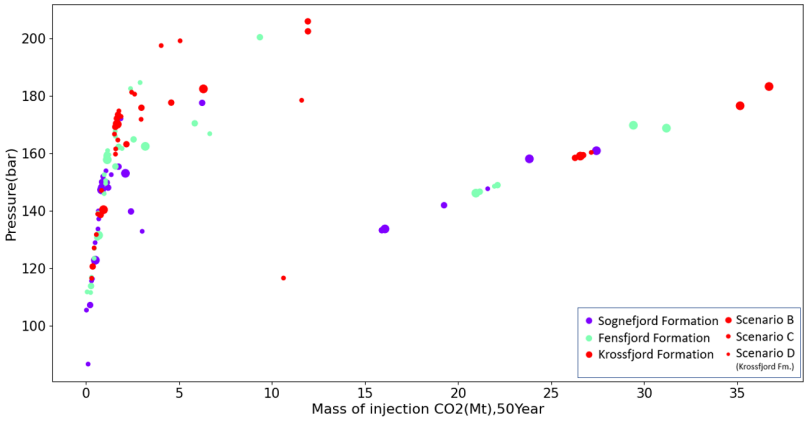

Figure 4.23: Injection result in 50 year $C_b = 5.0E-09\mathrm{Pa}^{-1}, I_c = 60\mathrm{m}^3/\mathrm{day/bar}$

The result shows a cluster and a linear-like relationship. The small compartments points gathering in low value caused by the pressure constraints are reached in these compartments. The linear-like relationship in the big compartments appears to the right of the plot, which may cause by the scaling parameter A being equal to 2 (this value is set as the lower bound of A) in all big compartments, the results are controlled by injectivity value and the biggest mass of injection CO_2 is around 35 Mt in this case.

As the injectivity is extremely high in this case, the irregular distribution of results can result in the volume limits being reached in most of the cases. A comparison with findings of pressure limits shows that although in most of the cases, the pressure in the compartment reaches the limit before volume reaches the limit, when the injectivity changes to a very high level, even some big compartments can reach the volume limit in tens years before the pressure increases to the peak

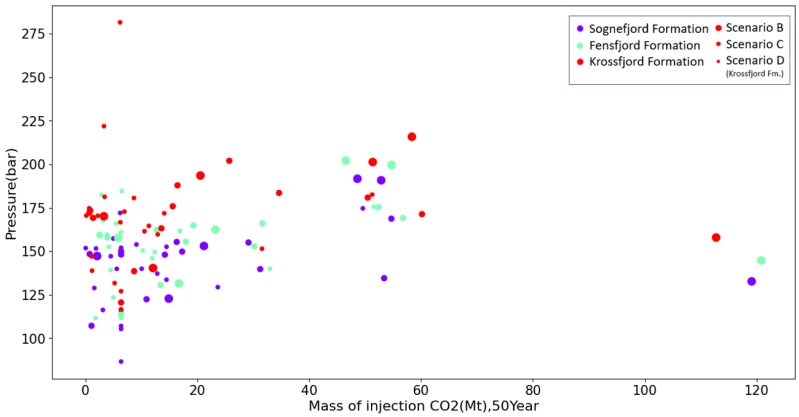

Figure 4.24: Injection result in 50 year $C_b = 3.0E-09\text{Pa}^{-1}$, $I_c = 2000\text{m}^3/\text{day/bar}$

value, so the injection volume changes further.

On basis of the practical data from Sleipner and Snøhvit CCS projects, the injection parameters are set as the table 3.2 shown. Fig 4.25 and 4.26 show the mass of injection CO_2 in year 25 and 50.

Compare the result plots of different project times, it clearly shows that the injection in all the compartments of Sognefjord formation has already stopped limited by the volume constraint, even in the biggest compartment the injection stops before year 25 and then pressure drops down back to the initial pressure, while in the Fensfjord formation, only the biggest compartment has mass increasing between year 25 and 50. In the Krossfjord formation, most of the compartments affected by the pressure limit and injection stopped in an early time period, and pressure decay between years 25 and 50 without the mass of injection change. The compartments in Krossfjord Formation have the largest variation of pressure, compare two plots of different times, to the left of the images, the injected volume in small and middle-size compartments doesn't change, only pressure in some compartments decreases in this period, which indicates that the injection in most of the Krossfjord formation compartments has already stopped before the year 25, the time varies lead to the pressure drop down back towards the initial pressure. While there are some big compartments from scenario D that have increments in pressure and injected volume, which means that the injection continues in these compartments since neither pressure nor compressibility limits are reached. The maximum mass of injection CO_2 is around 50 Mt, other values are gathering below 20 Mt.

The points of Fensfjord Formation compartments are distributed in the middle range of the entire results. From the comparison of the two plots, almost all of the compartments in Fensfjord Formation don't move in this period, so the injection in most of the cases has already stopped before year 25, pressures in some compartments decrease and tend back towards initial pressure. Only the injection volume

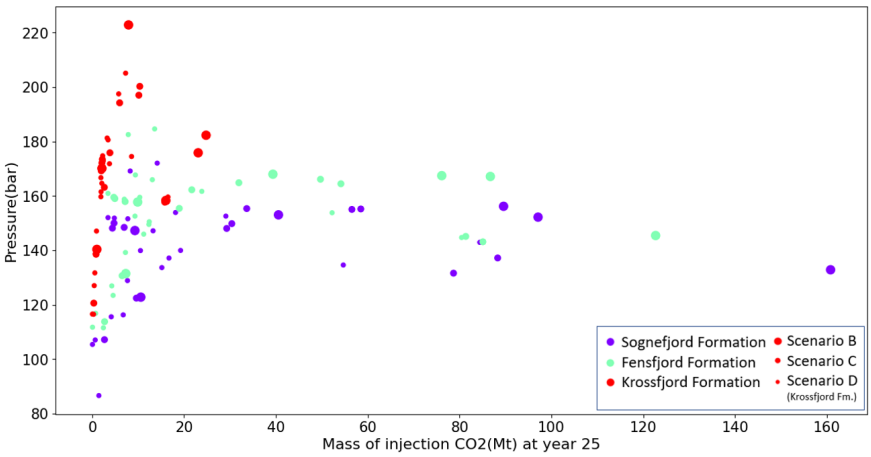

Figure 4.25: Mass of injection CO_2 in year 25 versus pressure

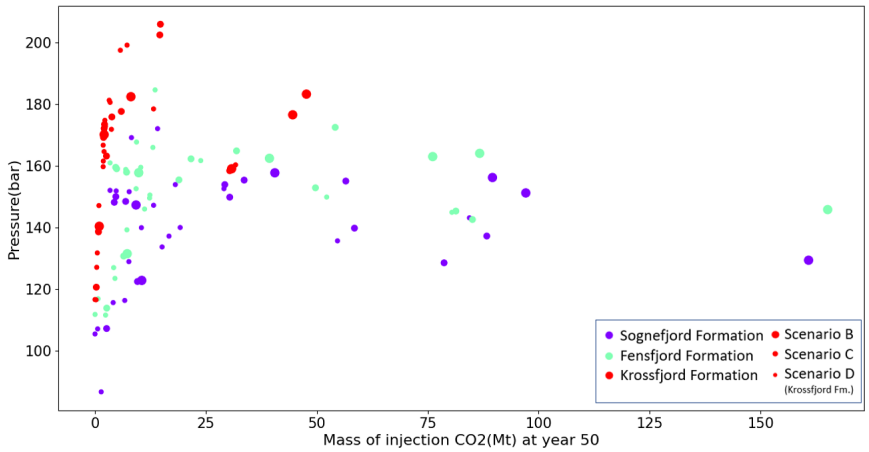

Figure 4.26: Mass of injection CO_2 in year 50 versus pressure

of the largest compartment of scenario B increases and offers the biggest possible mass of injection over 170 Mt among all these compartments.

The Sognefjord Formation compartments have the lowest pressure change interval, in most cases, there are no differences between two plots, which means that the injected volume already reaches the maximum injection volume before the year 25 and pressure in these compartments has already decayed back to the initial pressure in year 25. Only the largest compartment in scenario B can continue injection in this period and get the maximum mass of injection CO_2 around 160 Mt.

In summary, most of the injection into the compartments in Sognefjord and Fensfjord Formations ceased before year 25, with only pressure decay occuting in some compartments between year 25 and 50. Injection mass range from a few

tonnes to about 160 Mt in compartments in Sognefjord Formation, and from a few tonnes to around 170 Mt in Fensfjord Formation. Injection in some large compartments in Krossfjord Formation does not stop at year 25, and increases between year 25 and 50, with pressure decay in some C scenario compartments. The total injected mass of CO_2 ranges from a few tonnes to 50 Mt.

4.7 Numerical analysis result

Principal Component Analysis(PCA) approach is applied as the final step in this study to figure out the principal elements of multivariate datasets and understand the distribution of the output so as to have a further clustering analysis based on it. The main purpose is to replace a large number of relevant variables with a smaller set of uncorrelated variables, while retaining as much information as possible. As Fig 4.27 shown, the principal components are extracted from all variables. In general, the components with eigenvalues greater than 1 are defined as principal components, the analysis is then based on these components.

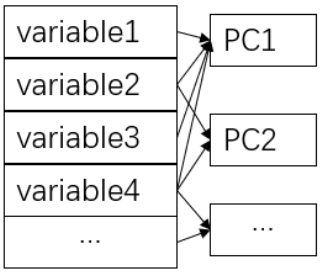

Figure 4.27: Schematic diagram of PCA

Several attempts to figure out the potential correlation of different inputs have tried, the results are divided into nine classes based on three scenarios in three formations. The first assumption is setting the dataset containing 126 datapoints, 4 variables which including the total pore volume, initial pressure, maximum pressure limit and total injected volume. The covariance matrix result shows:

$$\begin{bmatrix} 1.008 & 0.01314 & -0.0037 & 0.9032 \\ 0.01314 & 1.008 & 0.9786 & -0.061 \\ -0.0037 & 0.9786 & 1.008 & -0.1044 \\ 0.9032 & -0.061 & -0.1044 & 1.008 \end{bmatrix}$$

Then the Eigenvectors are calculated as :

$$\begin{bmatrix} 0.6207 & -0.3428 & 0.696 & -0.1132 \\ 0.3794 & 0.59612 & -0.1569 & -0.6899 \\ 0.3599 & 0.6076 & 0.0925 & 0.7019 \\ 0.5841 & -0.3973 & -0.6946 & 0.1359 \end{bmatrix}$$

The eigenvalues are calculated as: $\begin{bmatrix} 1.849 & 2.022 & 0.102 & 0.026 \end{bmatrix}$, the first two largest value are 2.022 and 1.849, which correspond to the first two principal components. The analysis graphs are showed as Fig 4.28.

The variance plot shows the main component accounts for about 50% can be interpreted by the first principal component alone, the second principal component still contains a main information accounts for about 45% while the third and

fourth principal components can safely be dropped without losing informative data. Together, the first two principal components cover about 95% of the total information. The scatter plot shows that all data points spread out in both direction, the points of scenario D gather, while scenario B and C scattered distribution, some points are located near the edges.

To have a more weak-correlation input, the second attempt includes four variables, containing the injected volume, pressure change(difference between initial pressure and maximum pressure), scaling parameter A and average depth. The covariance matrix is showed as :

$$\begin{bmatrix} 1.008 & -0.1433 & -0.8135 & -0.0610 \\ -0.1433 & 1.008 & -0.0159 & 0.8869 \\ -0.8135 & -0.0159 & 1.008 & -0.0570 \\ -0.0610 & 0.8869 & -0.0570 & 1.008 \end{bmatrix}$$

The result has some similar elements to the initial test covariance matrix result. Then the eigenvectors are computed as:

$$\begin{bmatrix} 0.3910 & -0.5890 & 0.6708 & -0.2240 \\ -0.6290 & -0.3184 & -0.1448 & -0.6943 \\ -0.2929 & 0.6478 & 0.6815 & -0.1738 \\ -0.6047 & -0.3634 & 0.2543 & 0.6615 \end{bmatrix}$$

And the eigenvalues are $\begin{bmatrix} 1.9269 & 1.7734 & 0.1878 & 0.1119 \end{bmatrix}$, the largest two values are 1.9269 and 1.7734, larger than 1, correspond to the first two principal components. The variance plot and the scatter plot are showed as Fig 4.29. The variance plot shows the first principal component takes possession of about 49% and the second principal component takes about 45%, these two covers about 94% information, others take small parts and can be safely ignored further. Compared to the initial result, the distribution of the scenario B and C are different in the middle, while the trends of the two tests are similar, so the potential factors have similarity.

To explore more potential factors for the injection, in addition to the scale parameter and the depth, the new test of different variables includes the volume ratio, pressure change, total pore volume and injectivity to have a view from a different perspective . The covariance matrix is showed as :

$$\begin{bmatrix} 1.008 & -0.3634 & 0.0563 & -0.0368 \\ -0.3634 & 1.008 & -0.0210 & 0.0294 \\ 0.0563 & -0.0210 & 1.008 & 0.5050 \\ -0.0368 & 0.0294 & 0.5050 & 1.008 \end{bmatrix}$$

Then the eigenvectors are computed as:

$$\begin{bmatrix} 1.008 & -0.1433 & -0.8135 & -0.0610 \\ -0.1433 & 1.008 & -0.0159 & 0.8869 \\ -0.8135 & -0.0159 & 1.008 & -0.0570 \\ -0.0610 & 0.8869 & -0.0570 & 1.008 \end{bmatrix}$$

Eigenvalues are $\begin{bmatrix} 0.6422 & 0.4902 & 1.3662 & 1.5014 \end{bmatrix}$. The values contain 1.5014 and 1.3662 which are larger than 1, but the differences between each value are smaller than other tests. The variance plot(Fig 4.30a) shows a relatively un-ideally result, the first principal component takes proportion about 38%, the second principal component takes about 35%, while the third and fourth principal components take around 15% and 12% respectively. The scatter plot(Fig4.30b) shows the compartments of scenario D distribute along the y-axis. The points can be grouped by different formations and distribute along the second principal component. Different scenarios in same formation distribute along the first principal component. Some points of scenario located at the edge.

Principal component 1 and 2 are very evident in the first test when the input variables include V_b, pressures and injected volume. When dP, scaling parameter A and depth are used instead of pressures and V_b, the result is similar to the first test. When I_c is used instead of A and volume ratio is used instead of volumes, the result is very different from the other two and the principal components are not obvious. This provide a foundation for the further work on PCA, a more flexible range of I_c can be included to analyse the affect of injectivity and explore more potential factors which may have influence on injection result.

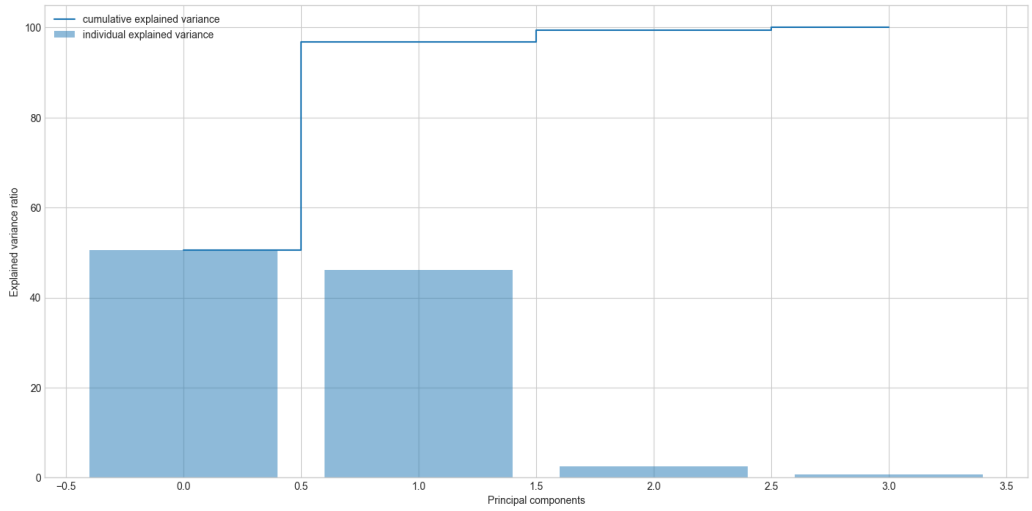

(a) Variance graph for initial test

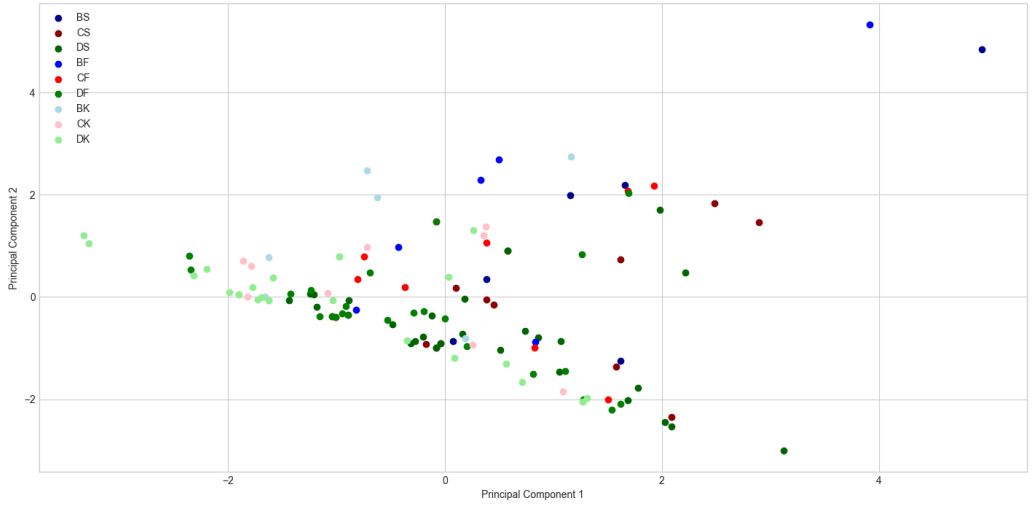

(b) PCA graph of initial test

Figure 4.28: PCA analysis result of the first test

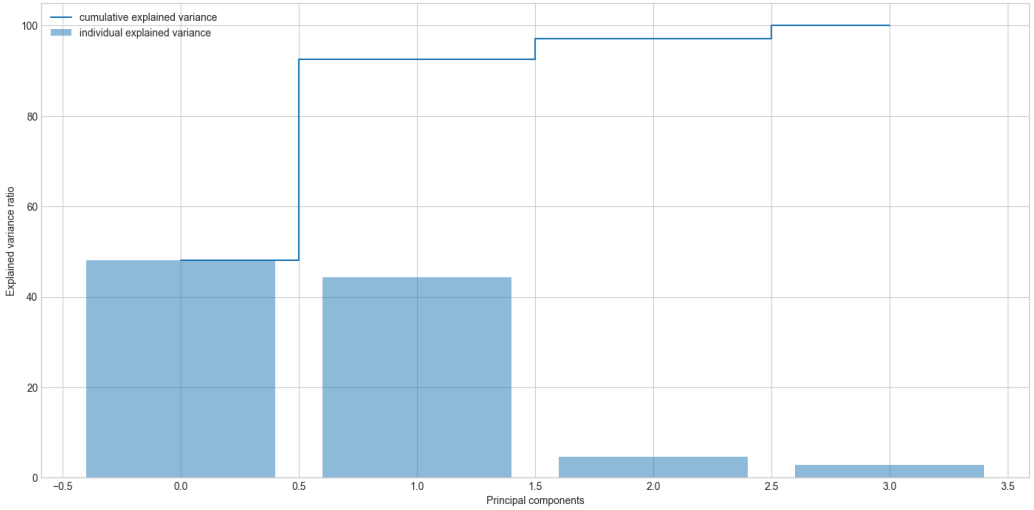

(a) Variance graph of new test

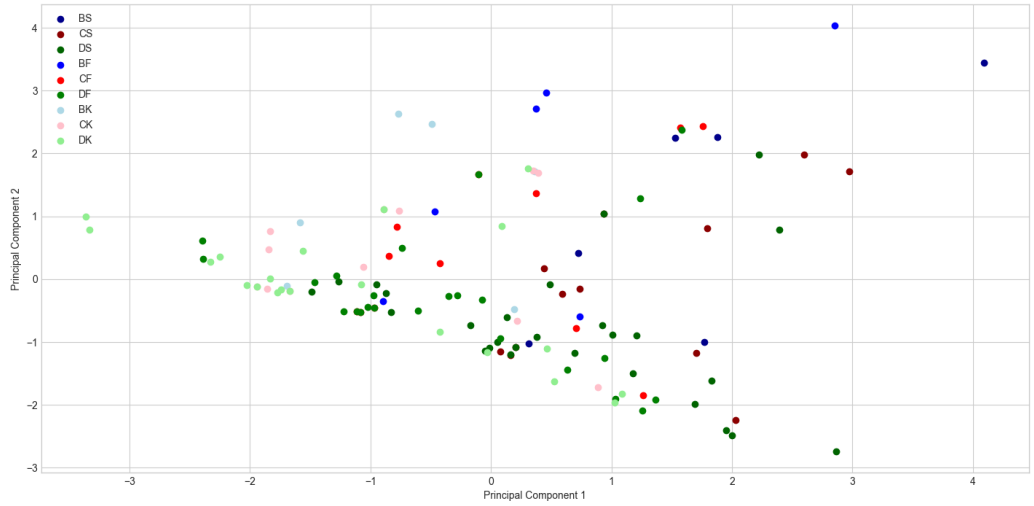

(b) PCA graph of new test

Figure 4.29: PCA analysis result of the second test

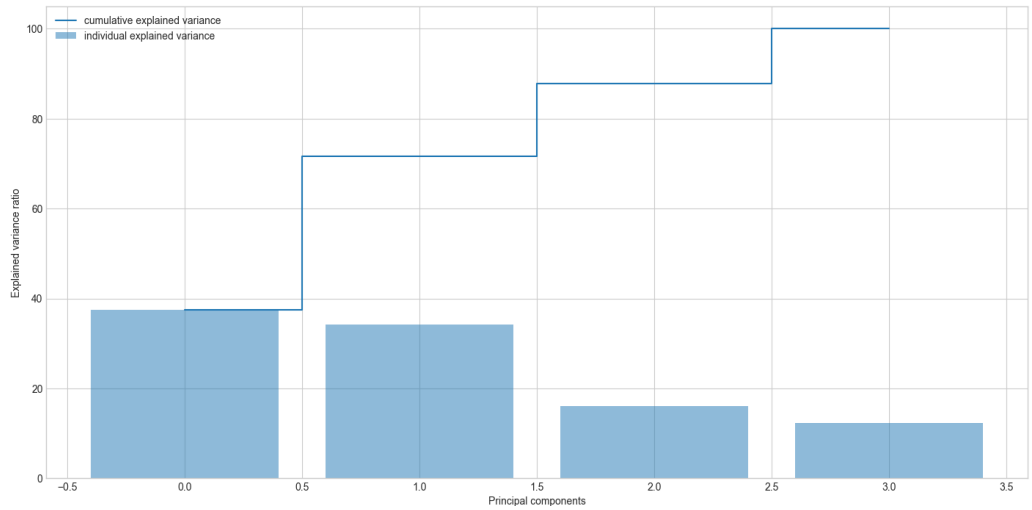

(a) Variance graph for different variables

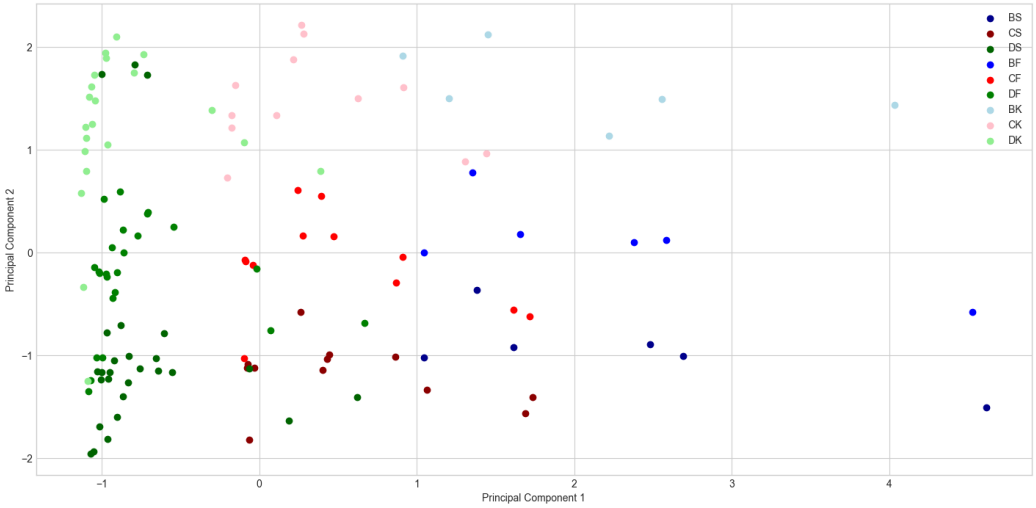

(b) PCA graph of different variables

Figure 4.30: PCA analysis result of different variables test

Chapter 5

Discussion and Conclusion

The aim of this study is to explore the deterministic parameters that control the injection process, to find the best compartment scenario that provides the maximum storage capacity, to analyse the pressure variation in all compartments and to optimize the injection by coding up simplified analytical functions in Python. Then to lay the foundation for further application of machine learning approach.

5.1 Effect of compressibility

From the Eq 3.1 and the plots in Chapter 4.1, the change of compressibility can vary the A value in the same compartment. When compressibility increases, scaling parameter A decreases, which controls the rate of pressure change. While on the other hand, it can also change the injection results by changing the maximum storage capacity, such as from the tornado plot results (Fig 4.18,4.19), the compressibility has an important effect on the variation in B3 compartment in the Sognefjord Formation and the Fensfjord Formation, due to the injected volume reaches the capacity limits.

5.2 Effect of injectivity

Compared to the results of different injectivity, the total mass of injected CO_2 has a big difference when injectivity changes in a big range. While as the Fig 4.20 shows, when injectivity is extremely high, the injectivity may not dominate the injection since the volume limits can easily be reached right after the injection, when injectivity rate is low, the change of injectivity affects the injection result.

5.3 Injection results of different scenarios

As the results shown in Fig 4.12,4.13 and 4.14, the maximum injection volume of different scenarios is uncertain. For instance, the scenario B has the biggest capacity for three formations in the area of B2, the possible reason may be the

connective compartments inside, while in the B1 area, both in Sognefjord Formation and in Krossfjord Formation, the compartments from scenario D have the largest injection volume and compartments from scenario B have the smallest injection volume, this is the exact opposite to the B2 cases. For the same scenario in three different formations, the Sognefjord Formation has the biggest injection volume in areas B1 and B5, the smallest volume is offered in the Krossfjord Formation, which may cause by the different geological settings such as porosity and permeability, then it can be simply summarized as affected by formation depth in further. So which scenario offers the optimised injection volume is depended on different formation properties and depth.

5.4 Tornado plot

From the tornado plots in different compartments, it is clear that the effective factors can be divided into two groups, pressure function and compressibility function. When injectivity is set as a high value, the compressibility , delta pressure and porosity have big effect on the result, since these factors control the volume limit regarding the compressibility function. Compare to the compartments in the Krossfjord Formation, which are assumed to have a low injectivity value, the important factors include the maximum pressure, initial pressure, injectivity as well as compressibility. Among them, maximum pressure and initial pressure control the bounds of pressure, injectivity controls the speed of injection, compressibility controls the value of scaling parameter A which is also involved in the pressure function and controls the pressure variation with time.

When compare the compartments in same formation with same parameters and relatively low injectivity, the results indicate the compartment size acts as key factor, in big compartments, the pressure limits are much easier than compressibility limits to be reached, so the parameters from the compressibility functions only have influence on injection in small compartments, for most of the cases, the factors control the pressure function (initial pressure, maximum pressure, injectivity and compressibility) are considered to be more important than others.

5.5 PCA

The final work of this study applies PCA approach to the result, aim to figure out the critical factors for injection process. When examine different parameters as input variables and total injected volume as output, the parameters directly from the pressure and compressibility function are firstly considered, and the variables without fixed values are preferred to selected for the tests. Thus the first test includes volume and pressure as input, while these are all related to the depth and size to some extent, so the second test converts the pressure to pressure change, and includes the scaling parameter and average depth instead of the initial pressure/maximum pressure. The differences between results for two tests are small

and mainly generates in the third/fourth principal component, which confirmed the hypothesis on depth and size.

To explore more potential factors, in the third test, the volume is converted to volume ratio of injected and total pore volume, instead of the scaling parameter, the injectivity (three different setpoints for three formations)is included. The result shows a big difference from the results of first two tests, the significance of both the first and second principal components decreases, the scatter plot shows the points can be grouped by different formations since the distribution is in upper, middle and lower place respectively, which may correspond to different injectivity values in three formations. Thus, the further work may include more random sampling points for injectivity in all compartments and compare the result to this initial evaluation result. .

5.6 Uncertainty Analysis

5.6.1 Parameter

The most difficult part of this project is deciding how to select the range of the numerous parameters, and our research is always based on a number of assumptions, such as constant injectivity during the injection period. The physical properties of the reservoir are always assumed to be the same and constant at different locations in the same compartment, i.e. that the subsurface medium is homogeneous. The CO_2 injection volume equation assumes that the flow rate is within a reasonable range and ignores skinning effects during injection in the well. The subsequent separation of the parameters in the computation of A also disregards the connection of the box models, presuming that the compartments are not connected to others, resulting in a value of 0 for F_b. Moreover, the pressures attend in the calculation are all from the theoretical model, the initial pressure of the injection is assumed to equal to the hydrostatic pressure of the interests depth, and the maximum pressure limit is also estimated by the fracture pressure, a more accurate method to calculate the pressure is required in the further study.

5.6.2 Data

Up to now, the major portion of the data used in box model build-up is derived from various models to estimate the parameters range, lots of parameters and potential factors are involved in the calculation, the results are highly dependent on the parameters set. In addition, the data used in the geological compartment is the real data from the Petrel project, the depth and the thickness we used in each compartment is estimated by the mean depth, which is related to the compartment area size and thickness, so it may generate errors when calculate the pressures, bulk volume and other parameters.

5.7 Scope of the work

In this study, the main findings are about the injection limits, the compressibility limits are reached in some very small compartments, the pressure limits may dominate in most of the cases. The ongoing study will be about compartment condition, such as the effect of communication between the near compartments. In addition, the compressibility effect is required to study for much more accurate geomechanical limits in different formations. The uncertainty of parameters will be the focus of the future study as well, more numerical analysis approaches are going to apply to this topic, more data points will be obtained to explore which parameter plays the most essential role in this project, then figure out an optimized solution of the injection and storage in further.

5.8 Conclusion

This project involves the study of a novel analytical approach to understanding long-term pressure in the Smeaheia area. The general direction of this work is to develop a basis for machine learning approach to study this complex process. According to the prior studies about this area, the target formations have been set in the Sognefjord Formation, Fensfjord Formation and Krossfjord Formation of the Viking Group. At this stage, some numerical solutions of the pressure analysis have been obtained, the results of the parameters setting combined with the real cases have been calculated and the variation of pressure has been estimated as well. The main objective of the work aim to understand parameter sensitivity. In summary, the study lays a foundation of further Machine learning approach application on the parameter problem and shows that multiple storage sites in the Smeaheia study region are possible of the $5 \sim 100$ Mt scale injection.

Focusing on the pressure variations, this study has analyzed the basin fluid delta pressure approach, and drawn the box method into this project which is based on the rock geomechanism. The parameter setting is critical in this process, the scaling parameter A varies with geometry and the compressibility of each compartment was studied as the first step. The result shows that the scaling parameter A decreases as the area increases, and it decreases as the pore volume increases as well; the compressibility value controls and limits the variation of A with the area and pore volume, consequently the value range of compressibility and how it affects the result have been examined. The porosity and the CO_2 density are also estimated based on different formation conditions, so as to have a specific study on compartments, which have been divided on basis of the faults systems in the Smeaheia area in order to apply the box method. Four scenarios have been created to compare the effect of different parameters and geological conditions, and then attempt to figure out a better scenario which offers the optimised injection result.

Two major constraints of injection are figured out, the pressure limit and the compressibility limit are focused on in this study. The pressure varies with time in each compartment shows that in small and middle-size compartments, the injection stops in a short time period because the pressure limits are reached in these cases. After obtaining the scientific and detailed range for different parameters, the sensitivity analysis was introduced into this study, the tornado plots indicate that the effect of parameters can be divided by pressure and the volume constraints, and the results of the same compartment in different formations may also be different due to different conditions. Finally, the results of injected mass of CO_2 as well as the pressure in different years are figured out, which indicates that the injectivity can control the final injection results as well, especially in some middle to large size compartments. Then the result plots are used to operate some numerical analysis, aim to figure out the key parameters and optimize the injection project. The PCA results show that the size and depth of the compartment can be considered as the main factors domain the injection process, in addition,

although injectivity is set as a fixed value, the result indicates the significance of injectivity as well.

In summary, the main findings of this project are given by parameter tests, in extremely large compartments, scaling parameter A tends to have a low value, leads to the pressure changes with time slowly and the pressure limit cannot be reached during the assuming injection project period, thus when injectivity is extremely high, the injected CO_2 volume increases quite quickly and reaches the volume limits, the compressibility limits can be reached only when injecting into some extremely small compartments. In generally when injectivity is fixed and relatively low, the pressure limits are reached before the compressibility limits, so injection stops and the pressure begins to decrease until down to the initial pressure. This process is dominated by injectivity as well, so the storage capacity is dependent on injectivity. The PCA results indicate the significance of geometric factors and injectivity, the further work may include the random samples of variables instead of fixed values to explore and have a better understanding. More research on parameters uncertainty analysis and numerical analysis approach are required to apply in the future work, aim to explore the key parameters that control the project and then figure out the optimization solution further.

Bibliography

IPCC. (2021). *Climate change widespread, rapid, and intensifying*. Retrieved October 30, 2021, from https://www.ipcc.ch/2021/08/09/ar6-wg1-20210809-pr/

IEA. (n.d.). *Global energy review 2021*. https://www.iea.org/reports/global-energy-review-2021

Metz, B., Davidson, O., de Coninck, H., Loos, M. & Meyer, L. (2005). Ipcc special report on carbon dioxide capture and storage. *Policy Stud.*

LPDD. (2022). *Global ccs institute reports and database*. Retrieved November 6, 2021, from https://lpdd.org/resources/global-ccs-institute-reports-and-database/

Mulrooney, M. (2021). *Derisking the smeaheia fault block: Geological controls on co2 containment*. Retrieved November 15, 2021, from https://blog.sintef.com/sintefenergy/ccs/derisking-the-smeaheia-fault-block-geological-controls-on-co2-containment/

Fawad, M., Rahman, M. J. & Mondol, N. H. (2021). Seismic reservoir characterization of potential co2 storage reservoir sandstones in smeaheia area, northern north sea. *Journal of Petroleum Science and Engineering*, *205*, 108812. https://doi.org/https://doi.org/10.1016/j.petrol.2021.108812

Ringrose, P. & Meckel, T. (2019). Maturing global co2 storage resources on offshore continental margins to achieve 2ds emissions reductions. *Scientific Reports*, *9*. https://doi.org/10.1038/s41598-019-54363-z

Rebecca Lindsey, L. D. (2021). *Climate change: Global temperature*. https://www.climate.gov/news-features/understanding-climate/climate-change-global-temperature

NASA-climate. (n.d.). *Climate change: How do we know?* https://climate.nasa.gov/evidence/

Buis, A. (2020). *Milankovitch (orbital) cycles and their role in earth's climate*. https://climate.nasa.gov/news/2948/milankovitch-orbital-cycles-and-their-role-in-earths-climate/

Ringrose, P. (2021). Co2 storage: Operation and integrity of engineered co2 storage - 1. greenhouse gases and co2 mass balance. *NTNU/Equinor*.

Ringrose, P. (2017). Principles of sustainability and physics as a basis for the low-carbon energy transition. *Petroleum Geoscience*, *23*, petgeo2016–060. https://doi.org/10.1144/petgeo2016-060

IPCC. (2016). *Radiative forcing estimates in 2011 relative to 1750 and aggregated uncertainties for the main drivers of climate change*. https://www.eea.europa.eu/data-and-maps/figures/radiative-forcing-estimates-in-2011

Philip Ringrose, M. D., Gelein de Koeijer. (2021). Co2 storage: Operation and integrity of engineered co2 storage - 4.thermodynamics and transport. *NTNU/Equinor*.

Whitson, C. & Brulé, M. (2000). *Phase behavior*. Henry L. Doherty Memorial Fund of AIME, Society of Petroleum Engineers. https://books.google.no/books?id=Z4cQAQAAMAAJ

Ringrose, P. (2020). *How to store co2 underground: Insights from early-mover ccs projects*. https://doi.org/10.1007/978-3-030-33113-9

Ringrose, P., Greenberg, S., Whittakerc, S., Nazarian, B. & Oye, V. (2017). Building confidence in co2 storage using reference datasets from demonstration projects. *Energy Procedia*, *114*, 3547–3557. https://doi.org/10.1016/j.egypro.2017.03.1484

Stephenson, M. H., Ringrose, P., Geiger, S., Bridden, M. & Schofield, D. (2019). Geoscience and decarbonization: current status and future directions. *Petroleum Geoscience*, *25*(4), 501–508. https://doi.org/10.1144/petgeo2019-084

IEA. (2021a). *Net zero by 2050*. Retrieved January 2022, from https://www.iea.org/reports/net-zero-by-2050

IEA. (2021b). *Global energy review 2021*. Retrieved October 30, 2021, from https://www.iea.org/reports/world-energy-outlook-2015

Gibbins, J. & Chalmers, H. (2008). Carbon capture and storage [Foresight Sustainable Energy Management and the Built Environment Project]. *Energy Policy*, *36*(12), 4317–4322. https://doi.org/https://doi.org/10.1016/j.enpol.2008.09.058

Bachu, S. (2015). Review of co2 storage efficiency in deep saline aquifers [Special Issue commemorating the 10th year anniversary of the publication of the Intergovernmental Panel on Climate Change Special Report on CO2 Capture and Storage]. *International Journal of Greenhouse Gas Control*, *40*, 188–202. https://doi.org/https://doi.org/10.1016/j.ijggc.2015.01.007

Zhou, Q., Birkholzer, J. T., Tsang, C.-F. & Rutqvist, J. (2008). A method for quick assessment of co2 storage capacity in closed and semi-closed saline formations [TCCS-4: The 4th Trondheim Conference on CO2 Capture, Transport and Storage]. *International Journal of Greenhouse Gas Control*, *2*(4), 626–639. https://doi.org/https://doi.org/10.1016/j.ijggc.2008.02.004

Cooper, C. D. (2009). A technical basis for carbon dioxide storage. *Energy Procedia*, *1*, 1727–1733.

Loizzo, M., Lecampion, B., Bérard, T., Harichandran, A. & Jammes, L. (2010). Reusing O&G-Depleted Reservoirs for CO2 Storage: Pros and Cons. *SPE Projects, Facilities Construction*, *5*(03), 166–172. https://doi.org/10.2118/124317-PA

Bachu, S., Bonijoly, D., Bradshaw, J., Burruss, R., Holloway, S., Christensen, N. P. & Mathiassen, O. M. (2007). Co2 storage capacity estimation: Methodology and gaps. *International Journal of Greenhouse Gas Control*, *1*(4), 430–443. https://doi.org/https://doi.org/10.1016/S1750-5836(07)00086-2

van der Meer, L. (1995). The co2 storage efficiency of aquifers [Proceedings of the Second International Conference on Carbon Dioxide Removal]. *Energy Conversion and Management*, *36*(6), 513–518. https://doi.org/https://doi.org/10.1016/0196-8904(95)00056-J

Pau, G. S., Bell, J. B., Pruess, K., Almgren, A. S., Lijewski, M. J. & Zhang, K. (2010). High-resolution simulation and characterization of density-driven flow in co2 storage in saline aquifers. *Advances in Water Resources*, *33*(4), 443–455. https://doi.org/https://doi.org/10.1016/j.advwatres.2010.01.009

Guo, T. (2021). Large-scale co2 injection: Pressure decay in multiple compartments and optimization of long-term basin pressure.

Mulrooney, M. J., Osmond, J. L., Skurtveit, E., Faleide, J. I. & Braathen, A. (2020). Structural analysis of the smeaheia fault block, a potential co2 storage site, northern horda platform, north sea. *Marine and Petroleum Geology*, *121*, 104598. https://doi.org/https://doi.org/10.1016/j.marpetgeo.2020.104598

Wu, L., Thorsen, R., Ottesen, S., Meneguolo, R., Hartvedt, K., Ringrose, P. & Nazarian, B. (2021). Significance of fault seal in assessing co 2 storage capacity and containment risks—an example from the horda platform, northern north sea. *Petroleum Geoscience*, *27*, petgeo2020–102. https://doi.org/10.1144/petgeo2020-102

Rahman, M. J., Choi, J. C., Fawad, M. & Mondol, N. H. (2021). Probabilistic analysis of vette fault stability in potential co2 storage site smeaheia, offshore norway. *International Journal of Greenhouse Gas Control*, *108*, 103315. https://doi.org/https://doi.org/10.1016/j.ijggc.2021.103315

NPD. (n.d.). Retrieved November 6, 2021, from https://www.npd.no/en/facts/publications/co2-atlases/co2-atlas-for-the-norwegian-continental-shelf/4-the-norwegian-north-sea/

Skurtveit, E., Aker, E., Soldal, M., Angeli, M. & Wang, Z. (2012). Experimental investigation of CO2 breakthrough and flow mechanisms in shale. *Petroleum Geoscience*, *18*(1), 3–15. https://doi.org/10.1144/1354-079311-016

Holgate, N., Jackson, C., Hampson, G. & Dreyer, T. (2013). Sedimentology and sequence stratigraphy of the middle-upper jurassic krossfjord and fensfjord formations, troll field, northern north sea. *Petroleum Geoscience*, *19*, 237–258. https://doi.org/10.1144/petgeo2012-039

NPD. (1985). Retrieved November 6, 2021, from https://factpages.npd.no/pbl/wellbore_documents/447_01_31_3_3_Completion_Report_and_Completion_log.pdf

GASSNOVA. (2016). *Feasibility study for full-scale ccs in norway*. https://ccsnorway.com/app/uploads/sites/6/2019/09/feasibilitystudy_fullscale_ccs_norway_2016.pdf

Hansen, O., Gilding, D., Nazarian, B., Osdal, B., Ringrose, P., Kristoffersen, J.-B., Eiken, O. & Hansen, H. (2013). Snøhvit: The history of injecting and storing 1 mt co2 in the fluvial tubåen fm [GHGT-11 Proceedings of the 11th International Conference on Greenhouse Gas Control Technologies, 18-22 November 2012, Kyoto, Japan]. *Energy Procedia*, *37*, 3565–3573. https://doi.org/https://doi.org/10.1016/j.egypro.2013.06.249

Zhang, J. J. (2019). Chapter 7 - abnormal pore pressure mechanisms. In J. J. Zhang (Ed.), *Applied petroleum geomechanics* (pp. 233–280). Gulf Professional Publishing. https://doi.org/https://doi.org/10.1016/B978-0-12-814814-3.00007-1

Bohloli, B., Ringrose, P., Grande, L. & Nazarian, B. (2017). Determination of the fracture pressure from co2 injection time-series datasets. *International Journal of Greenhouse Gas Control*, *61*, 85–93. https://doi.org/https://doi.org/10.1016/j.ijggc.2017.03.025

Weisstein, E. W. (2022). *Normal distribution*. Retrieved June 2, 2022, from https://mathworld.wolfram.com/NormalDistribution.html

Normal distribution pdf. (2022). Retrieved June 2, 2022, from https://commons.wikimedia.org/wiki/File:Normal_Distribution_PDF.svg

Iooss, B. & Lemaître, P. (2015). A review on global sensitivity analysis methods. In G. Dellino & C. Meloni (Eds.), *Uncertainty management in simulation-optimization of complex systems: Algorithms and applications* (pp. 101–122). Springer US. https://doi.org/10.1007/978-1-4899-7547-8_5

Lewis-Beck, M., Bryman, E., Bryman, A., Liao, T., Liao, T. & Sage Publications, i. (2004). *The sage encyclopedia of social science research methods*. SAGE Publications. https://books.google.no/books?id=xUy-NNnSQIIC

Abdi, H. & Williams, L. J. (2010). Principal component analysis. *WIREs Computational Statistics*, *2*(4), 433–459. https://doi.org/https://doi.org/10.1002/wics.101

Jaadi, Z. (2021). Retrieved April 1, 2021, from https://builtin.com/data-science/step-step-explanation-principal-component-analysis

NPD. (2000). Retrieved November 6, 2021, from https://factpages.npd.no/pbl/wellbore_documents/2918_32_4_1_COMPLETION_REPORT_AND_COMPLETION_LOG.pdf

Brobakken, I. I. (2018). Modeling of co2 storage in the smeaheia field, 83–84. http://hdl.handle.net/11250/2615132

Appendix A

Additional Material

A.1 Map of Smeaheia area

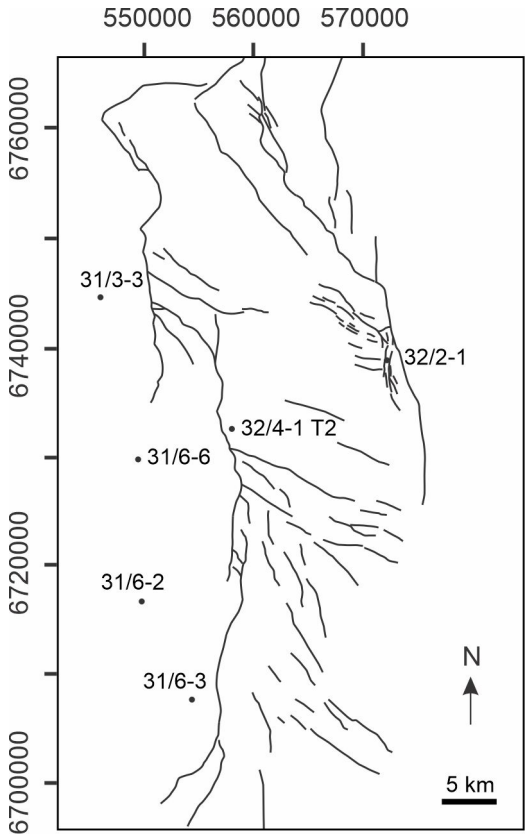

Figure A.1: Structure map of Smeaheia, modified from Wu et al., 2021

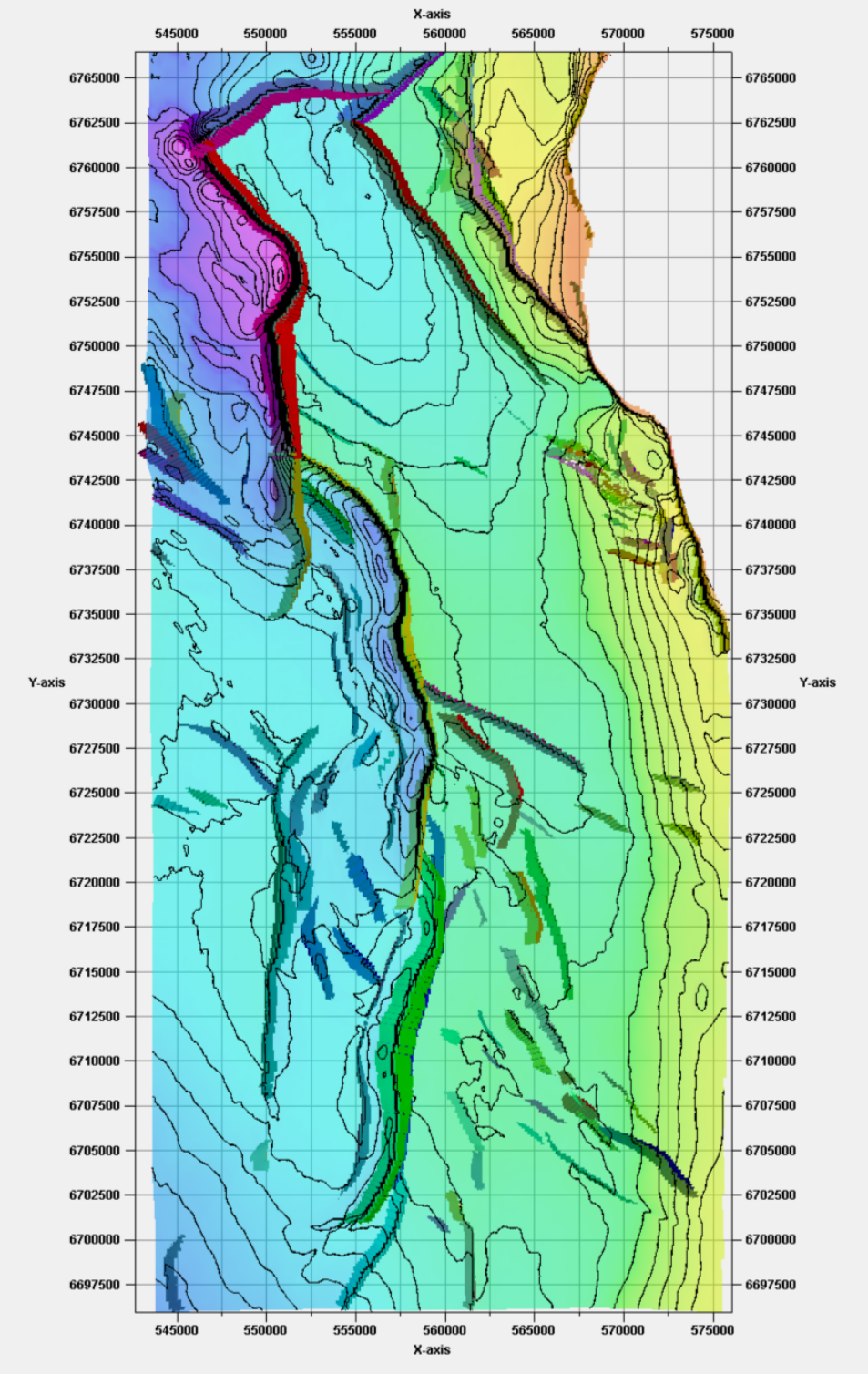

Figure A.2: Fault map of Smeaheia.

A.2 Box Division

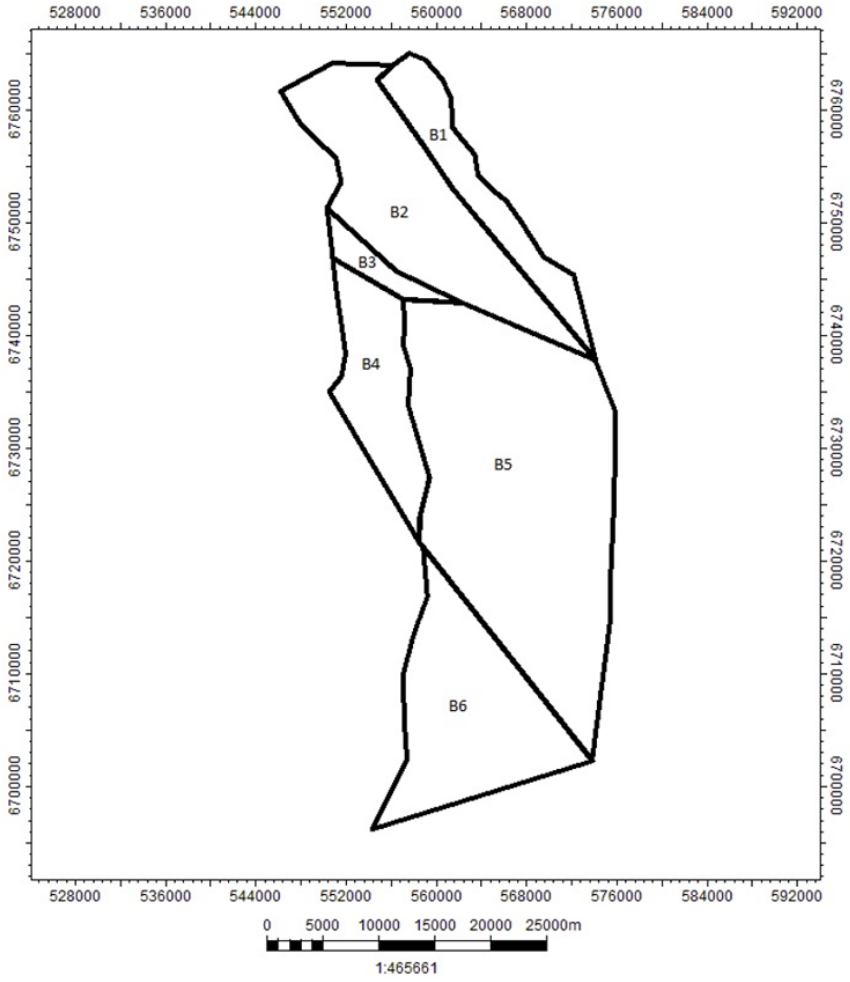

Figure A.3: Scenario B compartment map

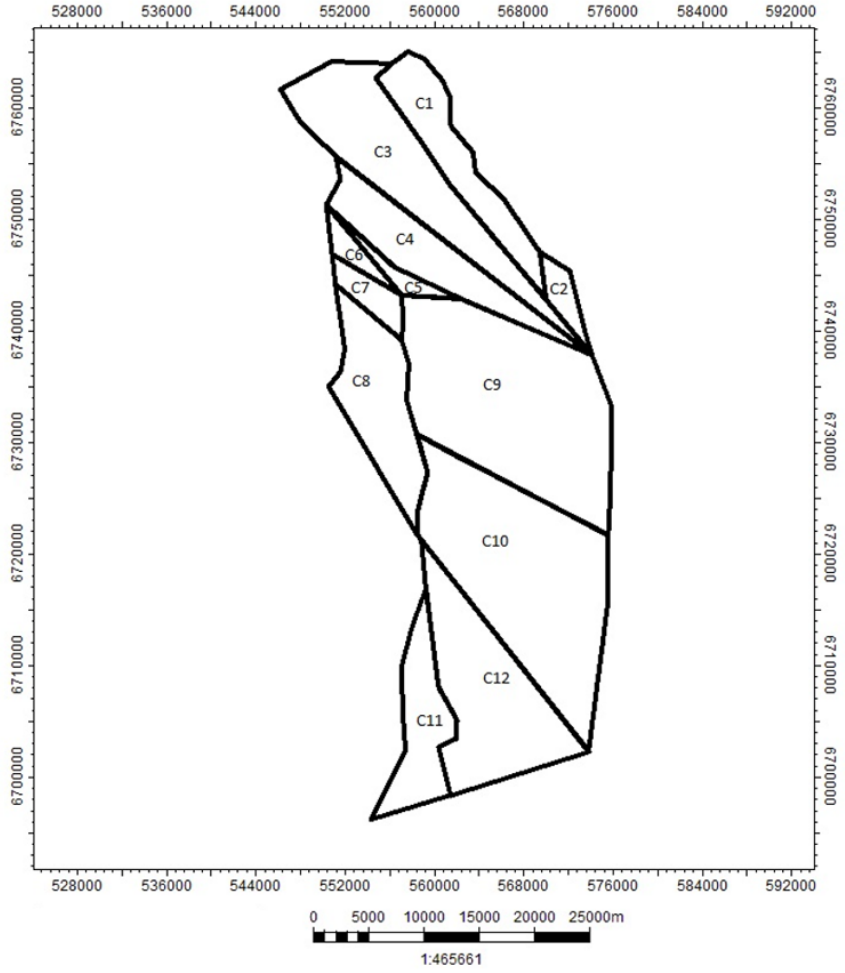

Figure A.4: Scenario C compartment map

A.3 Injection CO_2 volume estimate

Injected Volume of CO2(m3)

Sognefjord Fm.

Ic = 1000 t/d/bar

	B1				B2								B3				B4								B5								B6			
Total injected volume of scenario B(m3)	**1.82E+07**				**1.12E+08**								**1.25E+07**				**5.19E+07**								**2.58E+08**								**1.26E+08**			
	C1				C4								C5	C6			C8								C10								C12			
	1.66E+07		5.59E+06		3.91E+07								5.88E+06	6.24E+06			4.22E+07								1.30E+08								8.43E+07			
Total injected volume of scenario C(m3)	**2.22E+07**				**1.10E+08**								**1.21E+07**				**5.15E+07**								**2.57E+08**								**1.24E+08**			
	D1	D2	D3		D4	D5	D6	D7					D8	D9			D10	D11	D12	D13	D14				D15	D16	D17	D18	D19				D20	D21	D22	D23	D24
	1.23E+07	1.25E+07	5.59E+06		7.11E+07	3.74E+07	1.37E+06	1.26E+05					5.88E+06	6.24E+06			9.27E+06	4.45E+06	1.19E+07	1.56E+07	9.31E+06				1.18E+08	7.78E+06	8.74E+07	2.77E+07	1.00E+07				1.78E+07	2.31E+07	2.47E+07	2.32E+07	1.51E+07
Total injected volume of scenario D(m3)	**3.05E+07**				**1.10E+08**								**1.21E+07**				**5.06E+07**								**1.33E+08**								**1.04E+08**			

Fensfjord Fm.

Ic = 500 t/d/bar

	B1				B2								B3				B4								B5								B6			
Total injected volume of scenario B(m3)	**1.18E+07**				**1.20E+08**								**1.41E+07**				**5.50E+07**								**2.54E+08**								**1.06E+08**			
	C1		C2		C3								C5	C6			C8								C9				C10				C11			
	1.06E+07		4.80E+06		7.59E+07								6.67E+06	7.01E+06			1.02E+07								1.31E+08				1.24E+08				3.04E+07			
Total injected volume of scenario C(m3)	**1.54E+07**				**1.03E+08**								**1.37E+07**				**5.44E+07**								**2.55E+08**								**1.03E+08**			
	D1	D2	D3		D4	D5	D6	D7					D8	D9			D10	D11	D12	D13	D14				D15	D16	D17	D18	D19				D20	D21	D22	D23	D24
	1.13E+07	7.68E+06	4.80E+06		7.59E+07	3.35E+07	1.32E+06	1.27E+05					6.67E+06	7.01E+06			1.02E+07	4.85E+06	1.29E+07	1.73E+07	1.01E+07				1.22E+08	7.06E+06	8.11E+07	1.83E+07	9.94E+06				1.47E+07	1.80E+07	1.83E+07	1.69E+07	1.36E+07
Total injected volume of scenario D(m3)	**2.37E+07**				**1.11E+08**								**1.37E+07**				**5.54E+07**								**1.16E+08**								**8.16E+07**			

Krossfjord Fm.

Ic = 50 t/d/bar

	B1				B2								B3				B4								B5								B6			
Total injected volume of scenario B(m3)	**1.69E+06**				**6.27E+07**								**3.01E+06**				**1.13E+07**								**4.74E+07**								**6.55E+07**			
	C1		C2		C3								C5	C6			C7				C8				C9				C10				C11			
	1.42E+06		6.54E+05		3.01E+03								3.08E+06	2.97E+06			2.82E+06				8.19E+06				4.69E+07				4.76E+07				5.32E+06			
Total injected volume of scenario C(m3)	**2.07E+06**				**3.89E+06**								**6.05E+06**				**1.10E+07**								**9.45E+07**								**2.66E+07**			
	D1	D2	D3		D4	D5	D6	D7					D8	D9			D10	D11	D12	D13	D14				D15	D16	D17	D18	D19				D20	D21	D22	D23	D24
	1.50E+06	1.01E+06	6.54E+05		2.13E+07	5.29E+06	7.90E+05	99482.9					3.08E+06	2.97E+06			2.82E+06	3.16E+06	4.39E+06	9.03E+06	7.21E+06				4.94E+07	1.14E+06	2.07E+07	2.86E+06	2.91E+06				3.37E+06	4.67E+06	3.06E+06	2.83E+06	2.74E+06
Total injected volume of scenario D(m3)	**3.16E+06**				**2.74531336.66**								**6.05E+06**				**2.66E+07**								**7.60E+07**								**1.67E+07**			

Figure A.5: Total CO_2 injection volume in each compartment

A.4 Code

Python scripts used in the study are developed by Tian Guo, with good support from Eline Nybråten and Tobias Dyngeland.

A.4.1 Pressure Function

```
# -*- coding:utf-8 -*-
"""
Author: TianG
Date: 30.03.2022
"""
import numpy as np
import math
import matplotlib as mpl
import matplotlib.pyplot as plt
import pandas as pd
from numpy import polyfit, poly1d

# import data from spreadsheet

chart_1 = './compartments.xlsx'
df_s = pd.read_excel(chart_1, sheet_name='Sognefjord')
df_f = pd.read_excel(chart_1, sheet_name='Fensfjord')
df_k = pd.read_excel(chart_1, sheet_name='Krossfjord')
box_id_s = df_s.iloc[:, 0]
box_id_f = df_f.iloc[:, 0]
box_id_k = df_k.iloc[:, 0]
# size of area, km2
size_s = df_s.iloc[:, 1] * 1.0e-6
size_f = df_f.iloc[:, 1] * 1.0e-6
size_k = df_k.iloc[:, 1] * 1.0e-6
size_all = np.hstack([size_s,size_f,size_k])

# average thickness, m
thickness_s = df_s.iloc[:, 2]
thickness_f = df_f.iloc[:, 2]
thickness_k = df_k.iloc[:, 2]
thickness = np.hstack([thickness_s,thickness_f, thickness_k])
# average depth, m
dep_s = df_s.iloc[:, 4]
dep_f = df_f.iloc[:, 4]
dep_k = df_k.iloc[:, 4]
dep = np.hstack([dep_s,dep_f,dep_k])

# calculation fracture pressure, MPa
p_fracture_s = df_s.iloc[:, 7]
p_fracture_f = df_f.iloc[:, 7]
p_fracture_k = df_k.iloc[:, 7]
```

```
43 p_fracture = np.hstack([p_fracture_s, p_fracture_f, p_fracture_k
       ])
44 # calculation hydrostatic pressure, MPa
45 p_hydro_s = df_s.iloc[:, 8]
46 p_hydro_f = df_f.iloc[:, 8]
47 p_hydro_k = df_k.iloc[:, 8]
48 p_hydro = np.hstack([p_hydro_s, p_hydro_f, p_hydro_k])
49
50 pressures = []
51 poreVol = []
52
53 por_s = list([0.3] * len(box_id_s))
54 por_f = list([0.27] * len(box_id_f))
55 por_k = list([0.23] * len(box_id_k))
56 por = np.hstack([por_s, por_f, por_k])
57 list_V = []
58
59 # loop for different compartments
60 for comp in range(len(dep)):
61     print("box number:", comp)
62     p_i = p_hydro[comp]*10
63     p_f = p_fracture[comp] * 10  # bar
64     p_w = 0.9 * p_f
65     print("Pressure limitP_w):", p_w, "Bar")
66     # pressure decay curve
67     euler = math.exp(0.5772156649)
68     r = 0.5  # regime, for pressure function
69     years = 50
70     cb_n = 4
71     cb = 7.0e-9 - (cb_n * 1.0e-9)
72     a7 = -0.28 * size_all[comp] + 44.6
73     a3 = -0.1224 * size_all[comp] + 44.69
74     # calculate a
75     a = a7 + (a3 - a7) / 4 * cb_n
76     if a <= 2:
77         a = 2
78     print("scaling parameter:", a)
79     Ic = 40
80     dP = 3  # MPa
81     dv = np.multiply(size_all[comp], thickness[comp]) * cb * por
           [comp] * dP * 1.0e+12
82     print("volume limit:", dv)
83     lst2 = []
84     p_d = []
85     pres = []
86     rate = []
87     mass = []
88     xaxis = list(np.arange(0,years+0.5,0.5))
89     p_final = 0
90     pres_decay = []
```

```
91      arr_pres_decay = []
92      p_max = 0
93      t_max = 0
94      p_new = []
95      vol=[]
96      totalvol=[]
97      pressures=0
98  # loop in the increasing period
99      for i in range(0, len(xaxis)):
100         time = xaxis[i]
101         if i == 0:
102             time = 0.25 * euler
103         p_d.append(r * math.log(4 * time / euler))
104         # print("time pressure:", pd)
105         pres.append(p_i + a * p_d[i])
106         print("pressure:", pres[i])
107         rate.append(Ic * (p_w - pres[i]))
108         vol.append(365 * rate[i])  # m3/year
109         totalvol.append(np.sum(vol))
110
111         if totalvol[i] <= dv and pres[i] <= p_w:
112             continue
113         else:
114             if pres[i] > p_w and totalvol[i] <= dv:
115                 t_max = xaxis[i-1]
116                 p_final = pres[i - 1]  # final pressure, bar
117                 print("max injection time:", t_max, "Year\n", "
                        final pressure(bar):", p_final)
118                 lst2 = list(np.arange(t_max+0.5, years + 0.5,
                        0.5))
119                 pres.pop()  # delete last element(> p_w)
120             else:
121                 totalvol[i] = dv
122             break
123 # loop for decreasing period
124     for j in range(len(lst2)):
125         p_d.append(r * math.log(4 * time / euler))
126         pres_decay.append(p_final - a * p_d[j+1])
127         arr_pres_decay = np.array(pres_decay)  # list convert to
              array
128         arr_pres_decay[arr_pres_decay <= p_i] = p_i
129
130     p_new = np.hstack([pres, arr_pres_decay])
131     rate_new_1 = Ic * (p_w - pres)
132     rate_new_2 = np.zeros(len(pres_decay))
133     rate_new = np.hstack([rate_new_1,rate_new_2])
134     arr_rate = np.array(rate_new)
135
136 # generate plot
137     fig = plt.figure()
```

```
138     plt.plot(xaxis[0:len(p_new)], p_new)
139     labels = np.arange(0,years,1)
140     plt.xticks(labels, rotation = 'vertical')
141     plt.xlabel("Injection period(Year)")
142     plt.ylabel("Pressure(Bar)")
143     plt.show()
```

A.4.2 Random sampling A

```
# -*- coding: utf-8 -*-
"""
Author: TianG
Date: 08.03.2022
"""

import numpy as np
import matplotlib.pyplot as plt
import pandas as pd
chart_1 = './compartments.xlsx'
df_s = pd.read_excel(chart_1, sheet_name='Sognefjord')
df_f = pd.read_excel(chart_1, sheet_name='Fensfjord')
df_k = pd.read_excel(chart_1, sheet_name='Krossfjord')
box_id_s = df_s.iloc[:, 0]
box_id_f = df_f.iloc[:, 0]
box_id_k = df_k.iloc[:, 0]
# size of area, km2
size_s = df_s.iloc[:, 1] * 1.0e-6
size_f = df_f.iloc[:, 1] * 1.0e-6
size_k = df_k.iloc[:, 1] * 1.0e-6
size_all = np.hstack([size_s,size_f,size_k])
print(size_all)
# average thickness, m
thickness_s = df_s.iloc[:, 2]
thickness_f = df_f.iloc[:, 2]
thickness_k = df_k.iloc[:, 2]
thickness = np.hstack([thickness_s,thickness_f, thickness_k])
# average depth, m
dep_s = df_s.iloc[:, 4]
dep_f = df_f.iloc[:, 4]
dep_k = df_k.iloc[:, 4]
dep = np.hstack([dep_s,dep_f,dep_k])
# calculation fracture pressure, MPa
p_fracture_s = df_s.iloc[:, 7]
p_fracture_f = df_f.iloc[:, 7]
p_fracture_k = df_k.iloc[:, 7]
p_fracture = np.hstack([p_fracture_s, p_fracture_f, p_fracture_k
    ])
# calculation hydrostatic pressure, MPa
p_hydro_s = df_s.iloc[:, 8]
p_hydro_f = df_f.iloc[:, 8]
p_hydro_k = df_k.iloc[:, 8]
p_hydro = np.hstack([p_hydro_s, p_hydro_f, p_hydro_k])
por_s = np.random.uniform(low = 0.27, high = 0.34, size = len(
    box_id_s))
por_f = np.random.uniform(low = 0.26, high = 0.28, size = len(
    box_id_f))
```

```
45 por_k = np.random.uniform(low = 0.21, high = 0.25, size = len(
       box_id_k))
46 por = np.hstack([por_s, por_f, por_k])
47 print("porosity:", por)
48 vb = np.multiply(np.multiply(size_all,thickness),por)*1.0e+06  #
       m3
49
50 dp = 3 #MPa
51
52 ic = np.random.uniform(low=30, high=90, size=len(size_all))
53 print("Injectivity:", ic)
54 p_w = p_fracture * 9  # bar
55 p_i = p_hydro  * 10  # bar
56 p_f = p_fracture * 10 # bar
57
58 cb = np.random.uniform(low = 1.00e-11, high = 1.00e-9, size = 6
       )
59 print(cb)
60
61 pd = 2.014
62
63 rate_1 = cb[1] * vb * dp * 1000000 / 365/25
64 a_1 =(p_w - p_i - rate_1 / ic)/ pd
65 rate_2 = cb[2]* vb * dp * 1000000 / 365/25
66 a_2 =(p_w - p_i - rate_2 / ic)/ pd
67 rate_3 = cb[3]* vb * dp * 1000000 / 365/25
68 a_3 =( p_w - p_i - rate_3 / ic)/ pd
69 rate_4 = cb[4]* vb * dp * 1000000 / 365/25
70 a_4 =( p_w - p_i - rate_4 / ic)/ pd
71 rate_5 = cb[5] * vb * dp * 1000000 / 365/25
72 a_5 =(p_w - p_i - rate_5 / ic)/ pd
73 rate_6 = cb[0] * vb * dp * 1000000 / 365/25
74 a_6 =(p_w - p_i - rate_6 / ic)/ pd
75
76 plt.scatter(size_all,a_1,label = cb[1])
77 plt.scatter(size_all,a_2,label = cb[2])
78 plt.scatter(size_all,a_3,label = cb[3])
79 plt.scatter(size_all,a_4,label = cb[4])
80 plt.scatter(size_all,a_5,label = cb[5])
81 plt.scatter(size_all,a_6,label = cb[0])
82 plt.ylim(0,40)
83 plt.xlabel("Area Size(km2)")
84 plt.ylabel("A")
85
86 plt.legend(loc="best")
87 plt.show()
88
89 plt.scatter(vb,a_1,label = cb[1])
90 plt.scatter(vb,a_2,label = cb[2])
91 plt.scatter(vb,a_3,label = cb[3])
```

```
92  plt.scatter(vb,a_4,label = cb[4])
93  plt.scatter(vb,a_5,label = cb[5])
94  plt.scatter(vb,a_6,label = cb[0])
95  plt.ylim(0,40)
96  plt.xlabel("Pore volume(m3)")
97  plt.ylabel("A")
98
99  plt.legend(loc="best")
100 plt.show()
```

A.4.3 Injection Volume calculation

```
# -*- coding:utf-8 -*-
"""
Author: TianG
Date: 24.04.2022
"""
import numpy as np
import math
import matplotlib.pyplot as plt
import pandas as pd
import seaborn as sns


# import data from spreadsheet

chart_1 = './compartments.xlsx'
df_s = pd.read_excel(chart_1, sheet_name='Sognefjord')
df_f = pd.read_excel(chart_1, sheet_name='Fensfjord')
df_k = pd.read_excel(chart_1, sheet_name='Krossfjord')
box_id_s = df_s.iloc[:, 0]
box_id_f = df_f.iloc[:, 0]
box_id_k = df_k.iloc[:, 0]
# size of area, km2
size_s = df_s.iloc[:, 1] * 1.0e-6
size_f = df_f.iloc[:, 1] * 1.0e-6
size_k = df_k.iloc[:, 1] * 1.0e-6
size_all = np.hstack([size_s,size_f,size_k])

# average thickness, m
thickness_s = df_s.iloc[:, 2]
thickness_f = df_f.iloc[:, 2]
thickness_k = df_k.iloc[:, 2]
thickness = np.hstack([thickness_s,thickness_f, thickness_k])
# average depth, m
dep_s = df_s.iloc[:, 4]
dep_f = df_f.iloc[:, 4]
dep_k = df_k.iloc[:, 4]
dep = np.hstack([dep_s,dep_f,dep_k])

#  fracture pressure, MPa
p_fracture_s = df_s.iloc[:, 7]
p_fracture_f = df_f.iloc[:, 7]
p_fracture_k = df_k.iloc[:, 7]
p_fracture = np.hstack([p_fracture_s, p_fracture_f, p_fracture_k
    ])
#  hydrostatic pressure, MPa
p_hydro_s = df_s.iloc[:, 8]
p_hydro_f = df_f.iloc[:, 8]
p_hydro_k = df_k.iloc[:, 8]
```

```
48 p_hydro = np.hstack([p_hydro_s, p_hydro_f, p_hydro_k])
49
50 # calculation CO2 density, kg/m3
51 den_s = -0.001147182 * (dep_s ** 2) + 3.3925 * dep_s - 1793
52 den_f = -0.00041716 * (dep_f ** 2) + 1.54 * dep_f - 660.6
53 den_k = -0.00045366 * (dep_k ** 2) + 1.69421 * dep_k - 855.7
54 den = np.hstack([den_s, den_f, den_k])
55
56 # randomly set the porosity in different formations
57 #por_s = np.random.uniform(low = 0.27, high = 0.34, size = len(
       box_id_s))
58 #por_f = np.random.uniform(low = 0.26, high = 0.28, size = len(
       box_id_f))
59 #por_k = np.random.uniform(low = 0.21, high = 0.25, size = len(
       box_id_k))
60 por_s = list([0.3] * len(box_id_s))
61 por_f = list([0.27] * len(box_id_f))
62 por_k = list([0.23] * len(box_id_k))
63 por = np.hstack([por_s, por_f, por_k])
64
65 # change Ic
66 Ic_s = list([1500]*len(box_id_s))
67 Ic_f = list([725]*len(box_id_f))
68 Ic_k = list([75]*len(box_id_k))
69 Injectivity = np.hstack([Ic_s,Ic_f,Ic_k])
70
71 pressures = []
72 poreVol = []
73
74 # loop all compartments
75 for comp in range(len(size_all)):
76     density = den[comp]
77     Ic = Injectivity[comp]
78     print("box number:", comp, "density:", density)
79     p_i = p_hydro[comp]*10
80     print(" initial pressure:", p_i, 'bar')
81     p_f = p_fracture[comp] * 10  # bar
82     # calculate well pressure, bar
83     p_w = 0.9 * p_f
84     print("Pressure limitP_w):", p_w, "Bar")
85     # pressure decay curve
86     euler = math.exp(0.5772156649)
87     r = 0.5  # regime, for pressure function
88     dens = 0.79
89     visc = 0.07
90     dP = 3  # MPa
91     cb = 3.0e-09
92     a = -0.1224 * size_all[comp] + 44.69  # A function for
           compressibility: 3.0e-09"""
93     """cb_n = np.random.randint(low=0, high=6, size=1)
```

```
94      cb = 7.0e-9 - (cb_n * 1.0e-9)
95      print(cb)
96      #calculate A for different cb
97      a7 = -0.28 * size_all[comp] + 44.6
98      a3 = -0.1224 * size_all[comp] + 44.69"""
99      #a = a7 + (a3 - a7) / 4 * cb_n
100     #a[a<2]=2
101     if a < 2:
102         a = 2
103     print("scaling parameter:", a)
104     dv = np.multiply(size_all[comp], thickness[comp]) * cb * por
            [comp] * dP * 1.0e+12
105     # dv = size_all[comp] * thickness[comp] * np.multiply(cb,
            por) * 1.0e+6 * dP * 1.0e+6
106     print("volume limit:", dv)
107     years = 50
108     totalVol = 0
109     p_d = []
110     pres = []
111     min_i = 0
112     max_i = 0
113     decay = 0
114     n = 1
115     figtime = 0
116     for i in range(0,years+1):
117         time = i
118         if i == 0:
119             time = 0.25 * euler
120         p_d.append(r*math.log(4*time/euler))
121
122         # set compressibility-volume limit
123         if (totalVol > dv).any():
124             pres.append(pres[i-1])
125             totalVol = dv
126         # set pressure limit
127
128         elif ((p_i + a * p_d[i-min_i]) >= p_w).any():
129             decay = 1
130
131         if decay == 0:
132             pres.append(p_i + a * p_d[i-min_i])
133             max_i = i
134             totalVol += Ic * (p_w - pres[i]) * 365
135
136         elif decay == 1:
137             #  pressure reaches initial pressure
138             if ((p_i+a*p_d[max_i]-a*p_d[i-max_i+n-1]) <= p_i).
                    any():
139                 pres.append(p_i)
140             else:
```

```
                pres.append(p_i + p_d[max_i]-a*p_d[i-max_i+n])
                min_i = i
                totalVol += 0
        # set plot time and result
        if i == 50:
            figtime = i
            pressures.append(pres[i])
            poreVol.append(totalVol)


poreVol_x = np.array(poreVol,dtype=np.float32)

mass = poreVol_x * density * 1.0E-09  # Mt
poreVol_x = np.log(poreVol_x)
mass_x = np.log(mass)
print(mass)

# set color and size for points
size = list
    ([[80]*6+[40]*12+[20]*24+[80]*6+[40]*12+[20]*24+[80]*6+[40]*12+[20]*24])

col = list
    ([[1]*6+[1]*12+[1]*24+[2]*6+[2]*12+[2]*24+[3]*6+[3]*12+[3]*24])


plt.scatter(mass, pressures, s = size, c = col, cmap = 'rainbow'
    )

plt.xlabel('Mass of Injection CO2 (Mt),' + str(figtime) + ' Year
    ',fontsize = 16)
plt.ylabel('Pressure (bar)', fontsize = 16)

plt.tick_params(labelsize = 14)

plt.show()
```

A.4.4 PCA

```
# -*- coding:utf-8 -*-
"""
Author: TianG
Date: 23.05.2022
"""
import pandas as pd
import numpy as np
from sklearn.preprocessing import StandardScaler
import matplotlib.pyplot as plt
from sklearn.decomposition import PCA as sklearnPCA

df = pd.read_excel('./pca.xlsx', sheet_name='Sheet2')
df.columns = ['injV', 'pmax-pi','a', 'depth', 'class']
df.dropna(how="all", inplace=True)
X = df.iloc[:,0:4]
Y = df.iloc[:,4]
# covariance matrix
X_std = StandardScaler().fit_transform(X)
mean_vec = np.mean(X_std, axis = 0)
cov_mat = (X_std - mean_vec).T.dot((X_std-mean_vec))/(X_std.
    shape[0]-1)
print('covariance matrix \n%s' %cov_mat)
print('Numpy covariance matrix: \n%s' %np.cov(X_std.T))

#correlation matrix
cor_mat1 = np.corrcoef(X_std.T)

eig_vals, eig_vecs = np.linalg.eig(cor_mat1)

print("Eigenvectors \n%s" %eig_vecs)
print("\nEigenvalues \n%s" %eig_vals)

# singular value decomposition

u,s,v = np.linalg.svd(X_std.T)

# sorting eigenpairs

for ev in eig_vecs.T:
    np.testing.assert_array_almost_equal(1.0, np.linalg.norm(ev)
        )

# Make a list of (eigenvalue, eigenvector) tuples
eig_pairs = [(np.abs(eig_vals[i]), eig_vecs[:,i]) for i in range
    (len(eig_vals))]

# Sort the (eigenvalue, eigenvector) tuples from high to low
eig_pairs.sort(key=lambda x: x[0], reverse=True)
```

```
46
47 # Visually confirm that the list is correctly sorted by
       decreasing eigenvalues
48 print('Eigenvalues in descending order:')
49 for i in eig_pairs:
50     print(i[0])
51
52 # variance explained: how many princinpal components are we
       going to choose for new feature surface?
53 tot = sum(eig_vals)
54 var_exp = [(i / tot)*100 for i in sorted(eig_vals, reverse=True)
       ]
55 cum_var_exp = np.cumsum(var_exp)
56
57 # plot for variance
58 with plt.style.context('seaborn-whitegrid'):
59     plt.figure(figsize=(6, 4))
60
61     plt.bar(range(4), var_exp, alpha=0.5, align='center',
62             label='individual explained variance')
63     plt.step(range(4), cum_var_exp, where='mid',
64              label='cumulative explained variance')
65     plt.ylabel('Explained variance ratio')
66     plt.xlabel('Principal components')
67     plt.legend(loc='best')
68     plt.tight_layout()
69
70 sklearn_pca = sklearnPCA(n_components=2)
71 Y_sklearn = sklearn_pca.fit_transform(X_std)
72
73 with plt.style.context('seaborn-whitegrid'):
74     plt.figure(figsize=(6, 4))
75     for lab, col in zip(('BS', 'CS', 'DS','BF','CF','DF','BK','
           CK','DK'),
76                         ('darkblue', 'darkred', 'darkgreen','
                             blue','red','green','lightblue','
                             pink','lightgreen')):
77         plt.scatter(Y_sklearn[Y==lab, 0],
78                     Y_sklearn[Y==lab, 1],
79                     label=lab,
80                     c=col)
81     plt.xlabel('Principal Component 1')
82     plt.ylabel('Principal Component 2')
83     plt.legend(loc='best')
84     plt.tight_layout()
85     plt.show()
```

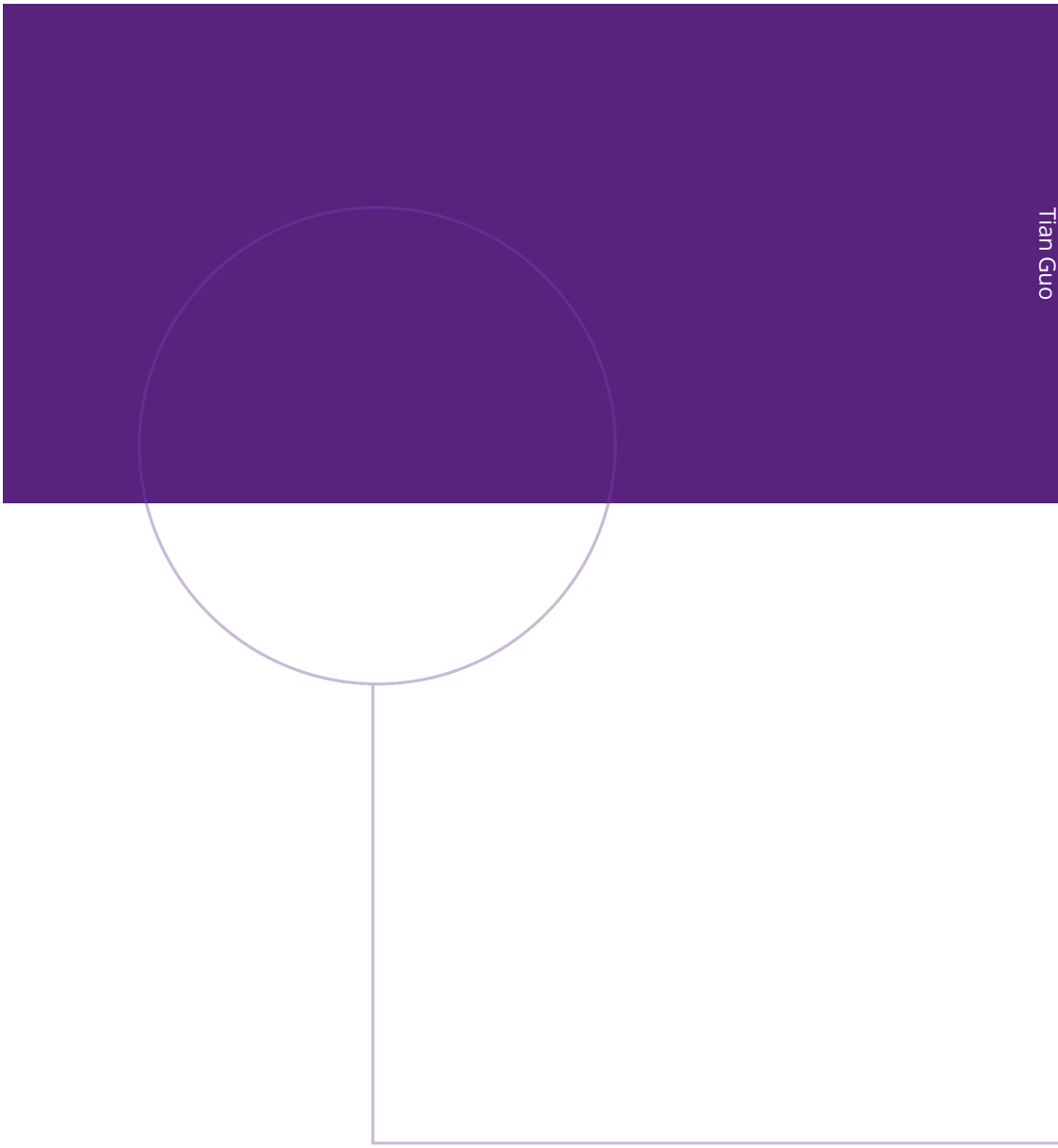

Tian Guo

NTNU

Norwegian University of
Science and Technology